

# Integration of Thermochimica into MOOSE-based Molten Salt Reactor Loop Simulations

INL/RPT-24-81124

SEPTEMBER 30, 2024

**Mauricio Tano**  
**Samuel Walker**

*Idaho National Laboratory, Thermal Hydraulics*

**Parikshit Bajpai**  
**Daniel Schwen**

*Idaho National Laboratory, Computational Mechanics and Materials*



#### DISCLAIMER

This information was prepared as an account of work sponsored by an agency of the U.S. Government. Neither the U.S. Government nor any agency thereof, nor any of their employees, makes any warranty, expressed or implied, or assumes any legal liability or responsibility for the accuracy, completeness, or usefulness, of any information, apparatus, product, or process disclosed, or represents that its use would not infringe privately owned rights. References herein to any specific commercial product, process, or service by trade name, trade mark, manufacturer, or otherwise, does not necessarily constitute or imply its endorsement, recommendation, or favoring by the U.S. Government or any agency thereof. The views and opinions of authors expressed herein do not necessarily state or reflect those of the U.S. Government or any agency thereof.

# **Integration of Thermochimica into MOOSE-based Molten Salt Reactor Loop Simulations**

**Mauricio Tano**

**Samuel Walker**

**Idaho National Laboratory, Thermal Hydraulics**

**Parikshit Bajpai**

**Daniel Schwen**

**Idaho National Laboratory, Computational Mechanics and Materials**

**September 30, 2024**

**Idaho National Laboratory**

**Idaho Falls, Idaho 83415**

**<http://www.inl.gov>**

**Prepared for the  
U.S. Department of Energy  
Office of Nuclear Energy  
Under DOE Idaho Operations Office  
Contract DE-AC07-05ID14517**

*Page intentionally left blank*

## **ABSTRACT**

Molten Salt Reactors (MSRs) offer significant advantages in terms of safety, operational efficiency, and high-temperature capabilities. A key challenge in MSR operation is the continuous tracking of species, including corrosion products and fission byproducts, and the accurate modeling of their transport and interactions within the reactor. This milestone demonstrates the integration of Pronghorn, a computational fluid dynamics (CFD) tool, with ThermoChimica, a Gibbs energy minimizer, to model chemical speciation, thermodynamic equilibrium, and corrosion processes in MSRs.

Key advancements include the development of two-phase flow models for species tracking between liquid and gas phases, the incorporation of the Poisson-Nernst-Planck (PNP) model with Butler-Volmer kinetics to simulate electrochemical corrosion and multi-region depletion models for tracking isotopic evolution. Validation against experimental data from Oak Ridge National Laboratory confirms the accuracy of the corrosion models. The resulting multiphysics framework enables high-fidelity simulations of species transport, corrosion, and depletion in MSRs, providing valuable insights for reactor design and long-term operation.

## SUMMARY

Molten Salt Reactors (MSRs) are an advanced nuclear technology offering inherent safety, high operational efficiency, and the capability to operate at high temperatures. A key aspect of MSR operation, addressed in this milestone, is the continuous tracking of species—including gas transport, plating, and leaching with structures—and the modeling of corrosion processes. Accurate modeling of these phenomena is essential to ensure reactor operability, minimize long-term material degradation, and optimize reactor efficiency.

This milestone achieved the integration of Pronghorn, NEAMS’s coarse-mesh computational fluid dynamics (CFD) tool, with Thermochimica, a Gibbs energy minimizer software that has been coupled to MOOSE. Pronghorn handles fluid flow and heat transfer simulations, while Thermochimica calculates the thermodynamic equilibrium and chemical speciation of the molten salt. This coupling provides a high-fidelity framework for tracking species and predicting corrosion product distribution, allowing for more detailed and accurate simulations of MSR behavior.

A key advancement was the inclusion of two-phase flow modeling, where gas bubbles in the molten salt significantly influence species transport. The interaction between liquid and gas phases affects corrosion rates and species accumulation, making two-phase flow modeling crucial for understanding dynamic reactor environments. The ability to track volatile species between phases supports optimizing MSR designs for enhanced safety and efficiency.

Additionally, the Poisson-Nernst-Planck (PNP) model, coupled with Butler-Volmer kinetics, was introduced into MOOSE to simulate electrochemical processes driving corrosion. These models improve predictions of species transport driven by electric currents and chemical gradients, enabling the simulation of species leaching and plating on reactor structures.

The multi-region depletion modeling developed via Griffin further enhances this framework by accounting for the evolving isotopic composition of molten salt. These depletion models predict how fuel composition changes over time, impacting species transport and reactor performance. Integrating these models enables long-term operational predictions for MSRs.

This milestone demonstrates an initial implementation of a comprehensive MOOSE-based multiphysics framework that integrates thermal-hydraulics, thermochemistry, electrochemistry, two-phase flow, and depletion modeling for accurate species tracking and corrosion prediction in MSRs. The key achievements include:

- **Coupling Thermochimica with Pronghorn:** Integrated Thermochimica with Pronghorn for chemical speciation and thermodynamic equilibrium modeling in MSRs.
- **Two-phase flow integration:** Developed two-phase flow models to track volatile species and their transport between liquid and gas phases.
- **Species transport modeling:** Enhanced tracking of corrosion and fission products using the Poisson-Nernst-Planck model and Butler-Volmer kinetics.
- **Multi-region depletion modeling:** Advanced depletion models to track isotopic evolution, coupled with speciation, and their impact on species transport and corrosion.
- **Validation of PNP model:** Validated the Poisson-Nernst-Planck model using experimental data from Oak Ridge National Laboratory’s corrosion loop.
- **3D and 2D loop simulations:** Demonstrated natural convection loop simulations, capturing species transport, corrosion, and flow behavior in realistic geometries.

- **Full MSR loop simulations:** Demonstrated species tracking and Thermochimica-driven phase equilibrium calculations in full-loop MSRs, with examples of a fluoride system and a chloride system, namely the Molten Salt Reactor Experiment and Molten Chloride Reactor Experiment, respectively.

# CONTENTS

SUMMARY	iii
1. INTRODUCTION	1
2. MOLTEN SALT THERMOCHEMISTRY CAPABILITIES IN THERMOCHIMICA AND MOOSE	4
2.1. Gibbs Energy and Thermodynamic Equilibrium . . . . .	4
2.1.1. Necessary conditions . . . . .	5
2.1.2. Sufficient conditions . . . . .	6
2.2. Thermochimica Integration in MOOSE . . . . .	6
2.2.1. MOOSE Objects for Thermochimica Calculations . . . . .	7
2.2.2. Finite Volume Support and Block Restrictions for Thermochimica . . . . .	7
2.2.3. Thermochimica multi-threading support . . . . .	8
2.3. Thermochimica Integration Test Cases . . . . .	9
2.3.1. $\text{BeF}_2 - \text{LiF}$ phase diagram . . . . .	9
3. POISSON-NERNST-PLANCK MODEL FOR CORROSION	11
3.1. Thermodynamic Consistency . . . . .	11
3.2. Butler-Volmer Equation for Electrochemical Kinetics . . . . .	11
3.3. Tafel Equations for High Overpotentials . . . . .	13
3.4. Tafel Plots in Corrosion Engineering . . . . .	14
3.5. Thermodynamically and Asymptotically Consistent Model for the Butler-Volmer Equation .	15
3.5.1. Derivation of the Nernst Equation . . . . .	15
3.5.2. Derivation of the Tafel Equations . . . . .	16
3.5.3. Modeling Species Leaching . . . . .	16
3.5.4. Modeling Species Plating . . . . .	19
3.5.5. Model for the Exchange Current Density . . . . .	21
3.6. Verification Cases . . . . .	22
3.6.1. Verification Case 1: Single Nickel Electrode . . . . .	23
3.6.2. Verification Case 2: Single Ni Electrode with Varying Electrode Potential due to Temperature . . . . .	24
3.6.3. Verification Case 3: Double Ni-Zn Electrode with Varying Electrode Potentials due to Temperature . . . . .	25
3.6.4. Verification Case 4: Grid Convergence Study for the Butler-Volmer Equation Coupled with the Poisson Equation for Electric Potential . . . . .	26
3.7. Full Poisson-Nernst-Planck Model . . . . .	27
3.7.1. Species Transport Equations . . . . .	27
3.7.2. Electric Potential Equation . . . . .	27
3.7.3. Energy Conservation Equation . . . . .	28
3.7.4. Fluid Flow Equations in the Liquid Phase . . . . .	28
3.7.5. Boundary Conditions at the Solid-Liquid Interface . . . . .	28
3.8. Verification of the Poisson-Nernst-Planck Model . . . . .	29
4. COUPLED LIQUID-GAS SPECIES TRANSPORT IN MOLTEN SALT REACTORS	31
4.1. Two-Phase Flow Modeling Using the Mixture Model . . . . .	31
4.1.1. Governing Equations . . . . .	31

4.1.2.	Definition of Mixture Variables	31
4.1.3.	Interfacial Momentum Transfer	32
4.1.4.	Interface Area Tracking	32
4.1.5.	Closure Relations	32
4.1.6.	Numerical Solution	33
4.2.	Species Transport Between Liquid and Gas Phases	33
4.2.1.	Governing Equations for Species Transport	33
4.2.2.	Interphase Mass Transfer	33
4.2.3.	Diffusive Fluxes	35
4.2.4.	Numerical Solution	35
5.	MOLTEN SALT REACTOR MULTI-REGION DEPLETION ANALYSES CAPABILITIES	35
5.1.	Improvements in Bateman multi-region modeling	35
6.	DEMONSTRATION CASES	38
6.1.	Validation of the Poisson-Nernst-Planck Model Using Experimental Data	38
6.2.	2D Molten Salt Loop with Two-Phase Flow	41
6.3.	3D Molten Salt Natural Convection Loop	52
7.	FULL MSR LOOP DEMONSTRATION CASES	57
7.1.	Lotus Molten Salt Reactor	58
7.2.	Molten Salt Reactor Experiment	61
8.	CONCLUSIONS	71
9.	FUTURE WORK	72
10.	REFERENCES	73

## FIGURES

Figure 1. Binary phase diagram of the BeF <sub>2</sub> –LiF system as evaluated in MSTDB-TC. . . . .	9
Figure 2. Thermochemical predictions of phase stability regions of various phases in BeF <sub>2</sub> –LiF system. . . . .	10
Figure 3. Tafel plot illustrating the anodic and cathodic branches used to determine the corrosion potential and current density. . . . .	15
Figure 4. Manufactured solution fields with $\tau = 1$ and $\varepsilon = 1$ : (a) concentration field $c_0(x, y)$ , (b) concentration field $c_1(x, y)$ , (c) electric potential $\phi(x, y)$ . . . . .	30
Figure 5. Convergence study for the PNP model implementation. The plot shows the $L_2$ norm of the error versus mesh size $\ \Delta x, \Delta y\ $ , indicating second-order convergence. . . . .	30
Figure 6. Schematic nuclide transfer diagram for the four-region depletion implementation. . . . .	37
Figure 7. Natural convection corrosion loop experiment for validating flow-accelerated corrosion models. . . . .	38
Figure 8. Thermal-hydraulic fields for steady-state operation of the natural convection loop. . . . .	39
Figure 9. Results for the Poisson-Nernst-Planck (PNP) model. . . . .	40
Figure 10. Geometry for the 2D natural convection flow loop demonstration case. . . . .	42
Figure 11. Temperature distribution for the system operating at steady-state for the 2D natural convection flow loop demonstration case. . . . .	43
Figure 12. Void fraction in the two-phase natural convection loop demonstration case at different time steps: $t = 0$ s (left), $t = 20$ s (center), $t = 1000$ s (right). . . . .	43
Figure 13. Velocity field for the system operating at steady-state for the 2D natural convection flow loop demonstration case. . . . .	44
Figure 14. Interface area concentration for the system operating at steady-state for the 2D natural convection flow loop demonstration case. . . . .	45
Figure 15. Chromium distribution after 1,000 hours of operation in the demonstration case for a 2D molten salt loop with two-phase flow. The central frame shows the distribution of chromium dissolved in the liquid phase, while the surrounding panels show the percent concentration of chromium in the pipe. Note that a different scale is used for the concentration in the pipe for visualization purposes. . . . .	46
Figure 16. Iron distribution after 1,000 hours of operation in the demonstration case for a 2D molten salt loop with two-phase flow. The central frame shows the distribution of iron dissolved in the liquid phase, while the surrounding panels show the percent concentration of iron in the pipe. Note that a different scale is used for the concentration in the pipe for visualization purposes. . . . .	47
Figure 17. Nickel distribution after 1,000 hours of operation in the demonstration case for a 2D molten salt loop with two-phase flow. The central frame shows the distribution of nickel dissolved in the liquid phase, while the surrounding panels show the percent concentration of nickel in the pipe. Note that a different scale is used for the concentration in the pipe for visualization purposes. . . . .	48
Figure 18. Corrosion product distribution in the gas phase for the system operating at steady-state for the 2D natural convection flow loop demonstration case including chromium (left), iron (center), and nickel (right). . . . .	49
Figure 19. Thermochemical predictions of phase stability and speciation in demonstration loop. . . . .	50
Figure 20. Thermochemical predicted element potentials in molten salt phase of demonstration loop. . . . .	51
Figure 21. Temperature distribution during steady-state operation of the 3D natural convection loop demonstration case. . . . .	53
Figure 22. Chromium profile in the molten salt loop pipe for the 3D natural convection loop demonstration case after 100 days of operation. . . . .	54

Figure 23. Iron profile in the molten salt loop pipe for the 3D natural convection loop demonstration case after 100 days of operation. . . . .	55
Figure 24. Nickel profile in the molten salt loop pipe for the 3D natural convection loop demonstration case after 100 days of operation. . . . .	56
Figure 25. Concentration in the molten salt of corrosion products after 100 days of operation for the 3D natural convection loop demonstration case, including Chromium (left), Iron (center), and Nickel (right). . . . .	57
Figure 26. Geometry for the 3D Lotus Molten Salt Reactor . . . . .	58
Figure 27. Thermochemically important fields within L-MSR at steady-state operation: (a) temperature [K], (b) pressure [Pa], (c) chemical potential of chloride ( $\text{Cl}^-$ ) [ $\text{J mol}^{-1}$ ]. . . . .	59
Figure 28. Volatilization of noble gases and chemical species within L-MSR at steady-state operation: (a) ideal gas phase distribution [ $\text{mol m}^{-3}$ ], (b) $\text{RbCl}$ gaseous species distribution [ $\text{mol m}^{-3}$ ], (c) $\text{CsI}$ gaseous species distribution [ $\text{mol m}^{-3}$ ]. . . . .	60
Figure 29. Changing chemical potentials of fuel salt constituents during depletion in L-MSR . . . . .	60
Figure 30. Increasing volatilization of chemical species due to depletion in L-MSR. . . . .	61
Figure 31. Axisymmetric Griffin-Pronghorn-Thermochimica model developed for MSRE. . . . .	62
Figure 32. MSRE Pump Bowl Schematic[1]. . . . .	63
Figure 33. Thermochemically important fields within MSRE at steady-state operation: (a) temperature [K], (b) pressure [Pa], (c) chemical potential of fluoride ( $\text{F}^-$ ) [ $\text{J mol}^{-1}$ ]. . . . .	64
Figure 34. Circulating helium void in MSRE at steady-state operation: (a) ideal gas phase distribution [ $\text{mol m}^{-3}$ ], (b) ideal gas void volume [ $\text{m}^3$ ], (c) effective circulating void mass transfer source term for fractional volatilization of chemical species [ $\text{m}^3$ ]. . . . .	65
Figure 35. Fission product element fields in MSRE at steady-state operation: (a) concentration of rubidium in the liquid phase [ $\text{mol m}^{-3}$ ], (b) concentration of rubidium in the gaseous phase [ $\text{mol m}^{-3}$ ], (c) concentration of iodine in the liquid phase [ $\text{mol m}^{-3}$ ], (d) concentration of iodine in the gaseous phase [ $\text{mol m}^{-3}$ ], (e) concentration of cesium in the gaseous phase [ $\text{mol m}^{-3}$ ], (f) concentration of cesium in the gaseous phase [ $\text{mol m}^{-3}$ ]. . . . .	66
Figure 36. Fluorination pulse transient in MSRE: (a) Total fluorine gas [ $\text{mol m}^{-3}$ ] (from left to right) at 0.75 s, 1.00 s, 1.25 s, and 1.50 s respectively, (b) Total void [ $\text{mol m}^{-3}$ ] (from left to right) at 0.75 s, 1.00 s, 1.25 s, and 1.50 s respectively, (c) Total iodine gas [ $\text{mol m}^{-3}$ ] (from left to right) at 0.75 s, 1.00 s, 1.25 s, and 1.50 s respectively. . . . .	68
Figure 37. Changing fluoride potential [ $\text{J mol}^{-1}$ ] due to fluorination pulse transient in MSRE (from left to right): (a) at 1.00 s, (b) at 10.00 s, (c) at 20.00 s, (d) at 30.00 s, (e) at 40.00 s, (f) at 50.00 s. . . . .	69
Figure 38. Circulating iodine gas [ $\text{mol m}^{-3}$ ] due to fluorination pulse transient in MSRE (from left to right): (a) at 1.00 s, (b) at 10.00 s, (c) at 20.00 s, (d) at 30.00 s, (e) at 40.00 s, (f) at 50.00 s. . . . .	70

## TABLES

Table 1.	Constants used in the verification cases. . . . .	23
Table 2.	Comparison of Nernst and computed values for liquid over solid Ni concentration ratios ( $C_l/C_s$ ) at different temperatures with constant electrode potential. . . . .	24
Table 3.	Comparison of Nernst and computed values for $C_l/C_s$ at different temperatures with varying electrode potential. . . . .	25
Table 4.	Reaction potentials and concentration ratios for Ni and Zn at different temperatures. . . . .	25
Table 5.	Mesh size refinement study with Grid Convergence Index (GCI) for $Zn_l/Zn_s$ and $Ni_l/Ni_s$ . .	26
Table 6.	Comparison of predicted and measured temperatures in the natural convection loop at steady state. . . . .	39
Table 7.	Comparison of predicted and measured concentrations of chromium and iron in the molten salt at the end of the experiment (in weight parts per million [wppm]). . . . .	40
Table 8.	Problem parameters for the molten salt loop with two-phase flow for the 2D natural convection flow loop demonstration case. . . . .	41
Table 9.	Problem parameters for the 3D molten salt natural convection loop demonstration case. . .	52
Table 10.	Key modeling parameters of the L-MSR . . . . .	59

# Integration of Thermochimica into MOOSE-based Molten Salt Reactor Loop Simulations

## 1. INTRODUCTION

Molten Salt Reactors (MSRs) are an advanced nuclear technology with promising attributes such as inherent safety, high thermal efficiency, and the ability to operate at elevated temperatures. A critical aspect of MSR operation, addressed in this milestone, is the tracking of species and the accurate modeling of corrosion processes within the reactor [2]. In MSRs, the fuel is dissolved in molten salt, which interacts with reactor materials, leading to the release of corrosion products into the salt [3]. These corrosion products, as well as fission products, can accumulate over time and significantly impact reactor performance, safety, and material longevity. Hence, the continuous tracking of species in both liquid and gas phases is essential to optimize reactor operation and minimize material degradation.

Corrosion in MSRs occurs due to interactions between molten salt and structural materials, particularly the dissolution of metals like chromium, iron, and nickel into the salt [4]. This process leads to gradual degradation of reactor components, reducing their structural integrity. The high operating temperatures and corrosive chemical environment inside MSRs exacerbate these effects, making corrosion modeling and prediction crucial for extending the operational life of reactor materials and preventing unplanned downtime or costly repairs. Effective modeling of corrosion processes, therefore, is essential for reliable long-term reactor operation [5].

The transport of corrosion products within MSRs can also affect the neutronics and thermal performance of the system [6]. These products are carried by the flowing molten salt, potentially leading to localized damage in different regions of the reactor. Tracking the migration and concentration of these species over time is vital for improving reactor design and mitigating risks associated with uneven material wear and corrosion-induced failure.

As both corrosion and fission products accumulate in the molten salt, additional phenomena such as volatility and precipitation arise [7]. Volatile species, particularly fission products like iodine and cesium, can escape the molten salt and enter the gas phase, contaminating the reactor system and affecting material degradation. Precipitation of certain species can also occur when concentrations exceed solubility limits, leading to solid deposits that reduce heat transfer efficiency and accelerate corrosion. To fully understand these effects, it is critical to track volatile species in the gas phase, as their migration through the reactor can lead to localized corrosion in cooler regions and complicate purification processes. Modeling the transport and behavior of volatile species ensures reactor safety and longevity, particularly in systems where off-gas extraction is implemented to remove volatile products.

Pronghorn, a MOOSE-based computational fluid dynamics (CFD) tool, is designed to model fluid flow and heat transfer in advanced reactors like MSRs [8]. Pronghorn's CFD capabilities enable the simulation of complex geometries and thermal-hydraulic phenomena, providing a robust framework for modeling both single-phase and multi-phase flows in MSRs. It employs various turbulence models, such as Reynolds-Averaged Navier-Stokes (RANS), to capture fluid behavior in reactor components, which is critical for accurately predicting void fraction generation, species transport, and the impacts of flow on corrosion processes.

Thermochimica is a Gibbs energy minimizer that performs thermochemical equilibrium calculations for multicomponent systems [9]. In the context of MSRs, Thermochimica predicts the stable phases, chemical potentials, and interactions between dissolved species and corrosion products within the molten salt. By accounting for non-ideal solution behavior and phase transitions, Thermochimica provides valuable insights

into the chemical speciation of molten salt mixtures under reactor conditions. Its ability to model the chemical reactions between molten salt components and structural materials makes it essential for accurately predicting corrosion behavior and material degradation.

The integration of Thermochimica into the MOOSE framework and its coupling with Pronghorn forms a powerful tool for species tracking in MSRs. By combining Pronghorn's CFD capabilities with Thermochimica's thermodynamic equilibrium calculations, this integrated framework can simulate species transport and chemical reactions in the reactor's environment. This coupling enables more accurate predictions of species concentrations, phase equilibria, and the distribution of corrosion products, providing operators with crucial information for optimizing reactor performance and mitigating material degradation.

A significant advancement in this milestone is the inclusion of two-phase flow capabilities within the Pronghorn-Thermochimica framework. Two-phase flow, where gas bubbles coexist with liquid molten salt, plays a crucial role in species transport, particularly for volatile products. Gas bubbles alter the flow field, increase turbulence, and provide additional interfaces for mass transfer between the liquid and gas phases. As volatile species transfer from the liquid to the gas phase, this two-phase flow accelerates the removal of these species from specific regions of the reactor, influencing both species migration and corrosion dynamics.

The addition of two-phase flow modeling is vital for understanding the behavior of corrosion products and fission species in dynamic reactor environments [10]. In regions where gas bubbles form, mass transfer between the molten salt and gas bubbles becomes a dominant factor in species transport. This not only affects the corrosion patterns but also the rate at which species accumulate or are removed from reactor components. Two-phase flow modeling enhances the overall understanding of the chemical environment in MSRs and helps inform design strategies aimed at minimizing corrosion and extending component life.

Despite the significant advancements provided by coupling Pronghorn and Thermochimica, several limitations remain in modeling corrosion in MSRs. One limitation is the challenge of accurately capturing the localized nature of corrosion, especially in areas with high strain or uneven temperature distributions. Furthermore, the models may simplify the complex interactions between species in non-ideal molten salt solutions, potentially introducing inaccuracies in the predictions of species concentrations. Another limitation is the difficulty in modeling long-term material degradation and the cumulative effects of corrosion over extended reactor operations. While short-term predictions are accurate, long-term simulations are computationally expensive and may not capture the full extent of corrosion effects.

Simplifications in tracking species transitions between liquid and gas phases also present challenges. The current models may not fully account for detailed interfacial mass transfer processes, which can lead to underestimating species transport rates and their impact on reactor corrosion. In addition, the limited availability of experimental validation data for specific MSR designs makes it difficult to assess the robustness of the predictions. Finally, the computational cost of fully coupled Pronghorn-Thermochimica simulations can restrict their use for high-resolution, long-term analyses, making it necessary to balance accuracy and feasibility in large-scale simulations.

The Poisson-Nernst-Planck (PNP) model, combined with Butler-Volmer kinetics [11], was introduced into MOOSE to better model the electrochemical aspects of corrosion in MSRs. The PNP model tracks the movement of ions in the molten salt, predicting how electric currents and concentration gradients drive the transport of corrosion products. Coupled with the Butler-Volmer formulation, which describes the kinetics of electrochemical reactions, this approach allows for more accurate simulation of corrosion rates and species transport at the material interfaces, particularly in high-temperature, corrosive environments like MSRs.

The PNP and Butler-Volmer models significantly improve the ability to predict corrosion behavior in MSRs by accounting for the electrochemical effects on species transport and leaching. By coupling these models with Pronghorn's flow field and temperature distributions, the simulation framework can predict how

corrosion products are transported from structural materials into the molten salt and how they migrate within the reactor. This integrated approach provides a deeper understanding of corrosion processes and offers valuable insights for optimizing reactor design and operation.

In addition to species transport, depletion modeling plays a critical role in understanding the long-term behavior of MSRs. Depletion refers to the continuous change in isotopic composition due to nuclear reactions and radioactive decay, which affects both neutronics and species behavior over time. Accurate depletion modeling is crucial for tracking fuel evolution, predicting how isotopic changes influence corrosion rates, and ensuring safe reactor operation. Griffin's depletion capabilities have been integrated with the Pronghorn-Thermochimica framework to model isotopic changes and their impact on species transport and corrosion.

The integration of these depletion models with species tracking and thermochemical calculations ensures that the framework can simulate not only the current state of the reactor but also its evolution over time. This is particularly important for MSRs, where fuel is cycled through the reactor, and isotopic changes directly affect the transport and behavior of corrosion products. By incorporating multi-region depletion models, the framework captures the complex interactions between fuel evolution, species migration, and corrosion in a dynamic reactor environment.

This milestone demonstrates the advancement of species tracking and corrosion modeling in Molten Salt Reactors (MSRs) by integrating multiple physics and computational tools. The key developments and accomplishments can be summarized as follows:

- **Coupling Thermochimica with Pronghorn:** Integrated Thermochimica, a Gibbs energy minimizer, with the Pronghorn code to model the chemical speciation and thermodynamic equilibrium of multi-component systems in MSRs. This allows for accurate prediction of phase equilibria and the impact of species transport on reactor behavior.
- **Two-phase flow integration:** Developed two-phase flow capabilities in Pronghorn for tracking volatile species and their transfer between liquid and gas phases and coupled them with Thermochimica for predicting the volatilization rate, which is crucial for understanding the behavior of corrosion products and volatile fission products in MSRs.
- **Initial implementation of multiphysics model for species tracking in MSRs in MOOSE:** Established an initial framework for comprehensive multiphysics studies of species tracking in MSRs that integrates thermal-hydraulics, chemical speciation, and corrosion kinetics to accurately model the long-term behavior of MSRs under realistic operational conditions.
- **Species transport modeling in MSRs:** Enhanced tracking of corrosion and fission products in both liquid and gas phases using a combination of the Poisson-Nernst-Planck (PNP) model, Butler-Volmer kinetics, and two-phase flow modeling.
- **Multi-region depletion modeling:** Advanced Bateman equation-based depletion modeling to track the isotopic evolution in MSRs, incorporating chemical reactions and mass transfer between different regions of the reactor system.
- **Validation of the Poisson-Nernst-Planck model:** Validated the PNP model against experimental data from an Oak Ridge National Laboratory's natural convection loop, demonstrating the accuracy of flow-accelerated corrosion predictions in a FLiNaK molten salt system.
- **3D and 2D natural convection loop simulations:** Demonstrated both 2D and 3D modeling of natural convection loops with molten salt, simulating the interaction of species transport, corrosion, and flow behavior in realistic geometries.

- **Full MSR loop demonstration:** Demonstrated species tracking in full loop MSR simulation using as examples the Molten Salt Reactor Experiment and the Molten Chloride Reactor Experiment.

The accomplishments presented in this milestone enhance the predictive capabilities of NEAMS tools for MSR design and operation, addressing critical challenges in species tracking, corrosion, and depletion analysis as outlined in the original milestone description.

## 2. MOLTEN SALT THERMOCHEMISTRY CAPABILITIES IN THERMOCHIMICA AND MOOSE

Nuclear reactors and materials are complex multicomponent systems which undergo continuous compositional evolution under the reactor environment. This evolution and the environmental conditions affect the stable phases, speciation and material properties. Representing the thermochemistry and phase evolution for relevant molten salt constituents is imperative for design, development, deployment, and safe operation of various advanced reactors including the Molten Salt Reactors (MSRs). The CALPHAD (Calculation of Phase Diagrams) method utilizes Gibbs energy functions to represent the thermodynamic properties of systems with multiple elements. For non-ideal solutions, excess Gibbs energy models account for deviations from ideal behavior based on pressure, temperature, and composition. These models are usually fitted to experimental phase and thermochemical data to determine optimal Gibbs energy parameters. Once assessed, these Gibbs energy functions and models can be used to predict phase equilibria and other thermodynamic properties.

Thermodynamic equilibrium calculations offer a quantitative approach to predict phase distribution, chemical potentials, and material properties (e.g., heat capacity, oxygen-to-metal ratio) as the composition evolves. By coupling thermodynamics with multiphysics codes, we can enhance predictions of nuclear material performance and improve safety. These calculations are based on minimizing the integral Gibbs energy of a closed system at constant temperature and hydrostatic pressure. From a numerical point of view, the objective of computing thermochemical equilibrium is to determine a unique combination of phases and their composition that yields a global minimum in the integral Gibbs energy subject to various linear and non-linear equality constraints.

### 2.1. Gibbs Energy and Thermodynamic Equilibrium

The integral Gibbs energy of a multicomponent multiphase system is represented as<sup>1</sup>:

$$G = RT \left( \sum_{\lambda=1}^{\Lambda} n_{\lambda} \sum_{i=1}^{N_{\lambda}} x_{i(\lambda)} \tilde{\mu}_i + \sum_{\omega=1}^{\Omega} n_{\omega} \tilde{\mu}_{\omega} \right), \quad (1)$$

where

- $R$  represents the universal gas constant ( $8.3145 \text{ J mol}^{-1} \text{ K}^{-1}$ ),
- $T$  is the temperature (K),
- $n_{\lambda}$  is the molar amount of solution phase  $\lambda$  (mol),

---

<sup>1</sup>The  $RT$  factor is not included in the equations below as the non-dimensional form of the chemical potentials is used. This is preferred from the computational perspective as it reduces the number of floating point operations at each iteration.

- $x_{i(\lambda)}$  is the mole fraction of species  $i$  of solution phase  $\lambda$ ,
- $\tilde{\mu}_i$  is the dimensionless chemical potential of species  $i$  of solution phase  $\lambda$ ,
- $n_\omega$  is the molar amount of stoichiometric phase  $\omega$  (mol),

The chemical potential is a measure of the change of the Gibbs energy of a system by the introduction of a substance. Mathematically, the chemical potential of a species  $i$  is defined as:

$$\tilde{\mu}_i = \frac{1}{RT} \left( \frac{\partial G}{\partial n_i} \right)_{T,P,n_{j \neq i}}, \quad (2)$$

and, for the species of an ideal phase, the non-dimensional form of the chemical potential incorporates the reference Gibbs energy of pure species,  $g_{i(\lambda)}^0$ , and the entropic contribution due to mixing as a function of its mole fraction:

$$\tilde{\mu}_i = \underbrace{g_{i(\lambda)}^0}_{\mu_{i(\lambda)}^0} + \underbrace{\ln x_{i(\lambda)}}_{\mu_{i(\lambda)}^{id}}. \quad (3)$$

For non-ideal solution phases, the chemical potential also includes the partial molar excess Gibbs energy of mixing,  $\tilde{\mu}_{i(\lambda)}^{ex}$ , to account for non-ideal mixing:

$$\tilde{\mu}_i = \underbrace{g_{i(\lambda)}^0}_{\mu_{i(\lambda)}^0} + \underbrace{\ln x_{i(\lambda)}}_{\mu_{i(\lambda)}^{id}} + \tilde{\mu}_{i(\lambda)}^{ex}. \quad (4)$$

While the chemical potential of stoichiometric phases does not include a composition dependent term, the partial molar excess Gibbs energies of mixing for non-ideal solution models depend on the mixing model employed e.g. the Modified Quasichemical Model [12–16], the Compound Energy Formalism [17], etc. Identifying the stable phase assemblage can be broken into a set of necessary and sufficient conditions that must be satisfied

### 2.1.1. Necessary conditions

1. *Conservation of mass* requires that the mass of element  $j$ ,  $b_j$ , must satisfy the following mass balance equation

$$b_j = \sum_{\lambda=1}^{\Lambda} n_\lambda \sum_{i=1}^{N_\lambda} x_{i(\lambda)} v_{i,j} + \sum_{\omega=1}^{\Omega} n_\omega v_\omega, \quad (5)$$

where  $v_{i,j}$  and  $v_\omega$  represent the stoichiometric coefficients of element  $j$  in solution phase species  $j$  and stoichiometric phase  $\omega$  respectively.

2. *Gibbs' phase rule*, which defines the thermodynamic degrees of freedom of the system must also be satisfied:

$$F = C - \Phi + 2 + \Xi \geq 0, \quad (6)$$

where  $F$  represents the degrees of freedom,  $C$  denotes the number of components in the system,  $\Phi$  denotes the number of phases and  $\Xi$  denotes the electrochemical terms.

3. *Gibbs' criteria* for equilibrium requires that the Gibbs energy of a system be at a global equilibrium. In equivalent terms, the chemical potential for each system component must have the same value in all stable phases within the system [18], where the chemical potential of any constituent in a stable phase can be defined as a linear function of the element potentials,  $\Gamma_j$ , as

$$\mu_i = \sum_{j=1}^C \nu_{i,j} \Gamma_j. \quad (7)$$

### 2.1.2. Sufficient conditions

The necessary conditions for thermodynamic equilibrium require that the chemical potentials of all stable solution phase species and stoichiometric phases abide by the above equality, which is equivalent to Gibbs energy of the system being at a local minimum, and that the conservation of mass and the Gibbs phase rule are satisfied. The sufficient condition requires that all the metastable phases abide by the following conditions [19]:

$$\pi_\lambda = \min_\lambda \sum_{i=1}^{N_\lambda} x_{i(\lambda)} \left( \mu_{i(\lambda)} - \sum_{j=1}^C \nu_{i,j} \Gamma_j \right), \quad (8)$$

that is, there must exist a Gibbs' plane such that the element potentials lie on the plane and the chemical potentials of all the species lie on or above the plane and the mole fraction of the species must satisfy the following constraints

$$\begin{aligned} \sum_{i=1}^{N_\lambda} x_{i(\lambda)} &= 1 \\ x_{i(\lambda)} &\geq 0 \quad \forall i \\ F &\geq 0, \end{aligned} \quad (9)$$

that is, the sum of mole fraction of all the species in a phase  $\lambda$  must be unity, the individual mole fractions must be greater than or equal to zero and the degree of freedom of the system calculated according to Gibbs' phase rule must be greater than or equal to zero. The aforementioned conditions are used in the Gibbs energy minimizer to find a unique combination of phases that are stable in the system.

The Molten Salt Thermal Properties Database-Thermochemical (MSTDB-TC) is a comprehensive collection of thermodynamic models of molten salt systems and contains Gibbs energy models for both fluoride and chloride molten salts and related systems of interest with respect to molten salt technology. These models can be used to determine chemical activities, vapor pressures, corrosion potentials, etc. by identifying the equilibrium state of the system. Doing so requires the use of a Gibbs energy minimizer, for which several commercial and open source codes such as FactSage, ThermoChimica and PyCalphad are available.

## 2.2. ThermoChimica Integration in MOOSE

The open-source Gibbs energy minimizer ThermoChimica has been integrated into the chemical reactions module of MOOSE allowing direct coupling of GEM calculations in MOOSE-based simulations and enabling the use of MSTDB-TC data to predict the thermodynamic properties. In MOOSE, ThermoChimica has been integrated through a combination of the `ChemicalComposition` action and the `ThermoChimicaData` user object template class.

### **2.2.1. MOOSE Objects for Thermochimica Calculations**

The `ChemicalComposition` action is the user-facing MOOSE object used to initiate the framework for thermochemical calculations and it creates required variables, reads the thermodynamic database for material system, and sets the units for temperature, pressure, and elemental composition. It can optionally initialize the amounts of elements used in the model. The `ChemicalComposition` action is also used to specify lists of chemical phases and chemical species for which concentrations should be output at each timestep and verifies them against the specified database. Finally, the action creates all auxiliary variables needed for output of phase concentration data, chemical potentials, vapor pressures, etc.

`ThermochimicaData` is the template base class used to specialize `ThermochimicaElementData` and `ThermochimicaNodalData`. These are MOOSE user objects that execute Thermochimica and provide access to equilibrium data at elements and nodes respectively. In addition, the user object also saves and loads the re-initialization data when Thermochimica's reinitialization scheme is used.

### **2.2.2. Finite Volume Support and Block Restrictions for Thermochimica**

The MOOSE Navier-Stokes module is a library for the implementation of simulation tools that solve the Navier-Stokes equations using either the continuous Galerkin finite element (CGFE) or finite volume (FV) methods with the FV implementation using a colocated grid with variable degrees of freedom stored on elements rather than on the nodes. While the finite element based simulations were previously supported by the MOOSE objects for running Thermochimica, integrating Thermochimica in full-loop MSR simulations required additional support for the finite volume method. To this end, the original implementation of `ThermochimicaNodalData` was refactored into `ThermochimicaData` template class described above, adding a specialization of the object that supports the elemental FV variables. To keep the `ChemicalComposition` action as the user facing MOOSE object that automatically sets up the required the `is_fv` parameter was added. This allows users to select at the runtime the variable type that will be used and the action creates the required variables.

Complex simulations often involve multiple materials localized to different subdomains. In the MOOSE framework, block restrictions are used to define specific regions within the computational domain where certain operations or properties should be applied. By applying block restrictions, users can optimize computational resources, enhance performance, and ensure that the simulation accurately reflects the physical setup of the problem. Block restrictions are typically defined in the input file using the `block` parameter, allowing for precise control over where boundary conditions, initial conditions, and other simulation parameters are enforced. In `ChemicalComposition` action, the `block` parameter can be used to specify subdomains with different material compositions. However, Thermochimica runs point calculations based on a specific parsed database and to support applications where separate databases must be used for different blocks, separate instances of Thermochimica must be run over each of block with restrictions. This is achieved through the use of input file subblocks of the `ChemicalComposition`. A separate user object is created for each subblock with block restrictions and a separate instance of Thermochimica is run for each user object. When no block restrictions are applied, a single user object is instantiated. `ChemicalComposition` subblocks also enable the use of finite volume and finite element variables on separate blocks. As an example, the fluid flow in a pipe can be simulated with the pipe material properties in an alloy database with elements discretized using the finite element scheme while the fluid domain could be modeled using finite volume discretization and the properties can be calculated using a separate database. An example input is shown in Listing 1.

Listing 1. A example of ChemicalComposition action with subblock restrictions

```
[ChemicalComposition]
  tunit = K
  punit = atm
  munit = moles
  temperature = T
  [block_0]
    block = '0'
    elements = 'Fe Cr'
    thermofile = FeCr.dat
    output_phases = 'FCCN BCCN HCPN'
    output_species = 'ALL'
    is_fv = false
    output_species_unit = mole_fraction
  []
  [block_1]
    block = '1'
    elements = 'F Be Li Fe Cr'
    thermofile = MSTDB_TC_Fluorides.dat
    output_phases = 'MSFL gas_ideal'
    output_species = 'MSFL:Cr MSFL:F'
    is_fv = true
    output_species_unit = moles
  []
[]
```

### 2.2.3. Thermochimica multi-threading support

In MOOSE simulations with thermodynamic solves, the Thermochimica computation makes up a large fraction of the total runtime. Parallel computing using message passing interface (MPI) is one approach to reduce the wall time of these calculations, by parallelizing over material points. However, many preconditioners (such as the direct solve based on LU-decomposition) have limited scalability, are not practical for small numbers of degrees of freedom, or require more iterations, which in turn increase the number of Thermochimica solves. A more promising acceleration approach for systems in those cases would be multi-threading. With multi-threading the non-linear solves would still only be parallelized over the MPI processes, while MOOSE material evaluation would be distributed over multiple light weight processes called threads.

Thermochimica, however, is not designed for parallel execution with threads, as all threads spawned by a process share a common memory space. In practice this means that any global data storage, such as global state variables, are shared between threads. Thermochimica is written in Fortran and utilizes legacy design patterns that take advantage of data sharing across subroutines through global variables. This approach makes it inherently unsuitable for multi-threaded execution, as multiple threads performing different calculations would overwrite each other's shared state variables constantly, leading to corrupted results.

In order to still support multi-threaded calculations with Thermochimica embedded in MOOSE applications we developed a workaround. Every thread launches a child process using the POSIX `fork()` system call. These child processes have their own separate memory space (a shallow copy of the parent process' memory space), which insulates the individual Thermochimica instances from each other. Under modern operating systems the memory space of a child process follows the *copy on write* paradigm, meaning that additional physical memory is only allocated when the child process makes any changes to memory locations. This causes the Thermochimica child processes to have minimal memory overhead.

Each thread also allocates a buffer of shared memory, using the `mmap()` system call, and a bidirectional UNIX communication socket, using the `socketpair()` system call, for communication with the child process. When a new ThermoChimica solve is required, the MOOSE application thread writes temperature, pressure, and mole fractions to the shared memory segment, which can be accessed by both parent and child process, and sends a trigger signal over the UNIX socket using the `write()` system call. The child process receives the signal using `read()`, calls the ThermoChimica library with the temperature, pressure, and mole fractions retrieved from the shared memory, and upon completion of the thermochemistry solve, writes the results back into the shared memory, and sends a trigger over the UNIX socket to the parent process. The parent process then retrieves the data and thus the calculation step is completed.

As an added benefit the encapsulation of ThermoChimica library execution into separate processes has also enabled us to support block restricted calculations with separate database files. For example, one region of a MOOSE simulation could require a thermochemistry solve of a molten salt speciation, where another region could involve the calculation of stable phases in an evolving alloy.

## 2.3. ThermoChimica Integration Test Cases

### 2.3.1. $\text{BeF}_2 - \text{LiF}$ phase diagram

To test the capabilities developed through the integration of ThermoChimica in MOOSE, the phase diagram of the  $\text{BeF}_2 - \text{LiF}$  binary system was reproduced by executing ThermoChimica on a MOOSE mesh with varying composition and temperature. Adaptive mesh refinement was used to reduce mesh size near phase boundaries and coarsen within single phase regions. The  $\text{BeF}_2 - \text{LiF}$  binary system has been widely assessed and is included in MSTDB-TC with a high confidence in the model. Figure 1 shows the phase diagram of the  $\text{BeF}_2 - \text{LiF}$  system as evaluated in MSTDB-TC and the ThermoChimica predicted phase stability regions are shown in Figure 2.

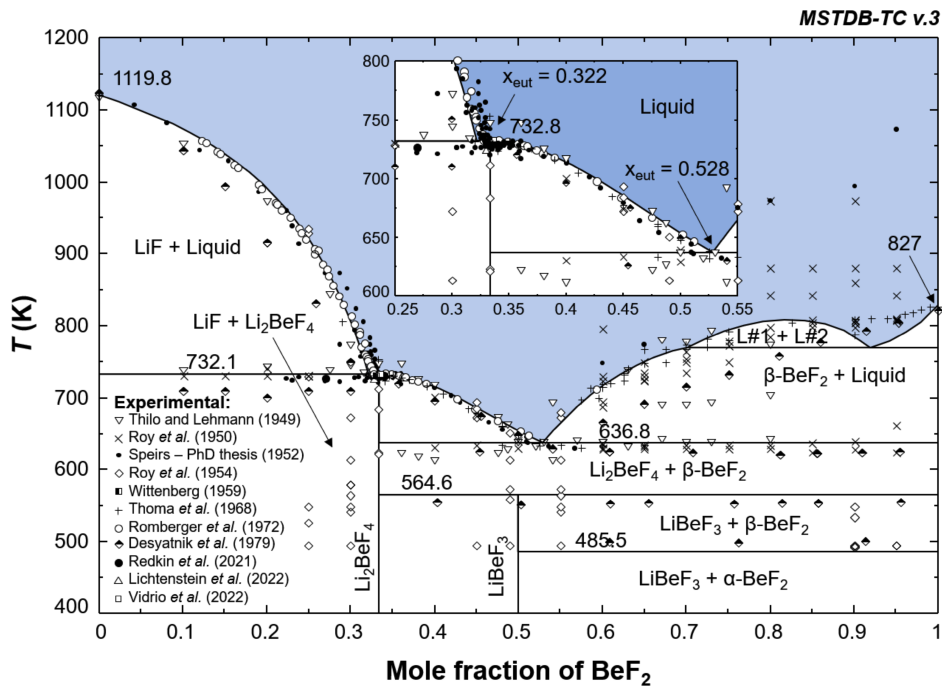


Figure 1. Binary phase diagram of the  $\text{BeF}_2 - \text{LiF}$  system as evaluated in MSTDB-TC.

The predictions of ThermoChimica show excellent agreement with the phase diagram and adaptive mesh refinement enables accurate capturing of the phase transition boundaries, including accurately capturing the eutectic transition compositions and temperatures. Though the region of dissociation (labeled as L $\equiv$ 1-L $\equiv$ 2) in the phase diagram appears to absent in ThermoChimica predictions, it has, in fact, been accurately captured. This apparent error can be attributed as an artifact of post processing. Since the region of dissociation contains the same liquid phase with two separate phase compositions, the post processing script classifies them as the same phase for the purpose of plotting their mole fractions. This results in the region being denoted with a phase composition of a single liquid phase in the phase diagram.

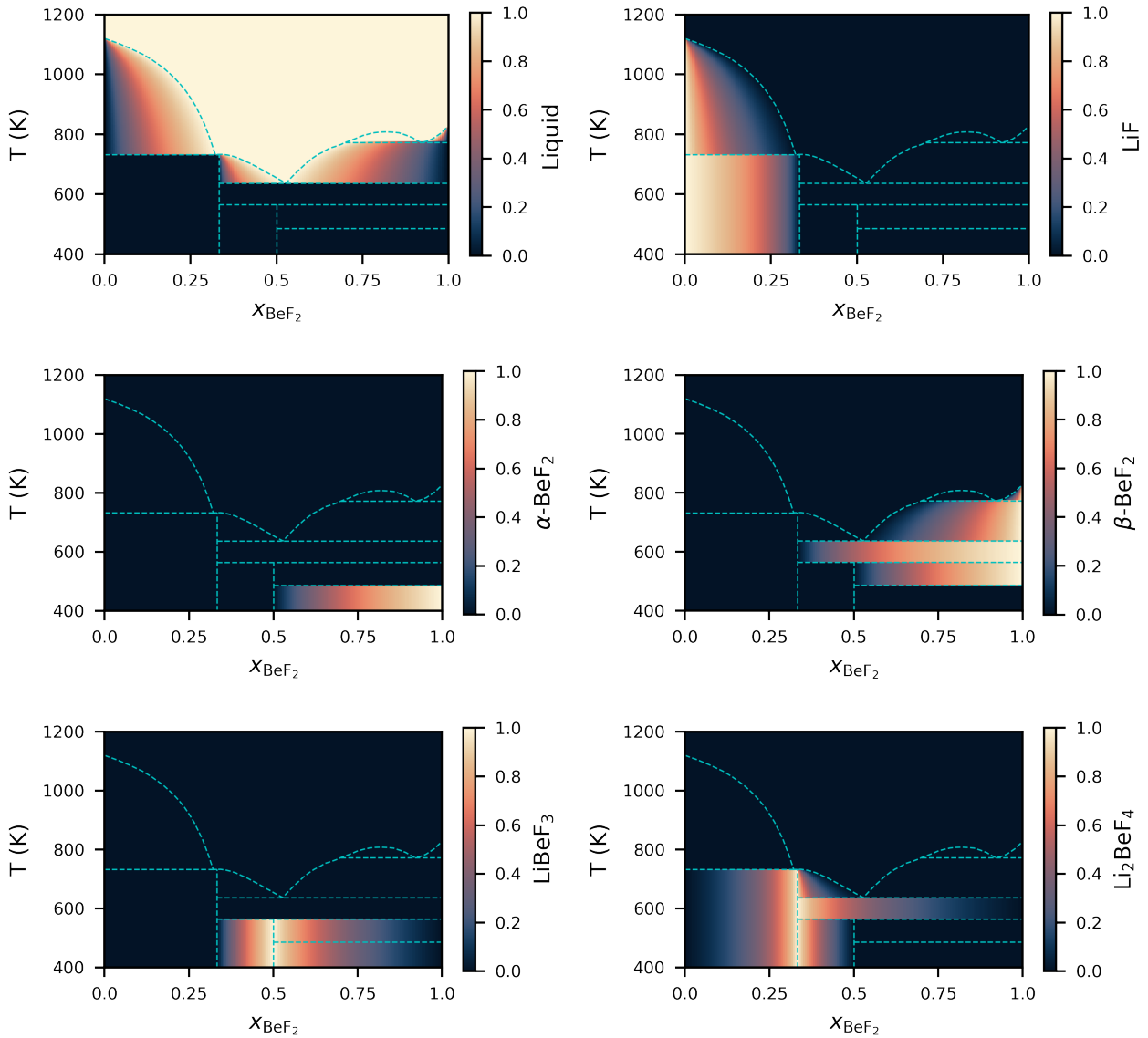


Figure 2. ThermoChimica predictions of phase stability regions of various phases in  $\text{BeF}_2$ – $\text{LiF}$  system. The cyan colored dashed lines represent the phase boundaries as reported in the phase diagram presented in Figure 1.

### 3. POISSON-NERNST-PLANCK MODEL FOR CORROSION

#### 3.1. Thermodynamic Consistency

Thermodynamic consistency in electrochemical reactions ensures realistic potentials and currents under specified conditions [20]. This is achieved by the Nernst equation, which sets the equilibrium potential:

$$E_{\text{eq}} = E^{\circ} + \frac{RT}{nF} \ln \frac{a_{\text{Red}}}{a_{\text{Ox}}} \quad (10)$$

where  $E^{\circ}$  is the standard electrode potential,  $R$  is the gas constant,  $T$  is the temperature,  $n$  is the number of moles of electrons transferred,  $F$  is the Faraday constant, and  $a_{\text{Red}}, a_{\text{Ox}}$  are the activities of the reduced and oxidized forms, respectively.

The equation illustrates how small variations in reactant concentrations can significantly affect the cell's potential, impacting performance and efficiency. The dependency on temperature and gas constant highlights the importance of controlling environmental conditions in electrochemical systems, especially in high-temperature applications like fuel cells.

#### 3.2. Butler-Volmer Equation for Electrochemical Kinetics

The Butler-Volmer equation provides a model that integrates both the thermodynamic and kinetic aspects of electrochemical reactions, describing how the current density  $i$  varies with overpotential  $\eta$  [21]:

$$i = i_0 \left[ \exp \left( \frac{\alpha_a n F \eta}{RT} \right) - \exp \left( -\frac{\alpha_c n F \eta}{RT} \right) \right] \quad (11)$$

where the symbols represent:

- $i$ : Current density ( $\text{A m}^{-2}$ ), indicating the amount of charge per unit area per unit time passing through a section of the electrode.
- $i_0$ : Exchange current density ( $\text{A m}^{-2}$ ), which is the current density at equilibrium (overpotential  $\eta = 0$ ), reflecting the intrinsic electrochemical activity of the electrode material.
- $\eta$ : Overpotential (V), the additional potential required to drive the reaction at a rate higher than its equilibrium rate, essentially the deviation from the equilibrium potential.
- $\alpha_a$  and  $\alpha_c$ : Anodic and cathodic transfer coefficients, dimensionless factors that indicate how the reaction rate changes with overpotential. These coefficients describe the distribution of the energy barrier between the forward and reverse reactions.
- $n$ : Number of electrons transferred in the electrochemical reaction, indicating the valency of the reaction.
- $F$ : Faraday's constant ( $96\,485.3321\, \text{C mol}^{-1}$ ), representing the charge of one mole of electrons.
- $R$ : Universal gas constant ( $8.3145\,\text{J mol}^{-1}\,\text{K}^{-1}$ ), linking the amount of energy per mole per degree to the equation.
- $T$ : Temperature (K), an essential factor as reaction kinetics are heavily temperature-dependent.

The Butler-Volmer equation is instrumental in modeling electrochemical corrosion, offering insights into how electrochemical kinetics interplay with environmental factors to influence corrosion processes. One of the primary applications of this equation is in predicting corrosion rates. By calculating the current density for both anodic and cathodic reactions at various overpotentials, engineers can estimate the corrosion rate of metals under specific environmental conditions.

Furthermore, the Butler-Volmer equation underpins the design of corrosion protection strategies, such as cathodic protection. By adjusting the overpotential through external anodes or impressed current systems, both the anodic and cathodic reactions can be modulated to control the corrosion process effectively. This precise adjustment of electrochemical parameters, guided by the kinetics described by the Butler-Volmer equation, is crucial for optimizing corrosion protection measures.

In the realm of materials engineering, the equation assists in selecting materials and designing coatings that exhibit favorable kinetic properties to mitigate corrosion. For example, coatings designed to increase the cathodic transfer coefficient can enhance the dominance of cathodic reactions, thereby offering superior protection against metal dissolution. Additionally, the Butler-Volmer equation is vital in assessing the impact of environmental variations—such as changes in pH, temperature, and ionic concentration—on corrosion kinetics. This capability is particularly valuable in industries like marine engineering, where materials are frequently exposed to harsh environmental conditions.

The development of corrosion inhibitors also relies heavily on the insights provided by the Butler-Volmer equation. By modifying the kinetics of anodic or cathodic reactions, corrosion inhibitors are formulated to impede the electrochemical processes that facilitate corrosion. This approach is foundational in creating chemical compounds that effectively reduce corrosion rates.

Moreover, the Butler-Volmer equation is extensively utilized in both academic and industrial research for simulating complex corrosion scenarios. These simulations, which integrate the equation to predict long-term material degradation, support the development of new alloys and protective coatings that are more resistant to corrosion.

Through these diverse applications, the Butler-Volmer equation serves as a cornerstone in the quantitative analysis of corrosion processes, bridging theoretical electrochemistry with practical applications in materials science and engineering. Its widespread use underscores the significance of electrochemical kinetics in designing durable materials and effective strategies for corrosion prevention.

Understanding corrosion in molten salt systems, often used as coolants in nuclear reactors or for energy storage, requires a robust analysis of electrochemical kinetics at high temperatures. The Butler-Volmer equation plays a critical role in this context by providing insights into the electrochemical dynamics that drive corrosion processes under these extreme conditions.

High-temperature operation significantly affects the kinetic parameters such as exchange current density ( $i_0$ ) and transfer coefficients ( $\alpha_a$  and  $\alpha_c$ ), which are integral to the Butler-Volmer equation. These parameters are crucial for determining the current density and, therefore, the corrosion rate. This equation enables the prediction of the overpotential necessary to initiate significant corrosion, which is particularly useful given the unique electrical conductivity and ionic nature of molten salts.

Moreover, the application of the Butler-Volmer equation extends to the evaluation of material stability within molten salt environments. This analysis is vital for selecting appropriate materials for use in systems like molten salt reactors and thermal energy storage, where material longevity and resistance to corrosion are of paramount importance. Through predictive modeling, researchers can assess how different materials will behave and degrade over time when exposed to aggressive molten salts.

The predictive capabilities of the Butler-Volmer equation also facilitate the simulation and modeling

of corrosion in these systems under varied operational conditions. Such advanced simulations help in understanding the intricate interactions between chemical reactions and material degradation. Insights gained from these models are crucial for enhancing the design and operational protocols of molten salt technologies.

In addition to predicting and understanding corrosion, the Butler-Volmer equation is instrumental in the development of corrosion inhibitors tailored for high-temperature applications. By comprehending the kinetics of corrosion processes, chemists are able to devise inhibitors that effectively mitigate these reactions, thus extending the operational life of the materials involved.

For industries that depend on molten salt technologies—such as nuclear and solar thermal energy—the ability to predict and control corrosion is essential for optimizing efficiency, safety, and durability. The Butler-Volmer equation, by providing a detailed view of electrochemical kinetics, underpins efforts to develop more durable materials and innovative corrosion protection strategies, enhancing the overall robustness and sustainability of high-temperature systems.

### 3.3. Tafel Equations for High Overpotentials

The Tafel equations are particularly useful for describing the behavior of electrochemical systems under high overpotentials, where one reaction direction (anodic or cathodic) dominates [22]. These equations simplify the Butler-Volmer model by focusing only on the dominant term:

$$\text{Anodic Tafel Equation: } \eta = \frac{RT}{\alpha_a nF} \ln \left( \frac{i}{i_0} \right)$$
$$\text{Cathodic Tafel Equation: } \eta = -\frac{RT}{\alpha_c nF} \ln \left( \frac{i}{i_0} \right)$$

where:

- $\eta$  is the overpotential,
- $RT/\alpha_a nF$  and  $RT/\alpha_c nF$  are the Tafel slopes for anodic and cathodic processes, respectively,
- $i$  is the current density,
- $i_0$  is the exchange current density,
- $\alpha_a$  and  $\alpha_c$  are the anodic and cathodic transfer coefficients,
- $n$  is the number of electrons transferred per molecule of reactant,
- $F$  is the Faraday constant,
- $R$  is the universal gas constant,
- $T$  is the temperature.

These equations are essential for understanding the exponential increase in current with increasing overpotential, providing insights crucial for the design and optimization of electrodes in batteries and electrolytic cells. In practical applications, the Tafel slopes offer a direct measure of the reaction kinetics' sensitivity to changes in the driving voltage, informing the design of control strategies for electrochemical processes [23].

### 3.4. Tafel Plots in Corrosion Engineering

Tafel plots are a fundamental tool in corrosion engineering, providing a clear visual representation of electrochemical processes at electrode surfaces. By graphing the logarithm of current density against electrode potential, they are instrumental in analyzing the kinetics of corrosion reactions and designing prevention strategies [24].

Derived from the Tafel equation, which describes the exponential increase in current density with overpotential, Tafel plots typically display two linear regions representing the anodic dissolution and cathodic reduction reactions. The intersection of these lines approximates the corrosion potential ( $E_{corr}$ ), offering valuable insights into material behavior.

In corrosion engineering, Tafel plots are used to determine critical parameters such as the corrosion current density ( $i_{corr}$ ) and the corrosion potential. These parameters are essential for evaluating material performance and designing cathodic protection systems. By analyzing Tafel slopes and corrosion currents, engineers can assess material susceptibility to corrosion and formulate effective inhibitors.

In high-temperature environments like molten salt reactors (MSRs), where traditional corrosion monitoring techniques may be less effective, Tafel plots are particularly useful. They provide insights into the electrochemical stability of materials exposed to aggressive molten salts, aiding in the prediction of long-term durability of reactor components.

To utilize Tafel plots for corrosion analysis, potentiodynamic polarization studies are conducted. The electrode potential is swept at a controlled rate, and the resulting current is measured. From these measurements, the Tafel plot is constructed by plotting the logarithm of the absolute current density against the electrode potential. The methodological steps include:

1. **Extrapolation of Linear Regions:** Determining the corrosion potential ( $E_{corr}$ ) by extrapolating the anodic and cathodic branches to their intersection.
2. **Calculation of Corrosion Current Density:** Identifying the corresponding current density at the intersection point as the corrosion current density ( $i_{corr}$ ).
3. **Analysis of Corrosion Rate:** Calculating the material loss or penetration rate from  $i_{corr}$ , often expressed in millimeters per year ( $\text{mm yr}^{-1}$ ).

Interpreting Tafel plots involves examining the slopes of the anodic and cathodic branches, which indicate the controlling electrochemical mechanisms. Steeper slopes suggest activation-controlled processes, while gentler slopes may indicate diffusion-controlled processes. This analysis helps in understanding the rate-determining steps in corrosion reactions and tailoring specific strategies for corrosion control.

While Tafel plots are invaluable in corrosion analysis, their interpretation requires careful consideration of experimental conditions such as electrolyte composition, temperature, and hydrodynamics. Deviations from ideal behavior, often seen at very high or low overpotentials, necessitate more sophisticated models, such as the Butler-Volmer system developed in this work.

In brief, Tafel plots play a critical role in the quantitative analysis of corrosion processes, providing a robust framework for assessing material durability and designing protective measures in various industrial applications. However, the usage of Tafel plots presents some limitations for MSRs. Due to the large amount of species in this reactor, formed not only as a product of corrosion, but also due to the depletion of the liquid nuclear fuel, the amount of currents that need to be measured to develop Tafel plots for each of the potential species can be extremely large. Hence, in this work we develop an independent electrode model

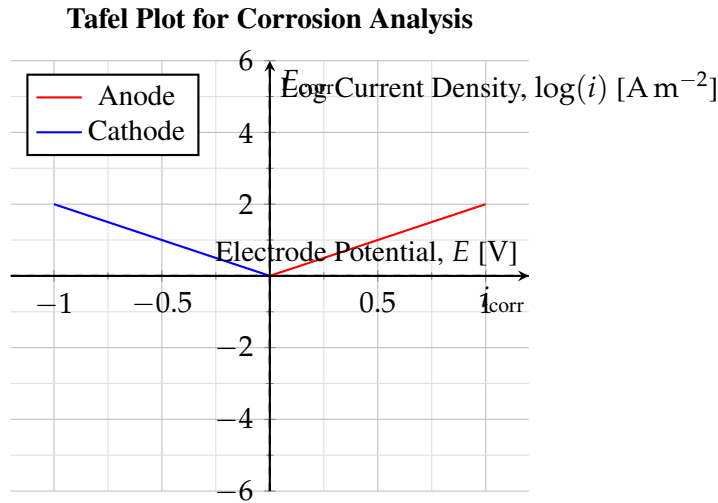


Figure 3. Tafel plot illustrating the anodic and cathodic branches used to determine the corrosion potential and current density.

that extends the Butler-Volmer formulation for a generically large number of species. Although this model does not replace the corrosion engineering based on Tafel analysis, it can help define which electrode potentials need to be primarily measured as they have the largest impact in the corrosion dynamics.

### 3.5. Thermodynamically and Asymptotically Consistent Model for the Butler-Volmer Equation

The Butler-Volmer equation is traditionally employed to model the kinetics of electrochemical reactions by considering the overpotential and the exchange current density. To enhance its accuracy, particularly under conditions with significant concentration gradients, it is beneficial to integrate the concentrations of the reacting species directly into the expression. This approach aligns the equation with the Nernst equation, providing a comprehensive depiction of electrochemical dynamics.

The modified Butler-Volmer equation incorporating these concentration effects is given by:

$$i = i_0 \left[ c_{\text{Ox}} \exp \left( \frac{\alpha_a nF(\eta - \phi)}{RT} \right) - c_{\text{Red}} \exp \left( -\frac{\alpha_c nF(\eta - \phi)}{RT} \right) \right] \quad (12)$$

where:  $c_{\text{Ox}}$  and  $c_{\text{Red}}$  are the concentrations of the oxidized and reduced species, respectively.  $\phi$  is the background potential, reflecting the steady-state potential of the electrode under open circuit conditions.

This modification to the overpotential  $\eta$  now reflects the deviation from a background potential  $\phi$ , adjusting the electrochemical reaction's driving force based on actual electrode conditions.

#### 3.5.1. Derivation of the Nernst Equation

The Nernst equation can be derived as a limiting case of the modified Butler-Volmer equation where the net current  $i$  approaches zero, indicating equilibrium conditions ( $\eta = 0$ ). Setting the current in the modified

Butler-Volmer equation to zero and solving for  $\eta$  yields:

$$0 = i_0 \left[ c_{\text{Ox}} \exp \left( \frac{\alpha_a nF(0 - \phi)}{RT} \right) - c_{\text{Red}} \exp \left( -\frac{\alpha_c nF(0 - \phi)}{RT} \right) \right] \quad (13)$$

Simplifying and solving for  $\phi$ , the equilibrium potential, we obtain the Nernst equation:

$$\phi = E^\circ + \frac{RT}{nF} \ln \frac{c_{\text{Red}}}{c_{\text{Ox}}} \quad (14)$$

### 3.5.2. Derivation of the Tafel Equations

The Tafel equations are derived from the Butler-Volmer equation under the condition of high overpotentials ( $|\eta|$  large). For large positive overpotentials ( $\eta \gg 0$ ), the anodic process dominates:

$$i \approx i_0 c_{\text{Ox}} \exp \left( \frac{\alpha_a nF(\eta - \phi)}{RT} \right) \quad (15)$$

Taking the logarithm of both sides and solving for  $\eta$  yields the Anodic Tafel Equation:

$$\eta \approx \phi + \frac{RT}{\alpha_a nF} \ln \left( \frac{i}{i_0 c_{\text{Ox}}} \right) \quad (16)$$

Similarly, for large negative overpotentials ( $\eta \ll 0$ ), the cathodic process dominates, leading to the Cathodic Tafel Equation:

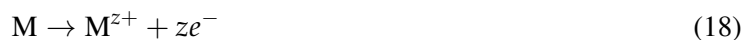
$$\eta \approx \phi - \frac{RT}{\alpha_c nF} \ln \left( \frac{i}{i_0 c_{\text{Red}}} \right) \quad (17)$$

These enhancements to the Butler-Volmer equation not only improve its descriptive accuracy but also provide a more robust framework for predicting electrochemical behavior under a variety of operational conditions.

### 3.5.3. Modeling Species Leaching

Species leaching is a process in which structural materials, such as metals and alloys, dissolve into the molten salt environment. This phenomenon can lead to material degradation and failure in high-temperature applications. Modeling species leaching involves understanding the transport mechanisms and electrochemical reactions at the interface between the structural material and the molten salt.

The leaching process begins with the oxidation of metal atoms from the structural material:



where:

- M represents the metal atom in the solid structure,
- $\text{M}^{z+}$  is the metal ion with valence  $z$ ,
- $e^-$  is the electron.

This oxidation reaction releases metal ions into the molten salt and is driven by the electrochemical potential difference between the metal and the molten salt.

Once formed, the metal ions ( $M^{z+}$ ) are transported away from the interface into the bulk molten salt. This transport is governed by:

1. **Diffusion:** Due to concentration gradients,
2. **Migration:** Under the influence of the electric field,
3. **Convection:** If the molten salt is in motion (often negligible in stationary systems).

The flux of metal ions is described by the Nernst-Planck equation:

$$J_{M^{z+}} = -D_{M^{z+}} \nabla c_{M^{z+}} - \frac{D_{M^{z+}} z e}{k_B T} c_{M^{z+}} \nabla \phi \quad (19)$$

where:

- $J_{M^{z+}}$  is the flux of metal ions ( $\text{mol m}^{-2} \text{s}^{-1}$ ),
- $D_{M^{z+}}$  is the diffusion coefficient of the metal ion ( $\text{m}^2 \text{s}^{-1}$ ),
- $c_{M^{z+}}$  is the concentration of metal ions ( $\text{mol m}^{-3}$ )
- $k_B$  is Boltzmann's constant ( $1.381 \times 10^{-23} \text{ J K}^{-1}$ ),
- $T$  is the absolute temperature (K), and
- $\phi$  is the electrostatic potential (V).

The time evolution of the metal ion concentration is governed by the continuity equation:

$$\frac{\partial c_{M^{z+}}}{\partial t} = -\nabla \cdot J_{M^{z+}} + R_{M^{z+}} \quad (20)$$

Assuming no bulk reactions involving  $M^{z+}$  in the molten salt, the reaction term  $R_{M^{z+}}$  is zero.

At the metal/molten salt interface, the flux of metal ions is related to the interfacial reaction kinetics. The current density  $i$  associated with the oxidation reaction is given by the anodic component of the Butler-Volmer equation:

$$i = i_0 \exp \left( \frac{\alpha_a n F \eta}{RT} \right) \quad (21)$$

where:

- $i_0$  is the exchange current density ( $\text{A}^2 \text{s}^{-1}$ ),
- $\alpha_a$  is the anodic transfer coefficient,
- $n = z$  is the number of electrons transferred,

- $F$  is Faraday's constant ( $96\,485.3321\,C\,mol^{-1}$ ),
- $R$  is the universal gas constant ( $8.3145\,J\,mol^{-1}\,K^{-1}$ ),
- $\eta$  is the overpotential ( $\phi_{\text{metal}} - \phi_{\text{molten salt}} - E_{\text{eq}}$ ).

The flux of metal ions at the interface is then related to the current density by Faraday's law:

$$\mathbf{J}_{M^{z+}} \cdot \mathbf{n} = -\frac{i}{nF} \quad (22)$$

Here,  $\mathbf{n}$  is the unit normal vector pointing from the metal into the molten salt.

The complete model for species leaching involves solving:

### Nernst-Planck Equation for Metal Ions:

$$\frac{\partial c_{M^{z+}}}{\partial t} = \nabla \cdot \left( D_{M^{z+}} \nabla c_{M^{z+}} + \frac{D_{M^{z+}} z e}{k_B T} c_{M^{z+}} \nabla \phi \right) \quad (23)$$

### Poisson Equation for Electrostatic Potential:

$$-\epsilon \nabla^2 \phi = \sum_i z_i e c_i \quad (24)$$

where the sum is over all ionic species in the molten salt.

### Boundary Conditions:

1. At the metal/molten salt interface:

$$D_{M^{z+}} \nabla c_{M^{z+}} \cdot \mathbf{n} + \frac{D_{M^{z+}} z e}{k_B T} c_{M^{z+}} \nabla \phi \cdot \mathbf{n} = -\frac{i_0}{nF} \exp\left(\frac{\alpha_a n F \eta}{RT}\right) \quad (25)$$

2. At the bulk molten salt boundary (far from the interface):

$$c_{M^{z+}} \rightarrow c_{M^{z+}}^\infty \quad (26)$$

3. Initial condition:

$$c_{M^{z+}}(\mathbf{r}, 0) = c_{M^{z+}}^0 \quad (27)$$

These equations are solved numerically using the finite volume method in MOOSE.

Several factors influence the leaching rate in electrochemical systems. Firstly, material properties play a significant role; the composition and microstructure of the metal affect the exchange current density  $i_0$  and the anodic transfer coefficient  $\alpha_a$ . Variations in alloy composition can alter the electrochemical behavior, impacting the rate at which metal ions are released into the molten salt. Microstructural features such as grain size, phase distribution, and the presence of defects can also influence the leaching process by affecting the surface area and the sites available for oxidation reactions.

Secondly, temperature is a critical factor. Higher temperatures increase diffusion coefficients and reaction rates, thereby accelerating the leaching process. Elevated temperatures enhance the kinetic energy of particles, promoting faster diffusion of metal ions into the molten salt and increasing the rate of the oxidation reaction at the metal surface. This temperature dependence is often described by the Arrhenius equation, which relates reaction rates to temperature.

Thirdly, the electrochemical potential, particularly the overpotential  $\eta$ , drives the oxidation reaction. The overpotential represents the deviation from the equilibrium potential and provides the thermodynamic driving force for the dissolution of metal atoms into ions. A higher overpotential increases the reaction rate, leading to more rapid leaching. Control of the electrochemical potential is essential in managing corrosion rates in industrial applications.

Lastly, the composition of the molten salt influences the leaching rate. Impurities and additives can affect the molten salt's conductivity and reactivity. For instance, the presence of aggressive species or oxidizing agents can enhance the corrosion rate by facilitating the oxidation of metal atoms. Conversely, certain additives may inhibit corrosion by forming protective layers or altering the electrochemical properties of the salt. The ionic strength and specific ions present can also influence the activity coefficients of the species involved, thereby affecting the thermodynamics and kinetics of the leaching process.

### 3.5.4. Modeling Species Plating

Species plating refers to the deposition of metal ions from the molten salt onto the structural material. This process can lead to the formation of unwanted deposits, altering the surface properties and potentially causing issues such as blockage or short-circuiting in electrochemical systems.

The plating process involves the reduction of metal ions at the interface:



This reduction reaction results in the deposition of metal atoms onto the structural material. Metal ions are transported from the bulk molten salt to the interface via diffusion and migration:

$$J_{M^{z+}} = -D_{M^{z+}} \nabla c_{M^{z+}} - \frac{D_{M^{z+}}ze}{k_B T} c_{M^{z+}} \nabla \phi \quad (29)$$

At the interface, the flux of metal ions is linked to the reduction current density  $i$  via:

$$J_{M^{z+}} \cdot \mathbf{n} = -\frac{i}{nF} \quad (30)$$

The current density  $i$  is given by the cathodic part of the Butler-Volmer equation:

$$i = -i_0 \exp \left( -\frac{\alpha_c nF\eta}{RT} \right) \quad (31)$$

where:

- $\alpha_c$  is the cathodic transfer coefficient.

The complete model for species plating includes:

**Nernst-Planck Equation for Metal Ions:**

$$\frac{\partial c_{M^{z+}}}{\partial t} = \nabla \cdot \left( D_{M^{z+}} \nabla c_{M^{z+}} + \frac{D_{M^{z+}} z e}{k_B T} c_{M^{z+}} \nabla \phi \right) \quad (32)$$

**Poisson Equation for Electrostatic Potential:**

$$-\epsilon \nabla^2 \phi = \sum_i z_i e c_i \quad (33)$$

**Boundary Conditions:**

1. At the metal/molten salt interface:

$$D_{M^{z+}} \nabla c_{M^{z+}} \cdot \mathbf{n} + \frac{D_{M^{z+}} z e}{k_B T} c_{M^{z+}} \nabla \phi \cdot \mathbf{n} = -\frac{i_0}{nF} \exp \left( -\frac{\alpha_c n F \eta}{RT} \right) \quad (34)$$

2. At the bulk molten salt boundary:

$$c_{M^{z+}} \rightarrow c_{M^{z+}}^\infty \quad (35)$$

3. Initial condition:

$$c_{M^{z+}}(\mathbf{r}, 0) = c_{M^{z+}}^0 \quad (36)$$

As for the leaching case, these equations are solved numerically in MOOSE using the finite volume method.

As metal atoms deposit onto the surface, the thickness of the deposited layer increases over time. The growth rate  $v_{\text{dep}}$  of the layer is related to the molar volume  $V_m$  of the metal:

$$v_{\text{dep}} = \frac{i}{nF} V_m \quad (37)$$

Several key factors influence the plating process in electrochemical systems. Firstly, the concentration of metal ions,  $c_{M^{z+}}$ , plays a critical role; higher concentrations enhance the plating rate by increasing the availability of ions at the electrode surface for reduction. This increased ion availability facilitates a greater flux of metal ions towards the surface, promoting a faster deposition rate.

Secondly, the electrochemical potential, particularly the overpotential  $\eta$ , determines the driving force for the reduction reaction. The overpotential, which is the deviation from the equilibrium potential, directly affects the rate at which electrons are transferred during the plating process. A higher overpotential increases the thermodynamic driving force, leading to an accelerated plating rate.

Thirdly, surface properties such as roughness and composition significantly affect nucleation and growth mechanisms during plating. A rougher surface provides more active sites for nucleation, which can lead to a more uniform and adherent deposit. The composition of the substrate can also influence the interaction between the depositing metal and the substrate, affecting the adhesion and morphology of the plated layer.

Lastly, temperature plays a key role by influencing reaction kinetics and diffusion rates. Elevated temperatures typically increase the kinetic energy of the ions, enhancing both the reaction rate of the electrode processes and the diffusion coefficients of the species in the electrolyte. This temperature dependence can lead to faster plating rates and can also affect the morphology of the deposited metal.

The morphology of the deposited metal layer can vary widely, impacting the material's performance and longevity. A uniform layer is often desired, especially in protective coatings, as it provides consistent coverage and enhances corrosion resistance. However, under certain conditions, dendritic growth may occur, characterized by tree-like structures extending from the electrode surface. Dendritic formations can lead to mechanical failures or short circuits, particularly in battery applications where they may penetrate separators between electrodes. Additionally, the formation of porous structures can adversely affect mechanical strength and reduce corrosion resistance due to increased surface area exposure, which facilitates more aggressive interactions with the environment.

Modeling the plating process involves tracking the moving boundary of the growing deposit to accurately predict the evolution of the deposit morphology. Advanced computational techniques such as the level-set method or phase-field modeling are employed to simulate the interface dynamics and morphological changes during plating. These methods allow for a detailed analysis of the factors influencing deposit growth, including the interplay between diffusion, convection, and reaction kinetics. By incorporating these modeling techniques, it is possible to develop strategies to control the morphology of the deposited layer, optimizing it for specific applications and enhancing the overall performance of the electrochemical system. Experimental techniques such as scanning electron microscopy (SEM) and atomic force microscopy (AFM) are used to study deposit morphology, while electrochemical measurements provide data for model validation.

### 3.5.5. Model for the Exchange Current Density

The exchange current density  $i_0$  determines the rate of electrochemical reactions at equilibrium, where forward and reverse reaction rates are equal. It depends on the concentration of reacting species, temperature, and the Gibbs energy of formation of the products and reactants. The model followed for the exchange current density has been taken from the book of fundamental and applications of electrochemical methods [25].

The model adopted for  $i_0$  is:

$$i_0 = A \cdot c_{\text{Ox}}^{\alpha_a} c_{\text{Red}}^{\alpha_c} \quad (38)$$

where:

- $A$  is the pre-exponential factor related to reaction kinetics,
- $c_{\text{Ox}}$  and  $c_{\text{Red}}$  are the concentrations of the oxidized and reduced species,
- $\alpha_a$  and  $\alpha_c$  are the anodic and cathodic transfer coefficients, and we assume  $\alpha_a = 1 - \alpha_c$ .

The pre-exponential factor  $A$  is modeled as:

$$A = \frac{nFk_0}{RT} \quad (39)$$

where:

- $n$  is the number of electrons transferred,
- $F$  is Faraday's constant,

- $k_0$  is the standard rate constant for the reaction,
- $R$  is the universal gas constant,
- $T$  is the absolute temperature.

The standard rate constant  $k_0$  incorporates the effects of activation energy and reaction kinetics at the electrode surface. The model for  $k_0$  is:

$$k_0 = \kappa \cdot \exp\left(-\frac{\Delta G^\ddagger}{RT}\right) \quad (40)$$

where  $\kappa$  is a transmission coefficient representing the probability of successful electron transfer, which is assumed 1 if no experimental data is available. In the absence of an activation energy database for the molten salt, the Gibbs free energy of activation  $\Delta G^\ddagger$  can be approximated by relating it to the formation energies of the oxidized and reduced species as follows:

$$\Delta G^\ddagger = \frac{(1 - \alpha_a)\Delta G_f^{\text{Ox}} + \alpha_c\Delta G_f^{\text{Red}}}{2} \quad (41)$$

where:

- $\Delta G_f^{\text{Ox}}$  is the Gibbs free energy of formation of the oxidized species,
- $\Delta G_f^{\text{Red}}$  is the Gibbs free energy of formation of the reduced species.

This model ensures that  $i_0$  accounts for the species concentrations, the reaction kinetics, and the thermodynamic driving force through the formation energies and activation energy.

### 3.6. Verification Cases

In this section, we present several verification cases for the implementation of the Butler-Volmer equations within the Poisson-Nernst-Planck framework. The aim of these cases is to validate the numerical implementation against analytical solutions derived from the Nernst equation under various conditions. The verification cases are designed to test the model's ability to predict equilibrium concentrations and electrode potentials accurately for different electrochemical systems and configurations.

The following verification cases are presented:

1. Case 1: Verification case for a single Ni electrode in a neutral electrolyte with constant electrode potential.
2. Case 2: Similar case as Case 1 but with varying electrode potential due to temperature changes.
3. Case 3: Verification case for a double Ni–Zn electrode system, with varying electrode potentials with temperature.
4. Case 4: Grid convergence study for a double Ni–Zn electrode at fixed temperature, coupled to the evolution of the electric potential due to species migration.

For all cases, the parameters used in the calculations are outlined in Table 1.

Table 1. Constants used in the verification cases.

Parameter	Unit	Value
$F$	C mol <sup>-1</sup>	96 485.3321
$R$	J mol <sup>-1</sup> K <sup>-1</sup>	8.314 462 618
$T_{\text{ref}}$	K	300.00
$\alpha$		0.5
$E_{\text{Ni}/\text{Ni}^{2+}}$	V	-0.23
$dE_{\text{Ni}/\text{Ni}^{2+}}/dT$	V K <sup>-1</sup>	$1.46 \times 10^{-4}$
$E_{\text{Zn}/\text{Zn}^{2+}}$	V	-0.76
$dE_{\text{Zn}/\text{Zn}^{2+}}/dT$	V K <sup>-1</sup>	$1.19 \times 10^{-4}$

The verification cases presented are essential for validating the numerical implementation of the Butler-Volmer equations within the Poisson-Nernst-Planck framework. By comparing the numerical results with analytical solutions from the Nernst equation under various conditions, we ensure that the model accurately captures the electrochemical behavior of the systems studied.

Case 1 and Case 2 validate the model for a single electrode system with constant and temperature-dependent electrode potentials, respectively. Case 3 extends the validation to a more complex system involving two different electrode reactions and highlights the model's ability to handle multiple species and reactions simultaneously. Case 4 assesses the numerical accuracy and convergence of the model when coupling the electrochemical kinetics with the electric potential evolution, which is crucial for simulating realistic electrochemical systems where electric fields influence species migration. This case ensures that mesh-independent solutions can be obtained with the current formulation.

These verification studies build confidence in the model's predictive capabilities and lay the foundation for more complex simulations of electrochemical systems.

### 3.6.1. Verification Case 1: Single Nickel Electrode

The first verification case involves a nickel (Ni) electrode in a neutral electrolyte. The objective is to validate the numerical implementation by comparing the computed equilibrium concentration of Ni ions in the electrolyte with the analytical solution obtained from the Nernst equation.

In this case, the initial condition consists of all the nickel present in the solid electrode, with no Ni ions initially in the electrolyte. A transient simulation is performed until equilibrium is reached between the Ni concentration in the solid electrode and in the electrolyte.

The Nernst equation for the half-cell reaction  $\text{Ni} \longleftrightarrow \text{Ni}^{2+} + 2 e^-$  is given by:

$$E = E^\circ + \frac{RT}{nF} \ln \left( \frac{a_{\text{Ni}^{2+}}}{a_{\text{Ni}}} \right), \quad (42)$$

where  $E$  is the electrode potential,  $E^\circ$  is the standard electrode potential,  $R$  is the gas constant,  $T$  is the temperature,  $n$  is the number of electrons transferred,  $F$  is the Faraday constant, and  $a_{\text{Ni}^{2+}}$  and  $a_{\text{Ni}}$  are the activities of  $\text{Ni}^{2+}$  ions and Ni atoms, respectively.

Assuming ideal behavior (activities equal to concentrations), and rearranging the equation to solve for the

concentration ratio  $C_l/C_s$  (liquid over solid concentration), we obtain:

$$\frac{C_l}{C_s} = \exp\left(\frac{nF}{RT}(E - E^\circ)\right). \quad (43)$$

The computed equilibrium concentrations from the numerical simulation are compared with the analytical values from the Nernst equation in Table 2. An excellent agreement is observed between the analytical and numerical results, with errors within numerical precision.

Table 2. Comparison of Nernst and computed values for liquid over solid Ni concentration ratios ( $C_l/C_s$ ) at different temperatures with constant electrode potential.

Temperature [K]	Electrode Potential [V]	$C_l/C_s$		Error [%]
		Nernst	Computed	
300.0	0.23	$5.341 \times 10^7$	$5.34 \times 10^7$	$-8.97 \times 10^{-5}$
400.0	0.23	$6.248 \times 10^5$	$6.25 \times 10^5$	$-3.16 \times 10^{-5}$
500.0	0.23	$4.331 \times 10^4$	$4.33 \times 10^3$	$-5.64 \times 10^{-6}$
600.0	0.23	$7.309 \times 10^3$	$7.31 \times 10^3$	$-5.99 \times 10^{-6}$
700.0	0.23	$2.050 \times 10^3$	$2.05 \times 10^3$	$7.26 \times 10^{-6}$
800.0	0.23	$7.904 \times 10^2$	$7.90 \times 10^2$	$5.74 \times 10^{-6}$

As shown in Table 2, the computed concentration ratios closely match the analytical values obtained from the Nernst equation across the range of temperatures studied. The percent error remains below 0.001%, demonstrating the accuracy of the numerical implementation for this single-electrode system with constant electrode potential.

### 3.6.2. Verification Case 2: Single Ni Electrode with Varying Electrode Potential due to Temperature

In the second verification case, we consider the effect of temperature on the electrode potential for the same Ni electrode system. The electrode potential varies with temperature according to the relation:

$$E_{\text{Ni}/\text{Ni}^{2+}}(T) = E_{\text{Ni}/\text{Ni}^{2+}}^\circ + \left(\frac{dE_{\text{Ni}/\text{Ni}^{2+}}}{dT}\right)(T - T_{\text{ref}}), \quad (44)$$

where  $E_{\text{Ni}/\text{Ni}^{2+}}^\circ$  is the standard electrode potential at the reference temperature  $T_{\text{ref}}$ , and  $\frac{dE_{\text{Ni}/\text{Ni}^{2+}}}{dT}$  is the temperature coefficient of the electrode potential.

As in Case 1, we perform transient simulations at various temperatures until equilibrium is reached, and compare the computed concentration ratios with the analytical values from the Nernst equation, accounting for the temperature-dependent electrode potential. The results are presented in Table 3.

Table 3. Comparison of Nernst and computed values for  $C_l / C_s$  at different temperatures with varying electrode potential.

Temperature [K]	Electrode Potential [V]	$C_l / C_s$		Error [%]
		Nernst	Computed	
300.0	0.230	$5.341 \times 10^7$	$5.34 \times 10^7$	$-8.97 \times 10^{-5}$
400.0	0.215	$2.678 \times 10^5$	$2.68 \times 10^5$	$-1.02 \times 10^{-5}$
500.0	0.201	$1.117 \times 10^4$	$1.12 \times 10^4$	$-2.27 \times 10^{-5}$
600.0	0.186	$1.343 \times 10^3$	$1.34 \times 10^3$	$5.98 \times 10^{-7}$
700.0	0.172	$2.958 \times 10^2$	$2.96 \times 10^{22}$	$-7.46 \times 10^{-6}$
800.0	0.157	$9.509 \times 10^1$	$9.51 \times 10^1$	$-2.98 \times 10^{-6}$

The results in Table 3 show excellent agreement between the computed and analytical concentration ratios, with errors remaining negligible across the temperature range. This verifies that the numerical model accurately captures the temperature dependence of the electrode potential and its effect on the equilibrium concentrations.

### 3.6.3. Verification Case 3: Double Ni-Zn Electrode with Varying Electrode Potentials due to Temperature

The third verification case involves a galvanic cell composed of two electrodes: a Ni electrode and a Zn electrode, immersed in a shared electrolyte. The objective is to verify the model's ability to handle multiple electrode reactions and the associated equilibrium concentrations under varying temperatures.

In this system, both electrode potentials vary with temperature, and the overall cell potential is determined by the difference between the Zn and Ni electrode potentials:

$$E_{\text{cell}}(T) = E_{\text{Zn/Zn}^{2+}}(T) - E_{\text{Ni/Ni}^{2+}}(T), \quad (45)$$

where each electrode potential is calculated using Equation 44 for the respective metal.

At equilibrium, the concentration ratios for Zn and Ni ions can be computed using the Nernst equation for each half-cell reaction. The numerical simulations involve transient calculations until the concentrations reach equilibrium. The computed results are compared with the analytical values in Table 4.

Table 4. Reaction potentials and concentration ratios for Ni and Zn at different temperatures.

T [K]	E [V]		$E_{\text{cell}}$ [V]	Ni <sub>l</sub> /Ni <sub>s</sub>		Zn <sub>l</sub> /Zn <sub>s</sub>		Error [%]	
	Ni	Zn		Nernst	Computed	Nernst	Computed	Ni	Zn
300.0	0.230	0.760	0.5300	$1.55878 \times 10^{-18}$	$2.11 \times 10^{-16}$	$6.41529 \times 10^{17}$	$6.42 \times 10^{17}$	$-1.35 \times 10^4$	$5.76 \times 10^{-6}$
400.0	0.215	0.748	0.5327	$3.77182 \times 10^{-14}$	$3.79 \times 10^{-14}$	$2.65124 \times 10^{13}$	$2.65 \times 10^{13}$	-0.582	$-3.19 \times 10^{-6}$
500.0	0.201	0.736	0.5354	$1.60995 \times 10^{-11}$	$1.61 \times 10^{-11}$	$6.21139 \times 10^{10}$	$6.21 \times 10^{10}$	$-2.55 \times 10^{-3}$	$4.78 \times 10^{-6}$
600.0	0.186	0.724	0.5381	$9.12679 \times 10^{-10}$	$9.13 \times 10^{-10}$	$1.09568 \times 10^9$	$1.10 \times 10^9$	$-4.47 \times 10^{-5}$	$-2.90 \times 10^{-6}$
700.0	0.172	0.712	0.5408	$1.63239 \times 10^{-8}$	$1.63 \times 10^{-8}$	$6.12600 \times 10^7$	$6.13 \times 10^7$	$-2.86 \times 10^{-5}$	$-3.06 \times 10^{-6}$
800.0	0.157	0.701	0.5435	$1.41972 \times 10^{-7}$	$1.42 \times 10^{-7}$	$7.04366 \times 10^6$	$7.04 \times 10^6$	$-1.94 \times 10^{-5}$	$-5.34 \times 10^{-6}$

Table 4 presents the electrode potentials for Ni and Zn at various temperatures, along with the corresponding cell potential and concentration ratios computed using the Nernst equation and numerical simulations.

The computed concentration ratios for Zn show excellent agreement with the analytical values, with errors on the order of  $10^{-6}\%$ .

For Ni, at lower temperatures (300 K), a significant discrepancy is observed between the computed and analytical concentration ratios, indicated by a large percent error. This is because these small values are capped by the numerical precision of the MOOSE solvers. This discrepancy diminishes rapidly with increasing temperature, and by 500 K, the error reduces to negligible levels when the concentration of Nickel in the electrolyte decreases.

The observed discrepancy at lower temperatures for Ni can be attributed to numerical limitations when dealing with extremely small concentration ratios, approaching machine precision limits. As the temperature increases, the concentration ratios become larger and more accurately captured by the numerical model.

This verification case demonstrates the model's capability to handle multiple electrode reactions and accurately predict the equilibrium concentrations in a galvanic cell system, accounting for temperature-dependent electrode potentials.

### **3.6.4. Verification Case 4: Grid Convergence Study for the Butler-Volmer Equation Coupled with the Poisson Equation for Electric Potential**

In the fourth verification case, we perform a grid convergence study to assess the numerical accuracy and convergence behavior of the model when coupling the Butler-Volmer equation with the Poisson equation for electric potential. This case involves the double Ni–Zn electrode system at a fixed temperature, with species migration contributing to the evolution of the electric potential in the system.

The grid convergence study involves running simulations with progressively refined mesh sizes and calculating the Grid Convergence Index (GCI) to quantify the numerical error and convergence rate. The GCI is calculated using the method proposed by Roache [26], which provides an estimate of the discretization error.

The mesh sizes used and the corresponding concentration ratios for Zn and Ni are presented in Table 5. The GCIs are calculated between successive mesh refinements.

Table 5. Mesh size refinement study with Grid Convergence Index (GCI) for  $Zn_l/Zn_s$  and  $Ni_l/Ni_s$ .

Mesh Size [m]	$Zn_l$	$Ni_l$	GCI	
	$Zn_s$	$Ni_s$	$Zn_l/Zn_s$	$Ni_l/Ni_s$
0.05	$9.87 \times 10^{-11}$	$2.27 \times 10^{-14}$		
0.0125	$1.07 \times 10^{-10}$	$6.10 \times 10^{-14}$		
0.003125	$1.26 \times 10^{-10}$	$6.20 \times 10^{-14}$	$9.71 \times 10^{-3}$	$1.09 \times 10^{-3}$
0.00078125	$1.26 \times 10^{-10}$	$6.20 \times 10^{-14}$	$1.11 \times 10^{-6}$	$1.12 \times 10^{-5}$
0.000195313	$1.26 \times 10^{-10}$	$6.20 \times 10^{-14}$	$5.30 \times 10^{-8}$	$9.78 \times 10^{-7}$
$4.88281 \times 10^{-5}$	$1.26 \times 10^{-10}$	$6.20 \times 10^{-14}$	$5.30 \times 10^{-9}$	$2.27 \times 10^{-6}$

As shown in Table 5, the concentration ratios for Zn and Ni converge to stable values as the mesh is refined. The GCIs decrease with mesh refinement, indicating that the numerical solution is approaching the grid-independent solution.

The small values of the GCIs at the finest mesh levels suggest that the numerical errors due to spatial discretization are minimal. This confirms the numerical implementation's robustness and accuracy when

coupling the electrochemical reactions with the electric potential evolution due to species migration.

### 3.7. Full Poisson-Nernst-Planck Model

In this section, we present the comprehensive implementation of the Poisson-Nernst-Planck (PNP) model to simulate the transport of ionic species in both solid and liquid phases, coupled with energy conservation and fluid flow in the liquid phase that has been implemented in MOOSE [11]. The model incorporates electrochemical reactions at the solid-liquid interface through the Butler-Volmer equation, enabling the analysis of corrosion processes in high-temperature molten salt environments.

The PNP model describes the transport of charged species under the influence of concentration gradients and electric fields. The model is extended to include thermal effects and fluid flow in the liquid phase.

#### 3.7.1. Species Transport Equations

In the liquid phase, the transport of ionic species in the liquid electrolyte is governed by the Nernst-Planck equation:

$$\frac{\partial c_i}{\partial t} + \nabla \cdot \mathbf{N}_i = R_i, \quad (46)$$

where  $c_i$  is the concentration of species  $i$ ,  $\mathbf{N}_i$  is the flux of species  $i$ , and  $R_i$  is the reaction rate of species  $i$  in the liquid phase. The flux  $\mathbf{N}_i$  includes diffusion, migration due to the electric field, and convection:

$$\mathbf{N}_i = -D_i \nabla c_i - \frac{D_i z_i e}{k_B T} c_i \nabla \phi + c_i \mathbf{v}, \quad (47)$$

where  $D_i$  is the diffusion coefficient,  $z_i$  is the charge number,  $e$  is the elementary charge,  $k_B$  is Boltzmann's constant,  $T$  is the temperature,  $\phi$  is the electric potential, and  $\mathbf{v}$  is the velocity field of the liquid.

In the solid phase, for species in the solid electrode, transport is primarily by diffusion:

$$\frac{\partial c_i^s}{\partial t} = \nabla \cdot (D_i^s \nabla c_i^s) + R_i^s, \quad (48)$$

where  $c_i^s$  and  $D_i^s$  are the concentration and diffusion coefficient of species  $i$  in the solid phase, respectively, and  $R_i^s$  is the reaction rate in the solid.

#### 3.7.2. Electric Potential Equation

The electric potential  $\phi$  is determined by the Poisson equation:

$$-\nabla \cdot (\epsilon \nabla \phi) = \rho, \quad (49)$$

where  $\epsilon$  is the permittivity of the medium and  $\rho$  is the charge density given by:

$$\rho = \sum_i F e c_i, \quad (50)$$

where  $F$  is the Faraday constant.

### 3.7.3. Energy Conservation Equation

The temperature field affects reaction kinetics and transport properties. Energy conservation is solved simultaneously in the electrolyte and electrode and reads as follows:

$$\rho c_p \left( \frac{\partial T}{\partial t} + \mathbf{v} \cdot \nabla T \right) = \nabla \cdot (k \nabla T) + Q_{\text{reaction}}, \quad (51)$$

where  $\rho$  is the density,  $c_p$  is the specific heat capacity,  $k$  is the thermal conductivity, and  $Q_{\text{reaction}}$  is the heat generated by chemical reactions.

### 3.7.4. Fluid Flow Equations in the Liquid Phase

The flow of the liquid electrolyte is described by the incompressible Navier-Stokes equations:

$$\nabla \cdot \mathbf{v} = 0. \quad (52)$$

$$\rho \left( \frac{\partial \mathbf{v}}{\partial t} + (\mathbf{v} \cdot \nabla) \mathbf{v} \right) = -\nabla p + \mu \nabla^2 \mathbf{v} + \mathbf{F}_{\text{body}}, \quad (53)$$

where  $p$  is the pressure,  $\mu$  is the dynamic viscosity, and  $\mathbf{F}_{\text{body}}$  includes body forces such as electric forces:

$$\mathbf{F}_{\text{body}} = \rho_e \mathbf{E}, \quad (54)$$

with  $\rho_e$  being the local charge density and  $\mathbf{E} = -\nabla \phi$  the electric field.

### 3.7.5. Boundary Conditions at the Solid-Liquid Interface

At the interface between the solid electrode and the liquid electrolyte, electrochemical reactions occur, governed by the Butler-Volmer equations previously described. The flux of species at the interface is related to the interfacial current density for the ionic species in the liquid:

$$\mathbf{N}_i \cdot \mathbf{n} = -\frac{i}{n_i F}, \quad (55)$$

where  $n_i$  is the stoichiometric coefficient of species  $i$  in the reaction, and  $\mathbf{n}$  is the unit normal vector pointing from the solid to the liquid. For the solid phase, the interface conditions read as follows:

$$-D_i^s \nabla c_i^s \cdot \mathbf{n} = \frac{i}{n_i F}. \quad (56)$$

At the interface, the electric potential is continuous:

$$\phi_s = \phi_l. \quad (57)$$

The model involves strong coupling between species transport, electric potential, temperature, and fluid flow.

The equations are solved using a nonlinear Jacobian method, which is automatically computed using the automatic differentiation. This is important since performing Picard iterations was leading to spurious solutions when solving this system.

### 3.8. Verification of the Poisson-Nernst-Planck Model

The verification of the Poisson-Nernst-Planck (PNP) model is needed to ensure the accuracy and reliability of the numerical implementation used to simulate coupled species transport and electric potential in electrochemical systems. To achieve this, a *method of manufactured solutions* (MMS) was employed. MMS is a systematic approach where an exact analytical solution is assumed, and the corresponding source terms are derived such that the governing equations are satisfied by this solution. This method provides a rigorous framework to assess the convergence and correctness of the numerical methods used in the implementation.

In this verification problem, source terms are introduced on the right-hand side of the governing equations to enforce a predefined solution. Specifically, we consider a coupled system involving two ionic species concentrations,  $c_0(x, y)$  and  $c_1(x, y)$ , and an electric potential  $\phi(x, y)$ . The manufactured solutions for these variables are defined as:

$$c_0(x, y) = \tau + \frac{\tau}{2} \cos(\pi x) \cos(\pi y), \quad (58)$$

$$c_1(x, y) = \tau - \frac{\tau}{2} \cos(\pi x) \cos(\pi y), \quad (59)$$

$$\phi(x, y) = -\frac{\tau F}{2\epsilon} [(1-x)x + (1-y)y], \quad (60)$$

where  $\tau$  is a constant parameter,  $F$  is Faraday's constant, and  $\epsilon$  is the permittivity of the medium. These solutions introduce spatial variations in both the concentrations and the electric potential, providing a challenging test case for the numerical solver.

By substituting these manufactured solutions into the original governing equations, the required source terms are derived to ensure that the equations are satisfied exactly. The governing equations for species transport and electric potential, modified to include these source terms, are:

$$\frac{\partial c_i}{\partial t} = D_i \nabla^2 c_i + \frac{z_i e}{k_B T} \nabla \cdot (D_i c_i \nabla \phi) + S_{c_i}, \quad i = 0, 1, \quad (61)$$

$$-\nabla \cdot (\epsilon \nabla \phi) = \sum_{i=0}^1 z_i F c_i + S_\phi, \quad (62)$$

where  $D_i$  is the diffusion coefficient of species  $i$ ,  $z_i$  is the charge number,  $e$  is the elementary charge,  $k_B$  is Boltzmann's constant,  $T$  is the temperature, and  $S_{c_i}$  and  $S_\phi$  are the source terms resulting from the MMS.

Figure 4 illustrates the manufactured solution fields for  $c_0(x, y)$ ,  $c_1(x, y)$ , and  $\phi(x, y)$  with  $\tau = 1$  and  $\epsilon = 1$ . The concentration fields exhibit a cosine spatial variation, while the electric potential shows a quadratic dependence on the spatial coordinates.

To verify the numerical implementation, the modified governing equations are solved numerically using a second-order finite volume method. The computational domain is progressively refined to assess the convergence of the numerical solution towards the exact manufactured solution. Since a second-order discretization scheme is employed, it is expected that the numerical errors will decrease quadratically with mesh refinement if the implementation is correct.

The convergence results are presented in Figure 5, where the  $L_2$  norm of the error between the numerical and analytical solutions is plotted against the mesh size, denoted by  $\|\Delta x, \Delta y\|$ . As observed in the figure, the error decreases approximately proportionally to the square of the mesh size, confirming second-order convergence. This result validates that the numerical methods for the coupled PNP system are correctly implemented and that the solver accurately captures the behavior of the model under mesh refinement.

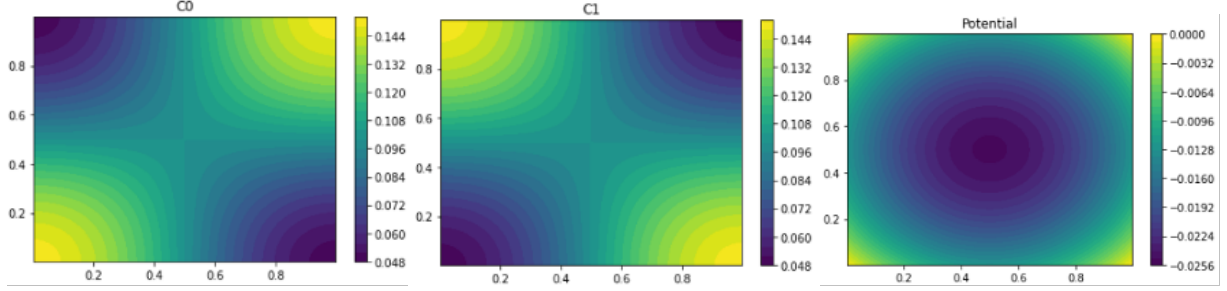


Figure 4. Manufactured solution fields with  $\tau = 1$  and  $\varepsilon = 1$ : (a) concentration field  $c_0(x, y)$ , (b) concentration field  $c_1(x, y)$ , (c) electric potential  $\phi(x, y)$ .

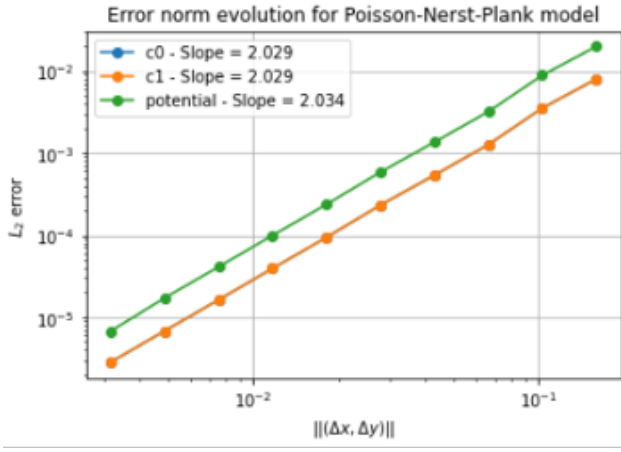


Figure 5. Convergence study for the PNP model implementation. The plot shows the  $L_2$  norm of the error versus mesh size  $\|\Delta x, \Delta y\|$ , indicating second-order convergence.

The successful application of the method of manufactured solutions demonstrates that the numerical solver accurately reproduces the prescribed analytical solutions, achieving the expected second-order convergence rate. This indicates that the coupled species transport and electric potential equations are correctly formulated and discretized in the numerical implementation. Such thorough verification provides confidence in the PNP model's capability to simulate coupled electrochemical phenomena, including ion transport and electric field distribution, which are essential for understanding and predicting corrosion processes in various environments.

By confirming the correctness of the numerical implementation, a solid foundation is established for applying the PNP model to more complex and realistic electrochemical systems. The verified model can be used to simulate the behavior of ionic species and electric potentials under various conditions, contributing valuable insights into the mechanisms of corrosion and aiding in the development of effective mitigation strategies.

In conclusion, the verification process confirms that the numerical implementation of the PNP model is accurate and reliable. The model successfully captures the coupled dynamics of species transport and electric potential, and the numerical methods used are capable of achieving the expected convergence rates. This ensures that the PNP model is a robust tool for simulating electrochemical systems and can be confidently employed in further research and applications related to corrosion modeling.

## 4. COUPLED LIQUID-GAS SPECIES TRANSPORT IN MOLTEN SALT REACTORS

Two-phase flow in molten salt loops is a critical phenomenon in advanced nuclear reactors and thermal energy storage systems. The transport of corrosion products and their interactions within these systems can significantly impact material degradation, system efficiency, and safety. Corrosion products may exist in both liquid and gaseous phases, and understanding their behavior requires accurate modeling of two-phase species transport.

Two-phase species tracking involves modeling the flow of liquid molten salt and gas bubbles, along with the transport of dissolved and gaseous species between these phases. The mixture model, combined with interface area tracking, provides an effective framework for simulating such complex flows.

This section presents the governing equations for two-phase flow using the mixture model with interface area tracking and describes the species transport between the liquid and gas phases in a molten salt loop.

### 4.1. Two-Phase Flow Modeling Using the Mixture Model

The mixture model treats the two-phase flow as a single continuum by averaging the properties of the liquid and gas phases. This approach simplifies the mathematical formulation while capturing essential characteristics of the flow.

#### 4.1.1. Governing Equations

The conservation equations for mass, momentum, and energy of the mixture are as follows [27]:

- **Continuity Equation:**

$$\frac{\partial \rho}{\partial t} + \nabla \cdot (\rho \mathbf{v}) = 0 \quad (63)$$

- **Momentum Equation:**

$$\frac{\partial(\rho \mathbf{v})}{\partial t} + \nabla \cdot (\rho \mathbf{v} \otimes \mathbf{v}) = -\nabla p + \nabla \cdot [\mu_{\text{mix}} (\nabla \mathbf{v} + \nabla \mathbf{v}^T)] + \rho \mathbf{g} + \mathbf{F}_{\text{drift}} \quad (64)$$

- **Energy Equation:** For systems where energy effects are significant, the energy equation can be included. However, for isothermal flows, it may be omitted.

#### 4.1.2. Definition of Mixture Variables

The mixture variables are defined based on the phase volume fractions and properties:

- **Mixture Density:**

$$\rho = \alpha_l \rho_l + \alpha_g \rho_g \quad (65)$$

where:

- $\alpha_l$  and  $\alpha_g$  are the volume fractions of the liquid and gas phases, respectively, with  $\alpha_l + \alpha_g = 1$ .
- $\rho_l$  and  $\rho_g$  are the densities of the liquid and gas phases.

- **Mass-Averaged Velocity:**

$$\rho \mathbf{v} = \alpha_l \rho_l \mathbf{v}_l + \alpha_g \rho_g \mathbf{v}_g \quad (66)$$

Therefore, the mixture velocity  $\mathbf{v}$  is:

$$\mathbf{v} = \frac{\alpha_l \rho_l \mathbf{v}_l + \alpha_g \rho_g \mathbf{v}_g}{\rho} \quad (67)$$

where  $\mathbf{v}_l$  and  $\mathbf{v}_g$  are the velocities of the liquid and gas phases.

- **Mixture Viscosity:**

$$\mu_{\text{mix}} = \alpha_l \mu_l + \alpha_g \mu_g \quad (68)$$

where  $\mu_l$  and  $\mu_g$  are the dynamic viscosities of the liquid and gas phases.

#### 4.1.3. Interfacial Momentum Transfer

The term  $\mathbf{F}_{\text{drift}}$  represents the momentum transfer due to the relative motion (slip) between the phases. It can be modeled using:

$$\mathbf{F}_{\text{drift}} = -\nabla \cdot (\alpha_g \rho_g \mathbf{v}_d \mathbf{v}_d) \quad (69)$$

where  $\mathbf{v}_d$  is the drift velocity, defined as:

$$\mathbf{v}_d = \mathbf{v}_g - \mathbf{v}_l \quad (70)$$

#### 4.1.4. Interface Area Tracking

The interfacial area concentration  $a_i$  represents the interfacial area per unit volume between the liquid and gas phases. It is important for modeling mass, momentum, and energy transfer across the interface. The transport equation for the interfacial area concentration is:

$$\frac{\partial a_i}{\partial t} + \nabla \cdot (a_i \mathbf{v}) = S_{a_i} \quad (71)$$

where  $S_{a_i}$  includes source and sink terms due to bubble coalescence, breakup, and phase change.

#### 4.1.5. Closure Relations

To complete the mixture model, closure relations are required for:

- **Slip Velocity ( $\mathbf{v}_d$ ):** An expression or correlation to compute the relative velocity between phases. For small bubbles in laminar flow, the slip velocity can be approximated using Stokes' law.
- **Interfacial Area Source Term ( $S_{a_i}$ ):** Models for bubble dynamics, including nucleation, growth, coalescence, and breakup.
- **Interfacial Forces:** In addition to drag, other interfacial forces such as lift, virtual mass, and turbulent dispersion may be included.

#### 4.1.6. Numerical Solution

The mixture model equations are discretized using appropriate numerical methods (e.g., finite volume method) and solved iteratively. The solution procedure typically involves:

1. Updating mixture properties based on current estimates of volume fractions.
2. Solving the continuity and momentum equations to obtain the mixture velocity  $\mathbf{v}$  and pressure  $p$ .
3. Calculating slip velocity  $\mathbf{v}_d$  and updating phase velocities  $\mathbf{v}_l$  and  $\mathbf{v}_g$ .
4. Solving the interfacial area concentration equation to update  $a_i$ .
5. Ensuring mass conservation and updating volume fractions  $\alpha_l$  and  $\alpha_g$ .

## 4.2. Species Transport Between Liquid and Gas Phases

Corrosion products and other chemical species may be transported between the liquid and gas phases through mass transfer at the interface.

#### 4.2.1. Governing Equations for Species Transport

The conservation equations for species  $k$  in each phase are:

##### Liquid Phase Species Transport

$$\frac{\partial(\alpha_l \rho_l Y_{l,k})}{\partial t} + \nabla \cdot (\alpha_l \rho_l \mathbf{v}_l Y_{l,k}) = -\nabla \cdot (\alpha_l \mathbf{J}_{l,k}) + \Gamma_k^{lg} \quad (72)$$

##### Gas Phase Species Transport

$$\frac{\partial(\alpha_g \rho_g Y_{g,k})}{\partial t} + \nabla \cdot (\alpha_g \rho_g \mathbf{v}_g Y_{g,k}) = -\nabla \cdot (\alpha_g \mathbf{J}_{g,k}) - \Gamma_k^{lg} \quad (73)$$

where:

- $Y_{l,k}$  and  $Y_{g,k}$  are the mass fractions of species  $k$  in the liquid and gas phases.
- $\mathbf{J}_{l,k}$  and  $\mathbf{J}_{g,k}$  are the diffusive fluxes of species  $k$  in the liquid and gas phases.
- $\Gamma_k^{lg}$  is the interphase mass transfer rate of species  $k$  from the liquid to the gas phase per unit volume.

#### 4.2.2. Interphase Mass Transfer

The interphase mass transfer rate  $\Gamma_k^{lg}$  can be modeled using mass transfer coefficients:

$$\Gamma_k^{lg} = a_i K_k (C_{l,k} - C_{l,k}^*) \quad (74)$$

where:

- $K_k$  is the overall mass transfer coefficient for species  $k$ .
- $C_{l,k}$  is the concentration of species  $k$  in the liquid phase.
- $C_{l,k}^*$  is the equilibrium concentration of species  $k$  in the liquid phase in equilibrium with the gas phase.
- $a_i$  is the interfacial area concentration.

Three different models are proposed for the mass transfer coefficient:

1. On the one hand, the mass transfer coefficient can be defined via the Sherwood number correlation [28] as follows  $\text{Sh} = 0.0096\text{Re}^{0.913}\text{Sc}^{0.346}$ , where  $\text{Re}$  is the Reynolds number based on the characteristic length of the geometry, e.g., the diameter of the pipe, and  $\text{Sc}$  is the Schmidt number. Once computed, the Sherwood number is used to compute the mass transfer coefficient as  $K_k = \text{Sh}D_{l,k}/L$ , where  $D_{l,k}$  is the diffusion coefficient for component  $k$  in the liquid phase and  $L$  is the characteristic length of the geometry. This model is used in MOOSE for computing the coupled corrosion mass transfer studies in a simple two-phase demonstration loop with natural convection.
2. Additionally, the mass transfer equivalent of the Dittus-Boelter correlation can be used for modeling mass transfer of insoluble material out of the flow to gas-liquid interfacial areas[29]. Similarly, the Sherwood number is defined as  $\text{Sh} = 0.023\text{Re}^{0.8}\text{Sc}^{0.4}$ . This correlation is used when coupling MOOSE with Thermochemical to model gas-liquid contactors like the toroidal spray ring in the Molten Salt Reactor Experiment model discussed in a later section.
3. Lastly, for interphase mass transfer involving species transport to bubbles with a mobile interface, the following Sherwood number is selected where  $\text{Sh} = 0.62\text{Re}^{0.45}\text{Sc}^{0.5}(L/d_b)^{0.5}$  [30]. Here  $d_b$  is the average bubble diameter of the bubble swarm that make up the void fraction in the molten salt. This correlation is used when coupling MOOSE with Thermochemical to model the volatilization of chemically reacting fission products like iodine and cesium to the noble gas phase of a helium bubble swarm as showcased in the Molten Salt Reactor Experiment model in a later section.

Lastly, when utilizing Thermochemical within MOOSE to assist in calculating the interphase mass transfer, the driving force of volatilization (i.e.,  $(C_{l,k} - C_{l,k}^*)$ ) can be directly informed by the calculation of phase equilibria of chemical species in the thermochemical system. Here Thermochemical calculates the phase equilibria  $C_{g,k}^*$  and  $C_{l,k}^*$  at thermochemical equilibrium of chemical species in both a molten salt and ideal gas phase.

Coupling Thermochemical with MOOSE in this way comes with the assumption that the chemical reaction kinetics in the molten salt system are infinitely fast and that mass transfer is the rate limiting step. This is an inherent approximation since Thermochemical can only calculate thermochemical equilibrium which is a point calculation that can be used as an effective source term for indicating the strength and direction of chemical speciation or solvation between phases that are not yet in equilibrium as modeled by the two-phase flow species transport equations. Performing multiphysics modeling in this manner allows for the best engineering scale approximation of the volatilization and subsequent transport of chemical species in MSR systems for source term calculations and off-gas system design which will be demonstrated in later sections.

### 4.2.3. Diffusive Fluxes

The diffusive fluxes are given by Fick's law:

$$\mathbf{J}_{l,k} = -\rho_l D_{l,k} \nabla Y_{l,k} \quad (75)$$

$$\mathbf{J}_{g,k} = -\rho_g D_{g,k} \nabla Y_{g,k} \quad (76)$$

where  $D_{l,k}$  and  $D_{g,k}$  are the diffusion coefficients in the liquid and gas phases.

### 4.2.4. Numerical Solution

The species transport equations are solved alongside the flow equations. The solution involves:

1. Solving the flow field to obtain velocities  $\mathbf{v}_l$ ,  $\mathbf{v}_g$ , and volume fractions  $\alpha_l$ ,  $\alpha_g$ .
2. Computing interfacial area concentration  $a_i$ .
3. Calculating mass transfer rates  $\Gamma_k^{lg}$  based on current species concentrations.
4. Solving the species transport equations to update mass fractions  $Y_{l,k}$  and  $Y_{g,k}$ .
5. Iterating until convergence is achieved for both flow and species concentrations.

Modeling two-phase species tracking in molten salt loops is needed for predicting the behavior of corrosion products and understanding corrosion dynamics. The mixture model with interface area tracking provides a robust framework for simulating two-phase flow, while the species transport equations capture the mass transfer between liquid and gas phases. Accurate modeling of these processes contributes to improved design, operation, and safety of molten salt systems.

## 5. MOLTEN SALT REACTOR MULTI-REGION DEPLETION ANALYSES CAPABILITIES

The evolution of isotopic inventory in MSRs is affected by both the radioactive decay, nuclear transmutation reactions, and the speciation of the fuel salt. This section details the multiphysics depletion-driven thermochemistry capabilities developed using the MOOSE-based applications Griffin and Pronghorn coupled to Gibbs energy minimizer Thermochimica.

### 5.1. Improvements in Bateman multi-region modeling

The nuclide number inventory in a system with transmutations, radioactive decay, and depletion events is mathematically described by the Bateman equations which describe the rate of change of isotopes in the system:

$$\frac{dn_i}{dt} = \sum_{i'} \left( \gamma_{i' \rightarrow i} \sum_g \sigma_{i'}^f \phi_g + \sum_g \sigma_{i' \rightarrow i}^t \phi_g + r_{i' \rightarrow i} \lambda_{i'} \right) n_{i'} - \left( \sum_g \sigma_i^a \phi_g + \lambda_i \right) n_i + S_i^{\text{chem}} + S_i^{\text{stream}}, \quad (77)$$

where

- $n_i$ ,  $n'_i$  are the amounts of nuclides  $i$  and  $i'$  respectively,
- $\sigma_{i'}^f$  is the groupwise fission cross-section of nuclide  $i'$ ,
- $\gamma_{i' \rightarrow i}$  is the yield of nuclide  $i$  from fission of nuclide  $i'$ ,
- $\sigma_{i' \rightarrow i}^t$  is the groupwise transmutation cross-section of nuclide  $i'$  that produces nuclide  $i$ ,
- $\phi_g$  is the groupwise scalar neutron flux,
- $\lambda_i$ ,  $\lambda_{i'}$  are the radioactive decay constants for nuclides  $i$  and  $i'$  respectively,
- $r_{i' \rightarrow i}$  is the branching ratio for nuclide  $i'$  decaying to  $i$ ,
- $\sigma_i^a$  is the groupwise absorption cross-section of nuclide  $i$ , and
- $S_i^{\text{chem}}$  and  $S_i^{\text{stream}}$  are the chemical reaction and mass transfer source terms respectively.

The MOOSE-based reactor physics analysis application Griffin supports multiple solvers for depletion calculations and solving the Bateman equation. These solvers include the Chebyshev Rational Approximation Method (CRAM), the Mini-Max Polynomial Approximation Method (MMPA), and the Adding and Doubling Method (ADM). However, in liquid-fueled reactors such as MSRs, the additional fuel and waste streams moving and in and out of the liquid fuel are key to accurately capturing the reactor physics, which involve species separation in MSRs. Most MSR designs also include an active off-gassing system and/or an off-gas plenum to collect volatile fission products. While fuel and fission product mobility itself complicates the depletion calculations, the phase evolution and speciation also contribute to the complexity. An off-gas isotope removal capability was previously added in Griffin which assumes the removal of isotopes from the fuel salt to an off gas mixture. However, in many applications, there are multiple regions/mixtures between which there is potential for transfer of inventory. As an example, in addition to off gas, one could assume a transfer of certain isotopes to solid precipitates. This requires a generalization of the depletion capability to capture continuous removal of isotopes into an arbitrary number of regions. Each of these regions should be simultaneously depleted. In such a scenario, the above equation can be written with individual composition variables for each region and with the removal constants representing the transfer of a nuclide from one region to another. The modified equation for an arbitrary region is then written as follows:

$$\frac{dn_i^m}{dt} = \sum_{i'} \left( \gamma_{i' \rightarrow i} \sum_g \sigma_{i'}^f \phi_g + \sum_g \sigma_{i' \rightarrow i}^t \phi_g + r_{i' \rightarrow i} \lambda_{i'} \right) n_{i'}^m + \sum_{m'} \lambda_i^{m' \rightarrow m} n_i^{m'} - \left( \sum_g \sigma_i^a \phi_g + \lambda_i \right) n_i^m + S_i^{\text{chem}} + S_i^{\text{stream}}, \quad (78)$$

where the new added transfer term is highlighted in red in the previous equation and

- Superscripts  $m$ ,  $m'$  represent the mixture region and
- $\lambda_i^{m' \rightarrow m} n_i^{m'}$  represents the removal rate of nuclide  $i$  from region  $m'$  to region  $m$ .

The above system can be represented in the matrix form as follows:

$$\begin{pmatrix} d\mathbf{n}^1/dt \\ d\mathbf{n}^2/dt \\ \vdots \\ d\mathbf{n}^M/dt \end{pmatrix} = \begin{pmatrix} \mathbf{A}^1 & \mathbf{A}^{2 \rightarrow 1} & \dots & \mathbf{A}^{M \rightarrow 1} \\ \mathbf{A}^{1 \rightarrow 2} & \mathbf{A}^2 & \dots & \mathbf{A}^{M \rightarrow 2} \\ \vdots & \vdots & \ddots & \vdots \\ \mathbf{A}^{1 \rightarrow M} & \mathbf{A}^{2 \rightarrow M} & \dots & \mathbf{A}^M \end{pmatrix} \begin{pmatrix} \mathbf{n}^1 \\ \mathbf{n}^2 \\ \vdots \\ \mathbf{n}^M \end{pmatrix} + \begin{pmatrix} \mathbf{S}_1^{\text{chem}} \\ \mathbf{S}_2^{\text{chem}} \\ \vdots \\ \mathbf{S}_M^{\text{chem}} \end{pmatrix} + \begin{pmatrix} \mathbf{S}_1^{\text{stream}} \\ \mathbf{S}_2^{\text{stream}} \\ \vdots \\ \mathbf{S}_M^{\text{stream}} \end{pmatrix} \quad (79)$$

However, the size of the above system can quickly grow leading to convergence issues even with the most modern depletion solvers. Therefore, during the development of this capability, a choice was made to support transfer from one principle region (core) to three other regions. Also, it was assumed that there will be no mass transfer between the three non-core regions. The schematic mass transfer scheme is shown in Figure 6

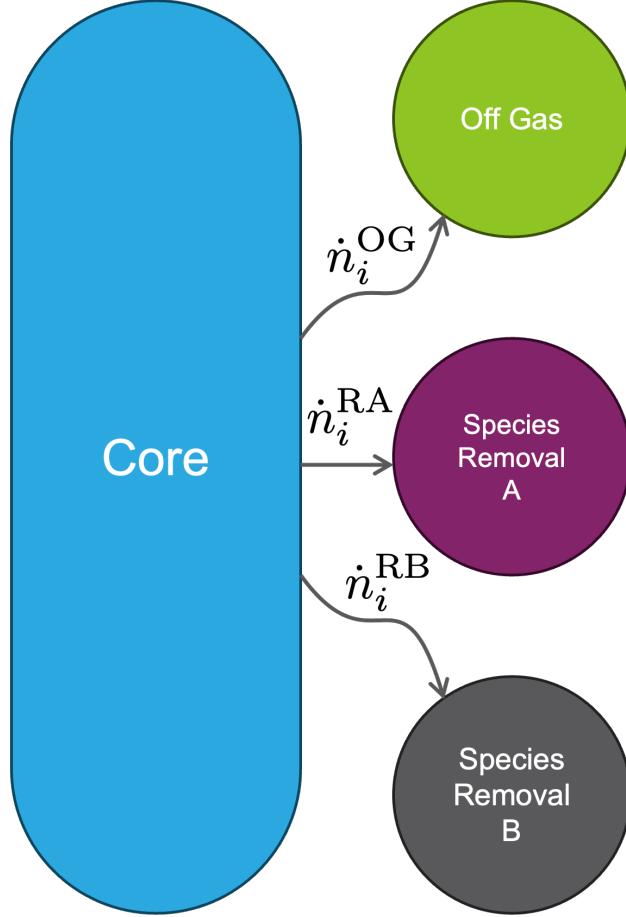


Figure 6. Schematic nuclide transfer diagram for the four-region depletion implementation.

This reduces the above equation to the following form:

$$\begin{pmatrix} \frac{dn^{\text{Core}}}{dt} \\ \frac{dn^{\text{OG}}}{dt} \\ \frac{dn^{\text{RA}}}{dt} \\ \frac{dn^{\text{RB}}}{dt} \end{pmatrix} = \begin{pmatrix} \mathbf{A}^{\text{Core}} & 0 & 0 & 0 \\ \mathbf{A}^{\text{Core} \rightarrow \text{OG}} & \mathbf{A}^{\text{OG}} & 0 & 0 \\ \mathbf{A}^{\text{Core} \rightarrow \text{RA}} & 0 & \mathbf{A}^{\text{RA}} & 0 \\ \mathbf{A}^{\text{Core} \rightarrow \text{RB}} & 0 & 0 & \mathbf{A}^{\text{RB}} \end{pmatrix} \begin{pmatrix} \mathbf{n}^{\text{Core}} \\ \mathbf{n}^{\text{OG}} \\ \mathbf{n}^{\text{RA}} \\ \mathbf{n}^{\text{RB}} \end{pmatrix} + \begin{pmatrix} \mathbf{S}^{\text{Core}}_{\text{chem}} \\ \mathbf{S}^{\text{OG}}_{\text{chem}} \\ \mathbf{S}^{\text{RA}}_{\text{chem}} \\ \mathbf{S}^{\text{RB}}_{\text{chem}} \end{pmatrix} + \begin{pmatrix} \mathbf{S}^{\text{Core}}_{\text{stream}} \\ \mathbf{S}^{\text{OG}}_{\text{stream}} \\ \mathbf{S}^{\text{RA}}_{\text{stream}} \\ \mathbf{S}^{\text{RB}}_{\text{stream}} \end{pmatrix}, \quad (80)$$

which results in a triangular sparse matrix.

A new vector postprocessor `MultiregionBatemanVPP` has been added to Griffin to create the matrices for the above system of equation. The vector postprocessor also solves the system of equation using the CRAM method. Despite the reduced size of the system of equations, the implementation resulted in an approximately  $15\times$  increase in the time required for solving the system of equation as compared to the previous implementation where only off-gassing was considered. This was because the original implementation was relying on matrix inversion which are extremely costly operations that scale cubically with the size of the matrix. Even though depletion each of the regions individually and accounting for mass transfer explicitly

could reduce computational time, it would introduce undesirable limits on the time step that can be used during depletion due to numerical stability concerns. A potential solution would be to use sparse Gaussian elimination, which has been shown to be an efficient method for solving the linear systems associated with the CRAM approximation [31]. This method has been added to Griffin previously but wasn't fully utilized in the BatemanVPP. MultiregionBatemanVPP leverages sparse Gaussian elimination to reduce the computational time needed in CRAM and has provided a speedup of approximately  $8\times$  compared to direct matrix inversion.

## 6. DEMONSTRATION CASES

### 6.1. Validation of the Poisson-Nernst-Planck Model Using Experimental Data

To validate the Poisson-Nernst-Planck (PNP) model for corrosion in molten salt systems, we compare the model predictions with experimental data from a natural convection corrosion loop conducted at Oak Ridge National Laboratory (ORNL) [32]. This experiment provides a dataset for evaluating the accuracy of flow-accelerated corrosion models under realistic operating conditions of FLiNaK molten salt in a stainless steel 316H loop.

Figure 7 illustrates the geometry of the corrosion loop, including the positioning of thermocouples and the placement of corrosion coupons along the loop. The right side of the figure presents light micrographs of the corrosion coupons after the experiment. A 2D model was adopted for these simulation. The validation parameters chosen for the models are the penetration depth of corrosion in the corrosion coupons and the concentrations of chromium (Cr) and iron (Fe) cations remaining in the molten salt at the end of the experiment.

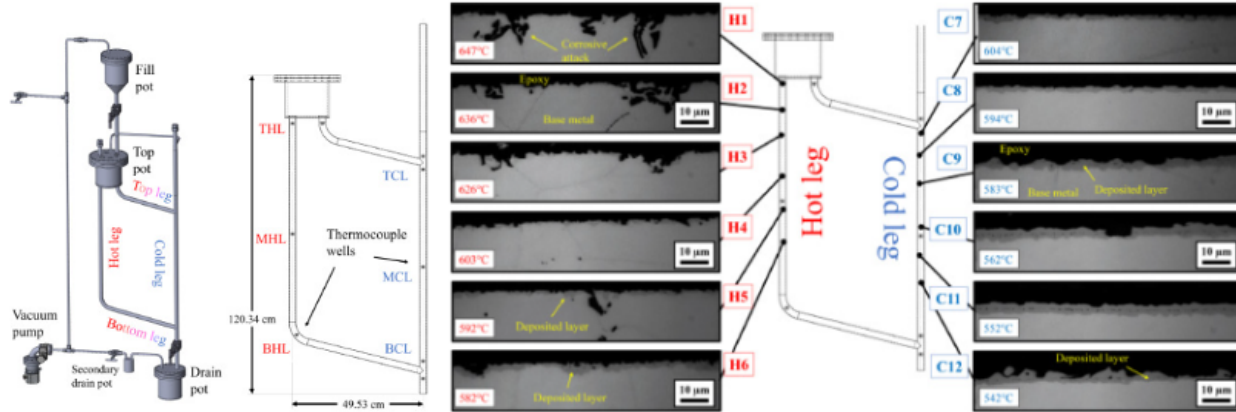


Figure 7. Natural convection corrosion loop experiment for validating flow-accelerated corrosion models [32]. **Left:** Geometry of the loop and location of the thermocouples. **Right:** Position of the corrosion coupons and corresponding light micrographs.

In the experiment, the bottom leg of the loop is heated by a 900 W power heater, while the hot leg is heated by two 900 W heaters. For the cold and bottom legs, a constant wall temperature of 520 °C is maintained using heating tape, which controls the average temperature throughout the experiment.

For the validation, a computational model replicating the main pipe section of the experiment where the corrosion coupons are placed was developed. The model omits the top intermediate pot and the drain pot, as they do not significantly contribute to the flow dynamics or the corrosion processes within the loop. The

mesh employed a cell size target of 2 mm for the pipe interior, approximately one-tenth of the pipe's internal diameter, and 1 mm for the pipe wall, approximately one-sixth of the pipe wall thickness. The complete mesh for the pipe interior and wall consisted of approximately 30,000 cells.

The thermal-hydraulic simulations were initialized with zero velocity and a uniform temperature of 520 °C. The simulation proceeded until the flow field reached a steady state. Figure 8 presents the results obtained for the velocity and temperature fields. The flow rises in the bottom and hot legs due to thermal expansion and buoyancy effects and returns via the top and cold legs, completing the natural convection loop. The temperature increases continuously in the bottom and hot legs due to heating and decreases in the top and cold legs as the fluid cools.

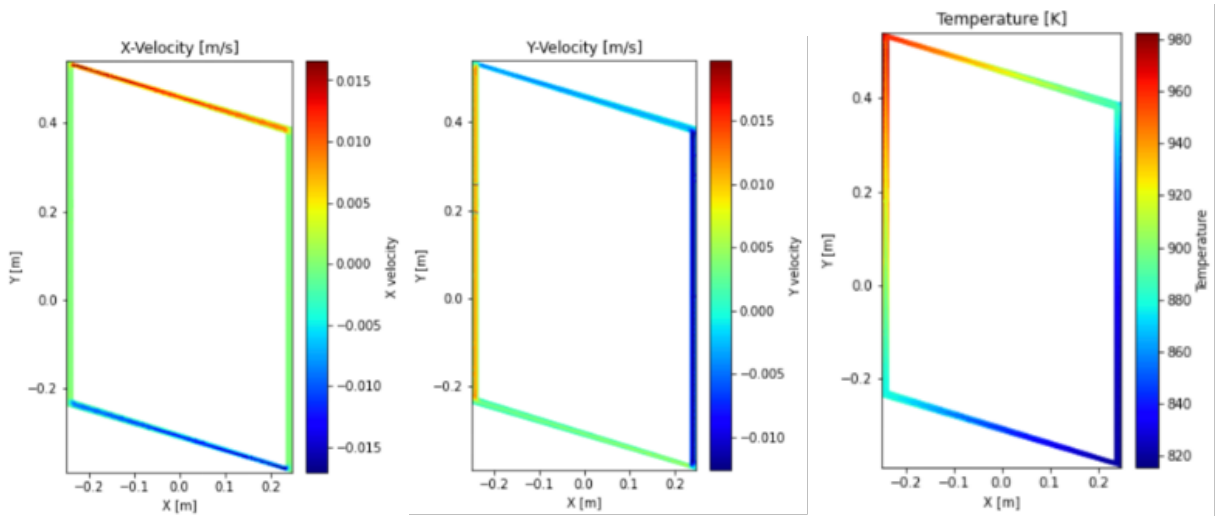


Figure 8. Thermal-hydraulic fields for steady-state operation of the natural convection loop. **Left:** Velocity component in the X-direction. **Center:** Velocity component in the Y-direction. **Right:** Temperature field.

The predicted temperatures at the salt-wall interfaces were compared with the thermocouple readings from the experiment at steady state. Table 6 summarizes the results. A very good agreement is observed between the numerical predictions and the experimental measurements, indicating that the thermal-hydraulic model accurately captures the flow and temperature distribution within the loop. This agreement provides a solid basis for comparing the flow-accelerated corrosion models.

Table 6. Comparison of predicted and measured temperatures in the natural convection loop at steady state.

Position	Exit HL	CL TCL	CL BLC	HL BHL	HL THL
Thermocouple reading [°C]	661	607	520	555	647
Predicted temperature [°C]	663	608	520	556	648

The concentration profiles for chromium and iron at the pipe wall, as well as the predicted corrosion penetration depths at the end of the experiment, were obtained using the PNP model. These results are presented in Figure 9.

The models predict that chromium continuously leaches out of the metal structure, while iron leaches out in hot regions and deposits in cold regions. The predicted corrosion penetration depths show good agreement with the experimental data, as depicted in the figures. The negative penetration depth for iron indicates deposition onto the surface rather than material loss.

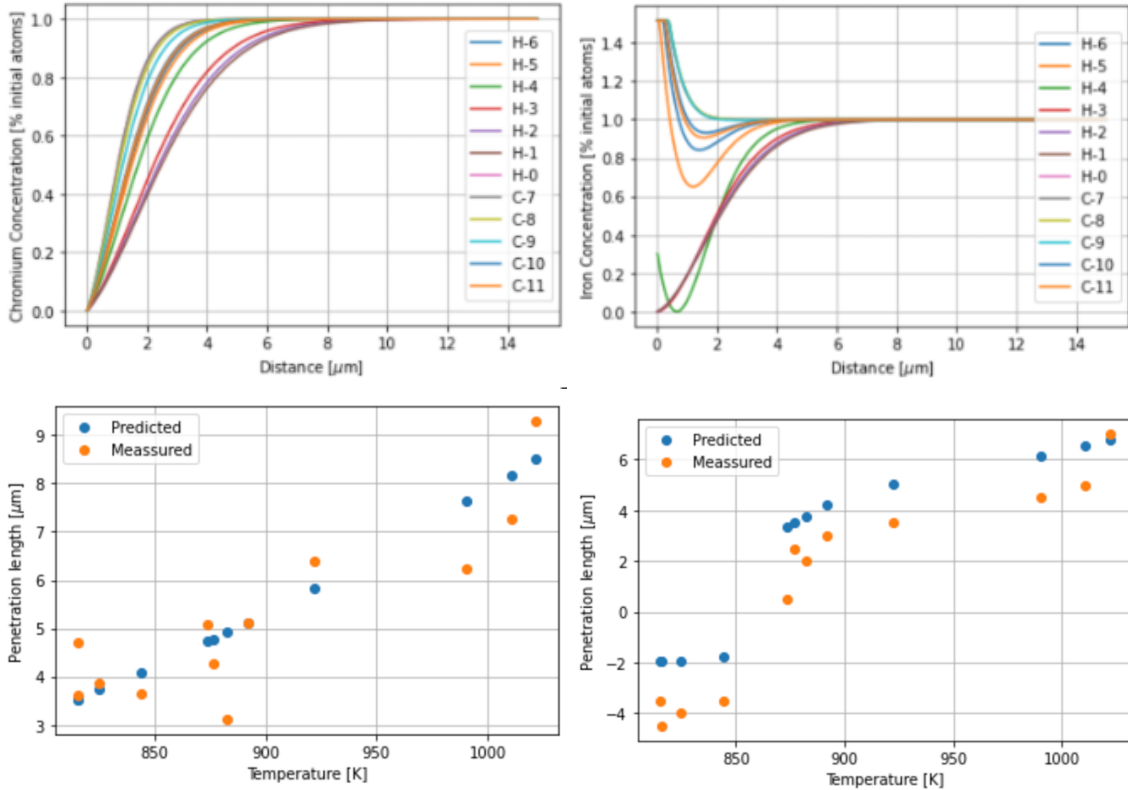


Figure 9. Results for the Poisson-Nernst-Planck (PNP) model. **Top Left:** Predicted chromium concentration profiles. **Top Right:** Predicted iron concentration profiles. **Bottom Left:** Corrosion penetration depth for chromium. **Bottom Right:** Corrosion penetration depth for iron.

Despite the large dispersion observed in the experimental data, primarily due to conglomerates of material detaching from the surface as observed in the micrographs in Figure 7, the model provides reasonable predictions of the corrosion penetration depths. This dispersion is not captured by the models, as the detachment of material is not included in the mass transport or PNP formulations.

The concentrations of chromium and iron in the molten salt after the experiments are further compared in Table 7. Both the mass transport model and the PNP model predictions are within the uncertainty bounds of the experimental measurements. This agreement corroborates the accuracy of the leaching currents predicted by the models.

Table 7. Comparison of predicted and measured concentrations of chromium and iron in the molten salt at the end of the experiment (in weight parts per million [wppm]).

Concentration [wppm]	Chromium (Cr)	Iron (Fe)
Experimental measurement	255±28	68±8
Mass transport model prediction	235	75
PNP model prediction	251	72

In conclusion, the PNP models show good agreement with experimental data regarding corrosion penetration depths and species concentrations in the molten salt.

## 6.2. 2D Molten Salt Loop with Two-Phase Flow

The two-phase flow in molten salt loops is an important factor for understanding the distribution of corrosion products and gas-phase species in high-temperature environments. As corrosion products leach from the structures, they dissolve in the liquid phase. If voids are present in the molten salt loop, the dissolved corrosion products can transfer into the gas phase. This mass exchange process can lead to a reduction in corrosion cations in the salt, which, in turn, reduces the buildup of the electric potential in the salt that hinders the corrosion process. Hence, the presence of two-phase flow in the molten salt loop can result in increased corrosion. This test case demonstrates the model's capability to capture corrosion in a two-phase flow loop.

This section presents the simulation results for a 2D natural convection flow loop under two-phase flow conditions, focusing on the temperature and velocity fields, void fraction, and the transport of corrosion products. Table 8 provides the key parameters used in the simulation of the molten salt loop, while Figure 10 shows the geometry used for the 2D natural convection loop simulation. The dimensions of the loop are shown in meters in Figure 10. The molten salt circulates due to natural convection, driven by heating and cooling zones, while gas bubbles are introduced into the system in the hot section and extracted in the cooling section, affecting the flow and temperature distribution.

Table 8. Problem parameters for the molten salt loop with two-phase flow for the 2D natural convection flow loop demonstration case.

Parameter	Value
Molten Salt	FLiNaK
Pipe	Stainless Steel 316H
Pipe Composition	Fe (71%) - Cr (17%) - Ni (12%)
Heat Source	1 MW
Heat Exchange Coefficient	$0.1 \text{ MW m}^{-3}$
Cold Source Exchange Temperature	900 K
Volumetric Void Injection Source	$0.02 \text{ m}^{-3}$
Void Extraction Coefficient	$1.0 \text{ m}^{-3}$
Operation Time	1,000 h

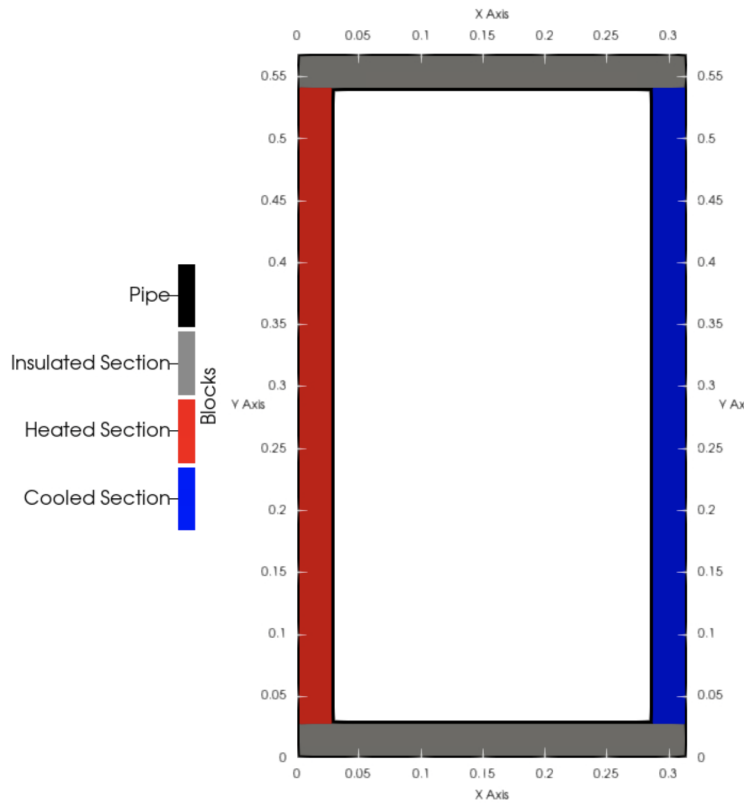


Figure 10. Geometry for the 2D natural convection flow loop demonstration case.

The temperature distribution in the molten salt and the solid pipe at steady state is shown in Figure 11. On the left, the molten salt temperature shows higher values near the heating region. The temperature profile develops downstream as the salt is heated and pumped by the buoyancy introduced by the heating and void injection. The temperature mixes in the top section of the pipe. The temperature of the solid increases while the flow is heated in the left leg and is approximately isothermal over the top leg. As the flow enters the right leg, it is cooled due to the heat exchange with the cold source, causing the temperature to decrease as the flow circulates through the cold leg. The temperature of the pipe in the cold leg also decreases as the flow is cooled. The flow then enters the bottom leg, where it mixes and remains approximately isothermal, as does the pipe in contact with the flow.

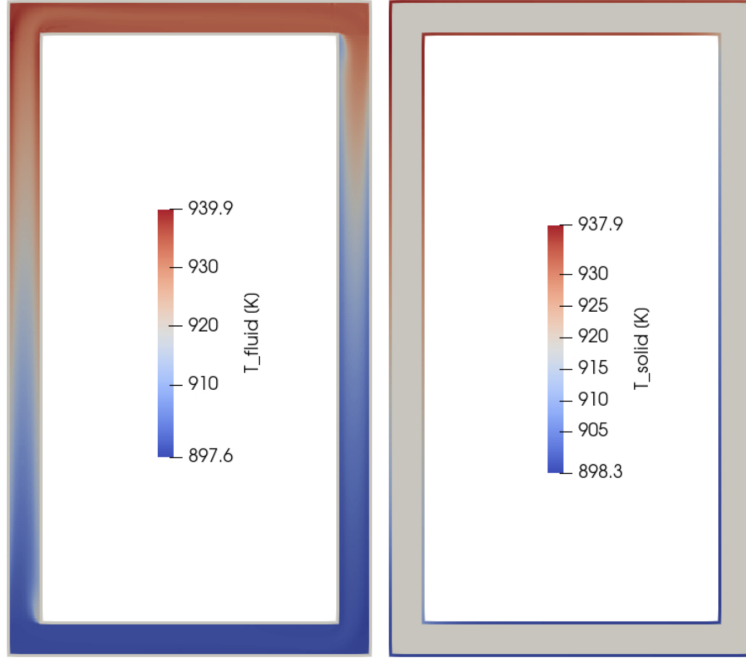


Figure 11. Temperature distribution for the system operating at steady-state for the 2D natural convection flow loop demonstration case. **Left:** temperature in the molten salt. **Right:** temperature in the solid pipe.

The evolution of the void fraction, shown in Figure 12, illustrates the development of the two-phase flow over time. Void is injected in the left hot leg and extracted in the cold leg with the void extraction coefficient of  $1.0 \text{ [-/m}^3]$  mentioned in Table 8. The void fraction rises in the left leg, mixes in the top leg, and then is extracted in the right leg. The evolution of the void fraction is shown through snapshots at different time steps. At  $t = 0 \text{ s}$ , there are no gas bubbles in the system. By  $t = 20 \text{ s}$ , bubbles start to form, and at  $t = 1000 \text{ s}$ , the gas bubbles are well-distributed throughout the loop, with higher void fractions near the heating section where bubbles are generated due to the elevated temperatures. This is the void configuration that is approximately maintained during system operation.

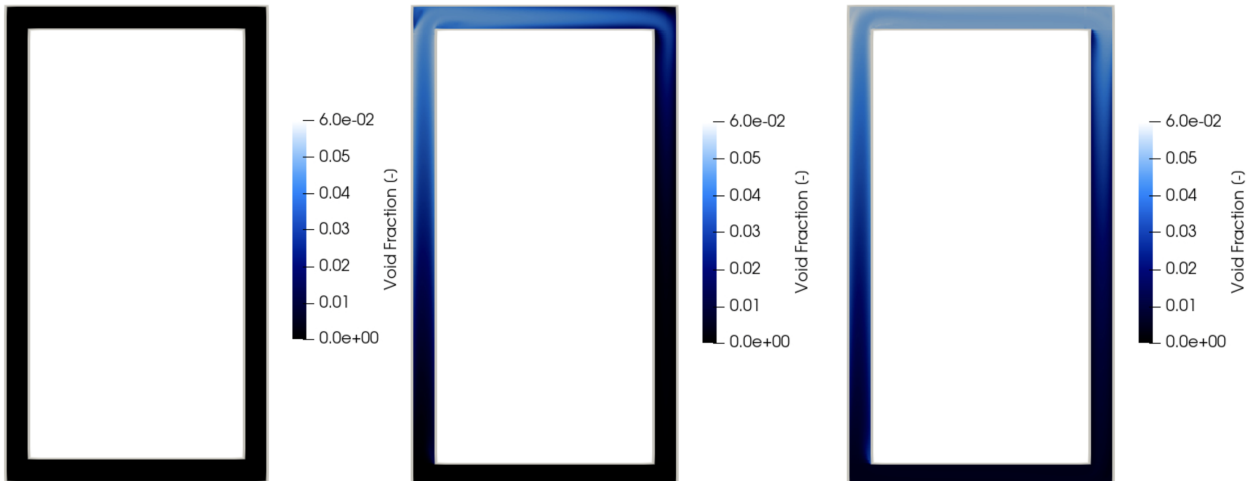


Figure 12. Void fraction in the two-phase natural convection loop demonstration case at different time steps:  $t = 0 \text{ s}$  (left),  $t = 20 \text{ s}$  (center),  $t = 1000 \text{ s}$  (right).

The velocity field at steady state, presented in Figure 13, is mainly a product of the thermal- and void-fraction-driven natural convection. Both heating and void injection in the left leg lead to rising velocities, while cooling and void extraction in the right leg lead to descending velocities. The remaining flow velocities are due to the conservation of mass in the closed loop. As expected, a nearly flat velocity profile is observed in the left and right legs, where the flow is driven by the volumetric forces. In the top and bottom sections, and their downstream regions, friction against the pipe wall plays a more significant role, influencing the velocity profile.

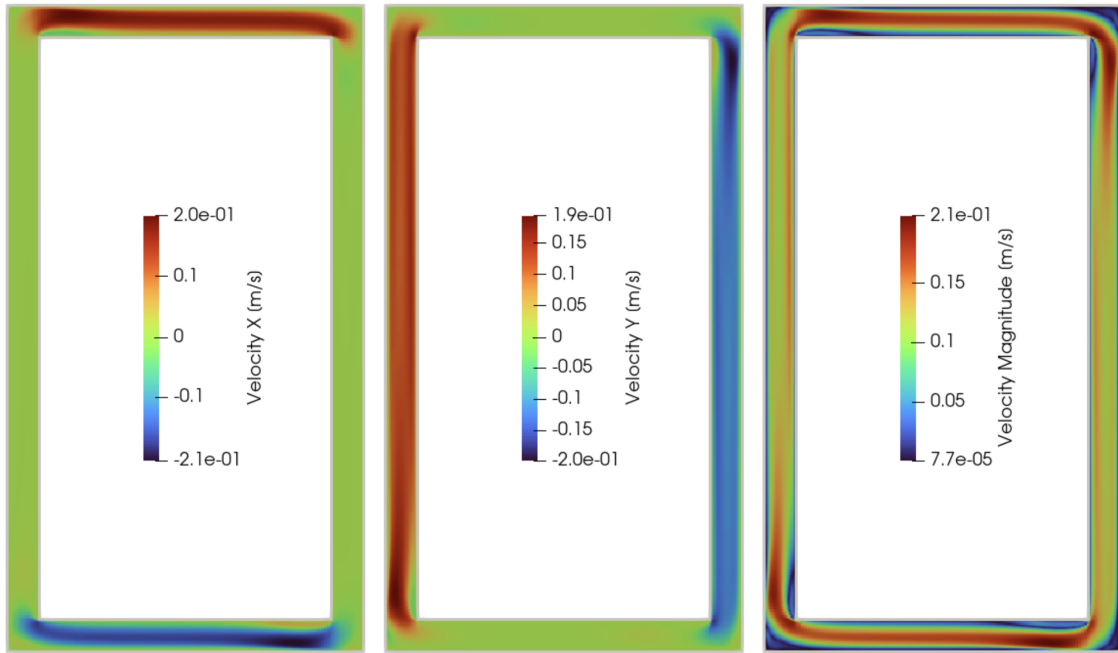


Figure 13. Velocity field for the system operating at steady-state for the 2D natural convection flow loop demonstration case.

Figure 14 shows the interface area concentration, which quantifies the interfacial area between the liquid and gas phases. A higher interface area concentration leads to more efficient mass transfer between the phases, influencing the transport of species and the dissolution of corrosion products into the molten salt and gas phases. The interface area concentration generally follows the void fraction distribution, with an increase near the open side of the elbows due to higher shear strain rates in those regions.

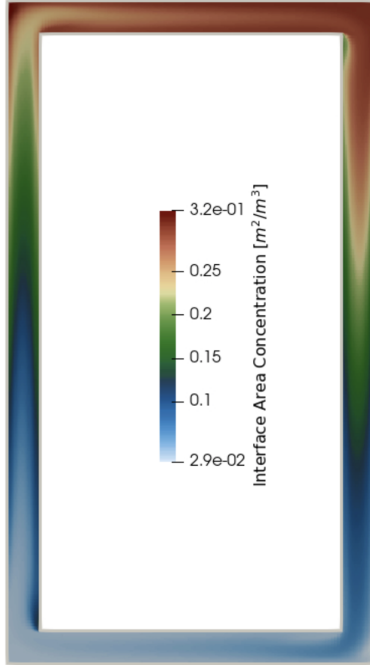


Figure 14. Interface area concentration for the system operating at steady-state for the 2D natural convection flow loop demonstration case.

The distribution of corrosion products, specifically chromium, iron, and nickel, after 1,000 hours of operation is shown in Figures 15, 16, and 17. Different behaviors are observed for these species due to their differing electrode potentials.

For chromium, as shown in Figure 15, leaching occurs throughout the domain. This is evident from the lower concentration of chromium near the molten salt-pipe interface. The chromium concentration decreases in the regions with higher void fractions due to the reduced liquid volume and transfer of chromium into the gas phase.

The iron distribution, shown in Figure 16, is similar to chromium in the liquid phase, following the void fraction distribution. However, iron leaches from the hot left and top legs and plates in the colder right and bottom legs, a mass transfer mechanism similar to the one observed in the validation case from the previous section.

The nickel distribution, shown in Figure 17, is significantly lower than chromium and iron, due to its lower electrode potential, resulting in minimal oxidation currents. Some nickel initially leaches into the molten salt, but as the salt's electric potential rises, the nickel plates back onto the pipe surface.

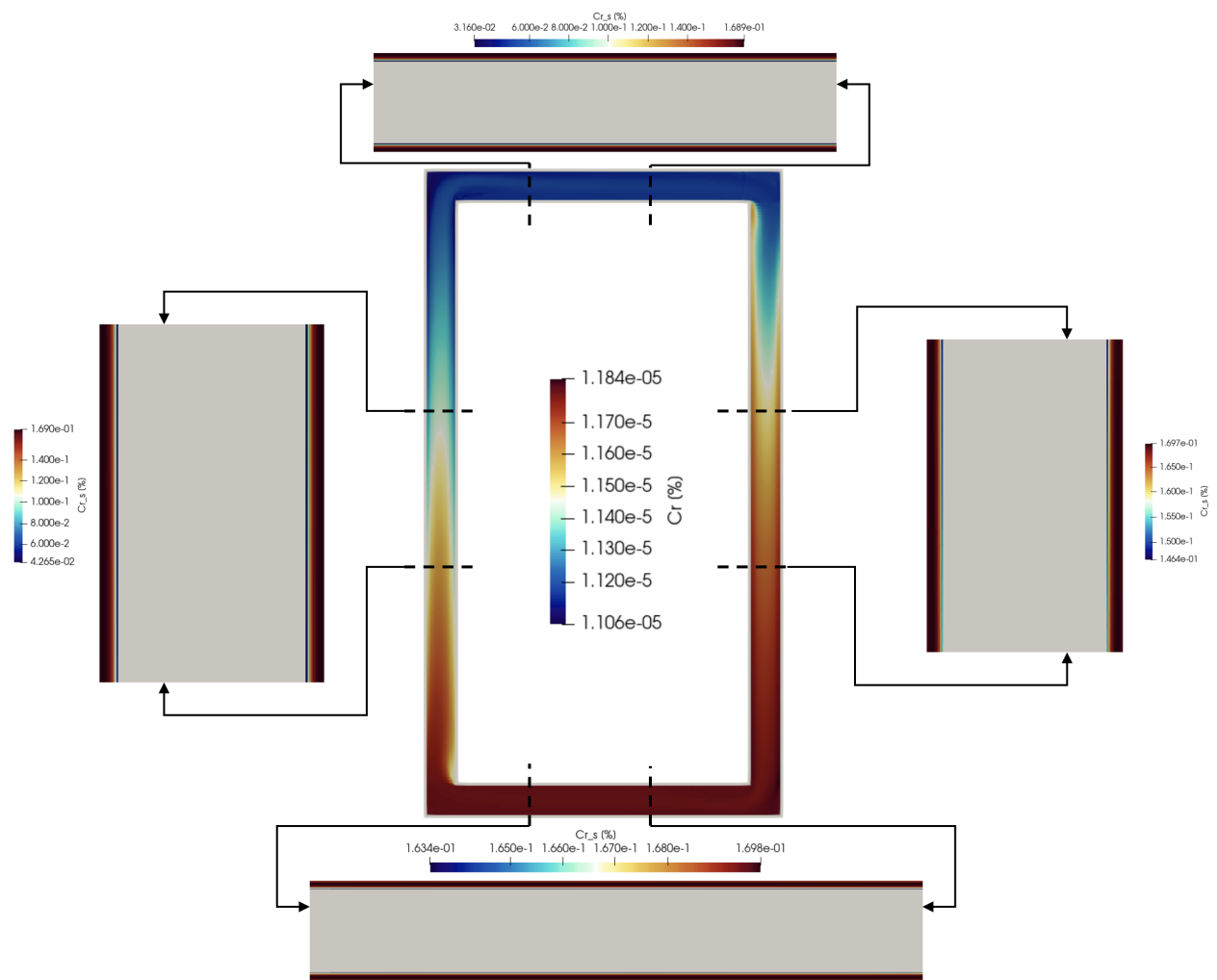


Figure 15. Chromium distribution after 1,000 hours of operation in the demonstration case for a 2D molten salt loop with two-phase flow. The central frame shows the distribution of chromium dissolved in the liquid phase, while the surrounding panels show the percent concentration of chromium in the pipe. Note that a different scale is used for the concentration in the pipe for visualization purposes.

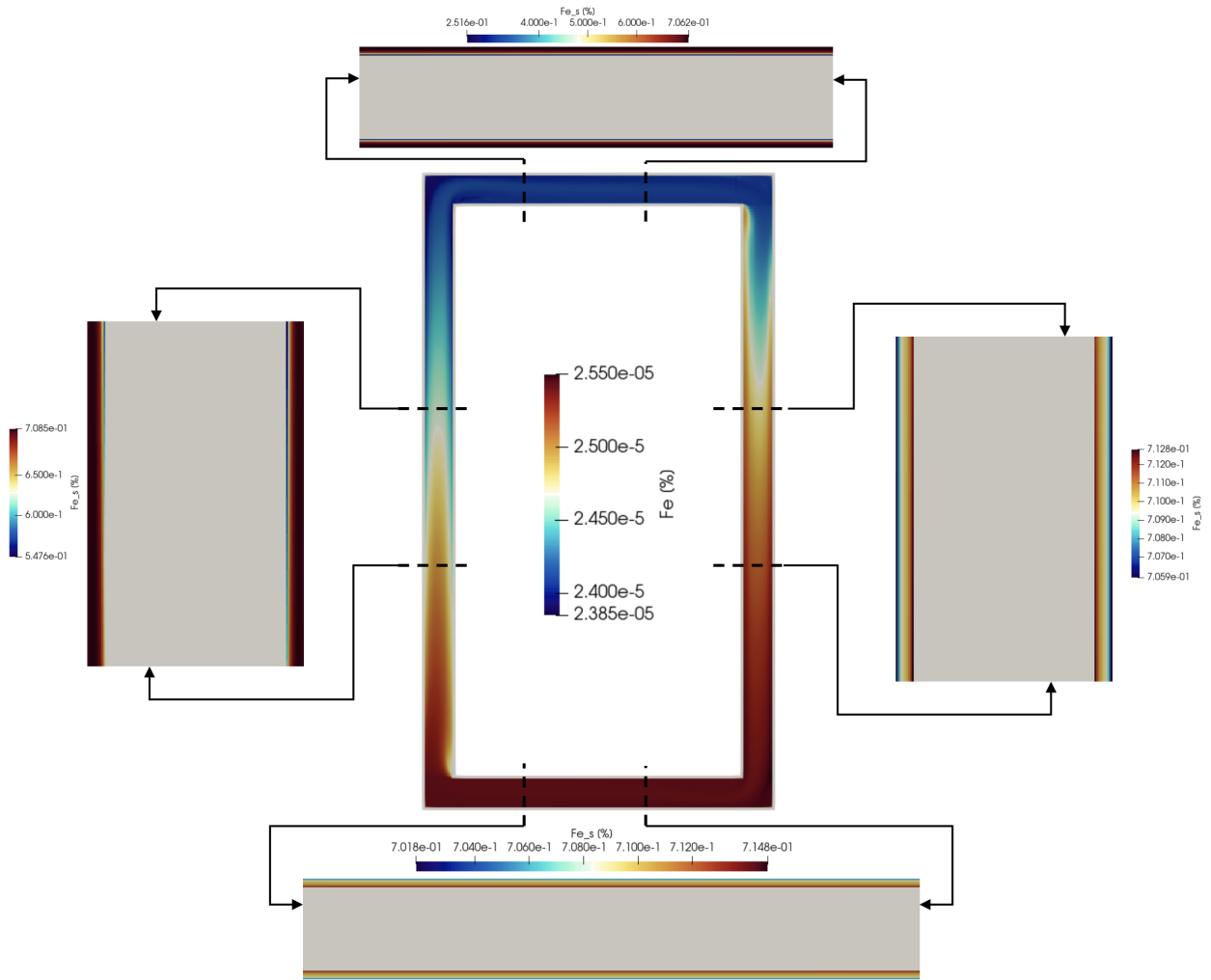


Figure 16. Iron distribution after 1,000 hours of operation in the demonstration case for a 2D molten salt loop with two-phase flow. The central frame shows the distribution of iron dissolved in the liquid phase, while the surrounding panels show the percent concentration of iron in the pipe. Note that a different scale is used for the concentration in the pipe for visualization purposes.

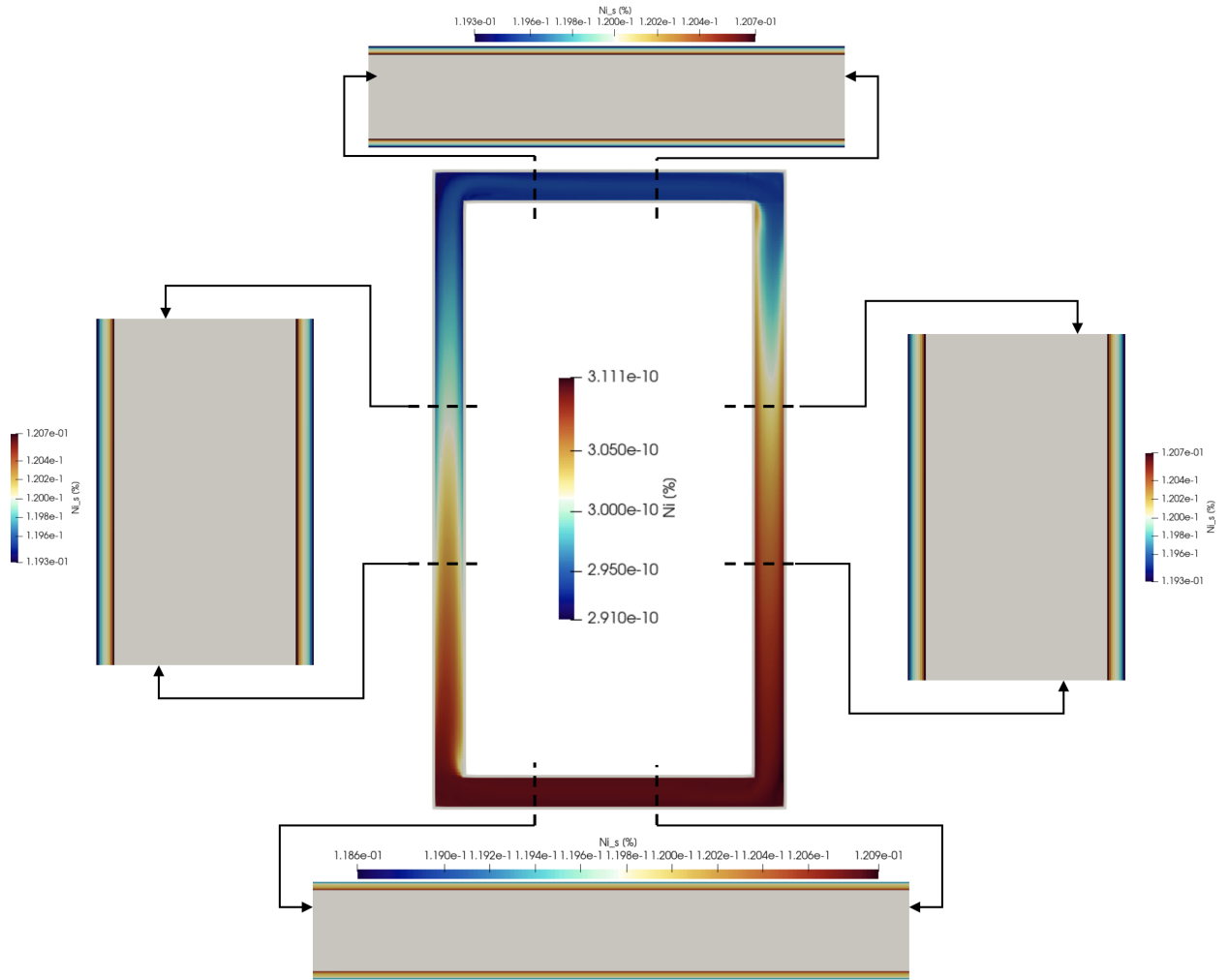


Figure 17. Nickel distribution after 1,000 hours of operation in the demonstration case for a 2D molten salt loop with two-phase flow. The central frame shows the distribution of nickel dissolved in the liquid phase, while the surrounding panels show the percent concentration of nickel in the pipe. Note that a different scale is used for the concentration in the pipe for visualization purposes.

Finally, Figure 18 presents the distribution of corrosion products in the gas phase, including chromium, iron, and nickel. These products accumulate in regions with higher void fractions, indicating that two-phase flow plays a significant role in the transport of corrosion species between the molten salt and gas phases. As the void fraction is extracted in the cold right leg, the concentration of corrosion products in the gas phase decreases, resulting in a continuous leaching of corrosion products into the gas phase.

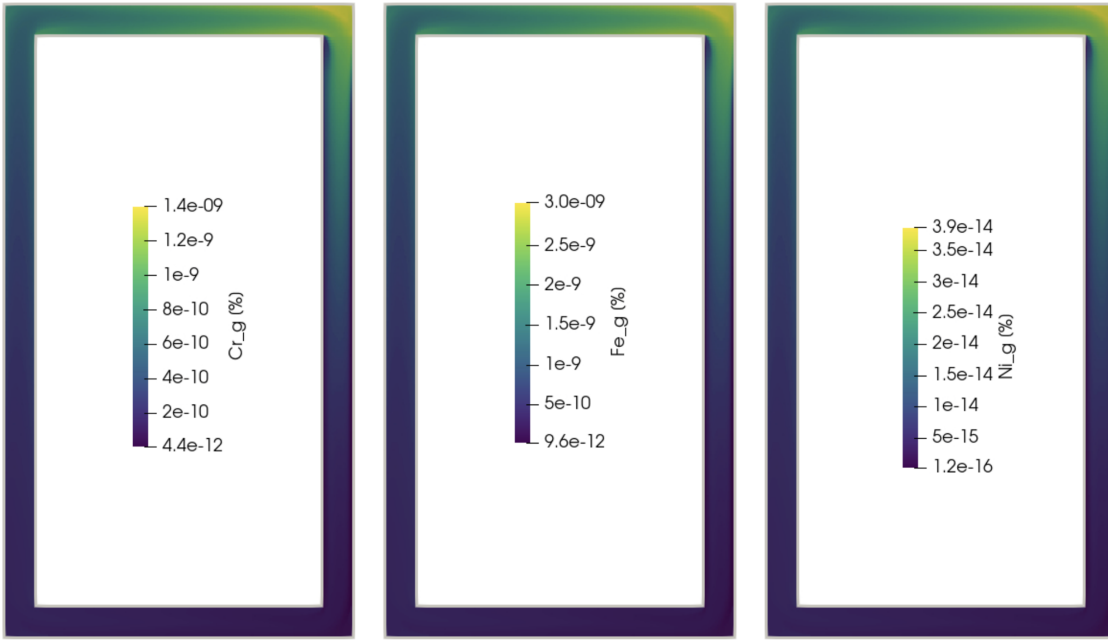
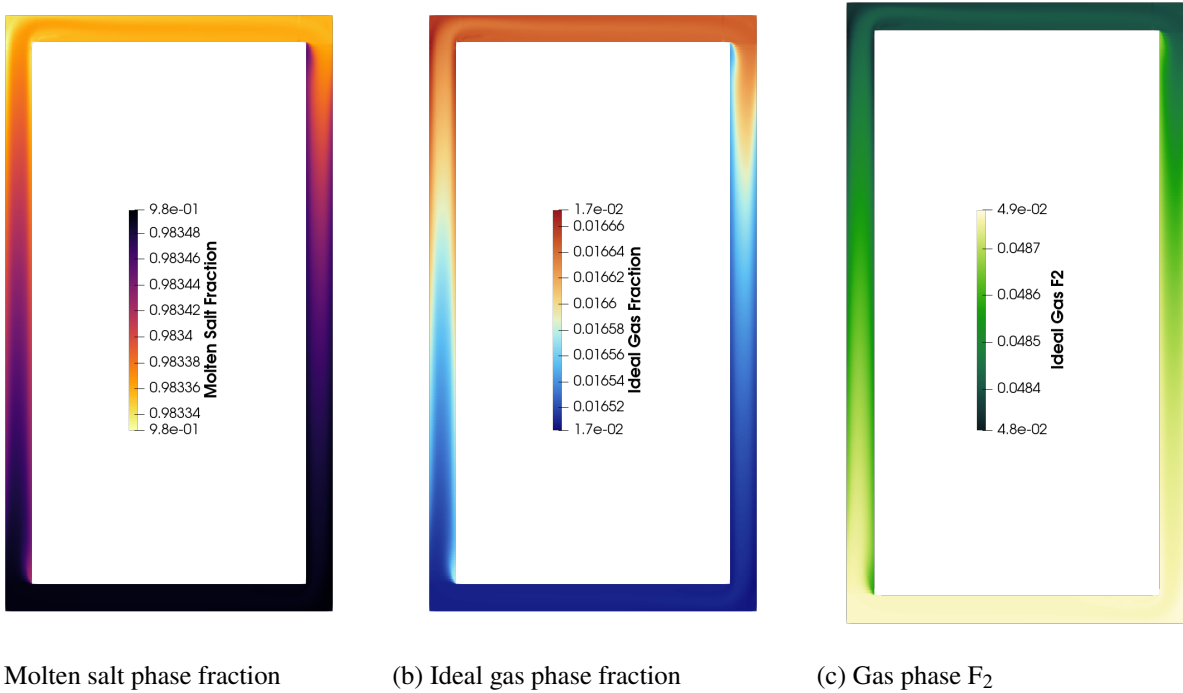


Figure 18. Corrosion product distribution in the gas phase for the system operating at steady-state for the 2D natural convection flow loop demonstration case including chromium (left), iron (center), and nickel (right).

In conclusion, the two-phase molten salt loop simulation demonstrates the multiphysics coupling between two-phase thermal-hydraulic behavior and corrosion product transport. The presence of gas bubbles significantly alters the velocity and temperature fields, affecting the overall distribution of corrosion products in both the molten salt and gas phases and contributing to increased corrosion. Although these results still need to be validated in future work, the observed physical behavior aligns with the expected trends for such systems.

While the corrosion products leach into the molten salt, one must ensure that they remain dissolved on this one and that the mass transfer into the gas phase remains similar to the volatilization rates predicted by equilibrium thermodynamics with Thermochimica. Hence, phase stability and speciation in the molten salt loop are performed with the coupled Thermochimica. For a eutectic composition of the FLiNaK salt used in the loop, the results of phase equilibrium, gas phase speciation, and chemical potential of the corroded elements at time  $t = 300\,000$  s are shown in Figures 19 - 20.

As corrosion products leach into the molten salt, they affect the chemical equilibrium of the mixture, which could result in the volatilization of some of these fission products. This develops a dissolved phase in the fluid salt and an ideal gas phase. The mass fraction of these phases is depicted in Figure 19a and Figure 19b, respectively. The ideal gas fraction generates in the hot leg, due to the added volatilization rate of corrosion products fluorides in these regions. Then, it reduces downstream into the cold branch due to the reduced volatilization rate of these species at lower temperature. Only two phases are present in the internal part of the loop, i.e., there are no precipitates formed under thermodynamic equilibrium conditions. Therefore, the fraction of the molten salt phase is the complement of the ideal gas one.

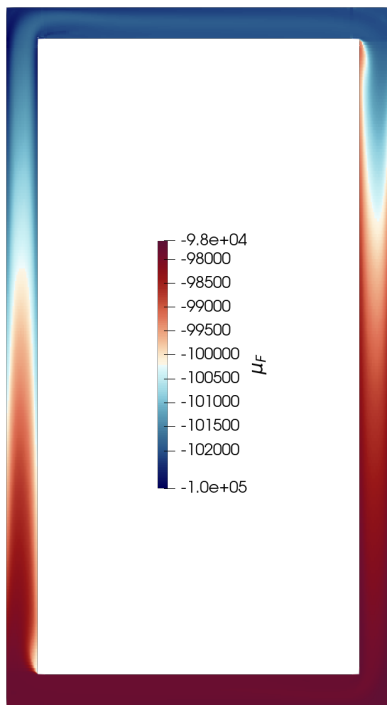


(a) Molten salt phase fraction      (b) Ideal gas phase fraction      (c) Gas phase F<sub>2</sub>

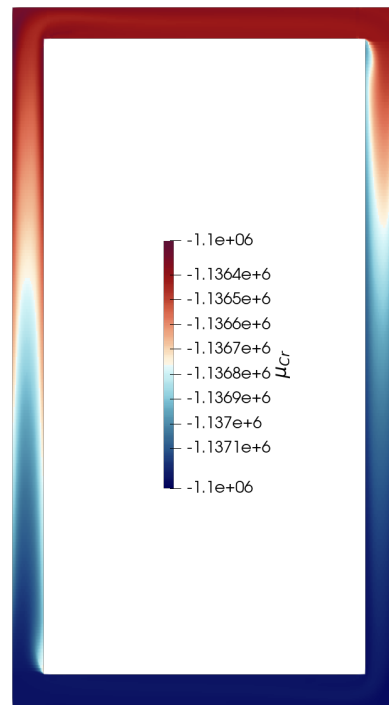
Figure 19. Thermochimica predictions of phase stability and speciation in demonstration loop.

The molten salt loop has been simulated with an excess amount of fluorine of 10% mol/mol. The distribution of this excess fluorine in the loop is depicted in Figure 19c. The fraction of fluorine gas in the ideal gas phase follows the solubility of fluorine in this phase, which increases with temperature. Similarly, the solubility of fluorine in the molten phase decreases with temperature.

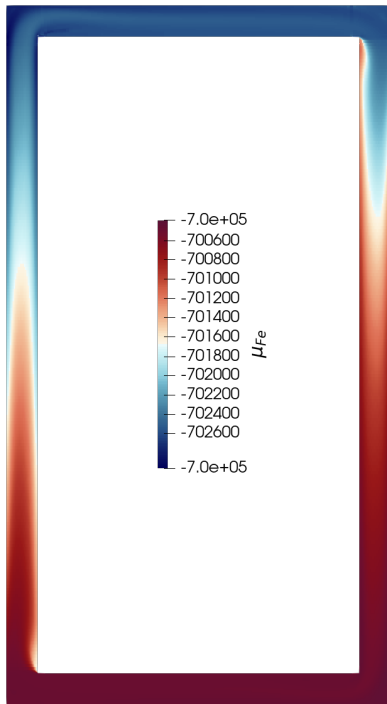
The chemical potential of fluorine is presented in Figure 20a, while the chemical potentials of the dissolved corrosion products chromium, iron, and nickel are depicted in Figures 20b, 20c, and 20d, respectively. As observed, the chemical potential of each of the corrosion products is lower than the one of fluorine. This is expected since all of these corrosion products are being dissolved by the free fluorine in the system, i.e., it is more thermodynamically favorable for a free fluorine to attach to a corrosion products instead of other fluorine. The distribution of the chemical potential of iron and nickel follows the one of fluorine, indicating that these potentials are dominated by the solubility in the salt. The potential of chromium, however, follows more closely the ideal gas distribution, indicating that the chromium fluorides are acting as the chemical buffer in this system.



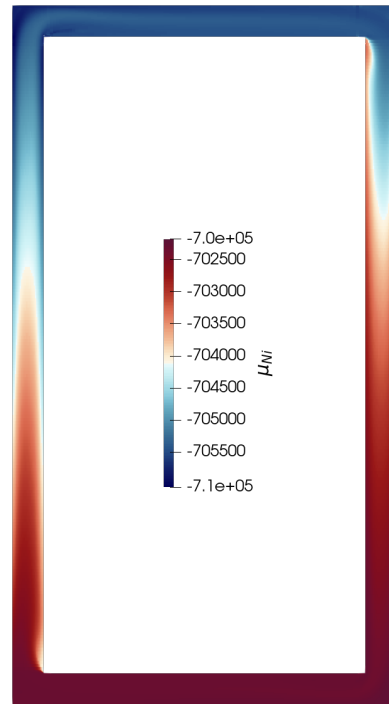
(a) Fluorine potential



(b) Chromium potential



(c) Iron potential



(d) Nickel potential

Figure 20. Thermochimica predicted element potentials in molten salt phase of demonstration loop.

This section demonstrates the coupling of thermal-hydraulics in Pronghorn with two phase flow, with corrosion and phase equilibrium predicted with Thermochimica. However, the exchange current density in the corrosion PNP model is still computed with the linear interpolation model for the activation energy from the formation energy of the reducing and oxidizing species. Future work will look into leveraging the phases chemical potentials in Thermochimica and the predicted equilibrium phase distributions to more accurately compute the activation energy for the redox reactions at the salt-solid interfaces.

### 6.3. 3D Molten Salt Natural Convection Loop

The 3D molten salt natural convection loop provides a more realistic representation of flow and temperature distribution in molten salt systems. Unlike the 2D case with two-phase flow, this case uses a 3D geometry with rounded elbows and a non-Cartesian computational mesh, which is more representative of the type of mesh that would be used in realistic corrosion studies. The test case focuses on natural convection driven by temperature gradients imposed on the solid walls, without the introduction of a gas phase. This setup allows for the evaluation of flow dynamics and corrosion product transport in a fully three-dimensional setting, where the geometrical features more accurately represent practical engineering systems. However, the phenomena expected for this system are more linear than the previous one, as the absence of two-phase flow simplifies the thermal-hydraulics and corrosion behavior.

In this case, the right leg of the loop is heated by imposing a hot temperature of 933.1 K on the right solid wall, while the left leg is cooled via an imposed temperature of 813.2 K on the left wall. The right leg is positioned lower than the left leg, and the temperature difference between the legs drives the natural convection flow. The hot fluid rises in the right leg, while the cooler fluid descends in the left leg, completing the circulation loop. Table 9 summarizes the key parameters used in the simulation of the 3D natural convection loop.

Table 9. Problem parameters for the 3D molten salt natural convection loop demonstration case.

Parameter	Value
Molten Salt	FLiNaK
Pipe	Stainless Steel 316H
Pipe Composition	Fe (71%) - Cr (17%) - Ni (12%)
Heated Wall Temperature	933.1 K (right wall)
Cooled Wall Temperature	813.2 K (left wall)
Operation Time	100 days

Figure 21 shows the steady-state temperature distribution in the molten salt (right panel) and the surrounding solid pipe (left panel). Gravity is pointing downwards in this study. The hot leg, shown on the right side of the loop, exhibits higher temperatures due to the imposed wall heating. The temperature is constant along the wall due to the imposed fixed-temperature boundary condition. As the fluid rises through this leg due to natural convection, it heats up. A thermal boundary layer is observed in the rising flow, with higher temperatures near the wall where the flow is heated. Then, the flow mixes in the top leg, where the temperature of the solid wall and the liquid salt equalizes due to conjugate heat transfer. The flow then cools down in the left leg, where a cooling boundary layer develops as the flow descends through the cooling pipe. In the bottom leg, the cooled flow mixes, and the salt and wall temperatures equalize again due to conjugate heat transfer.

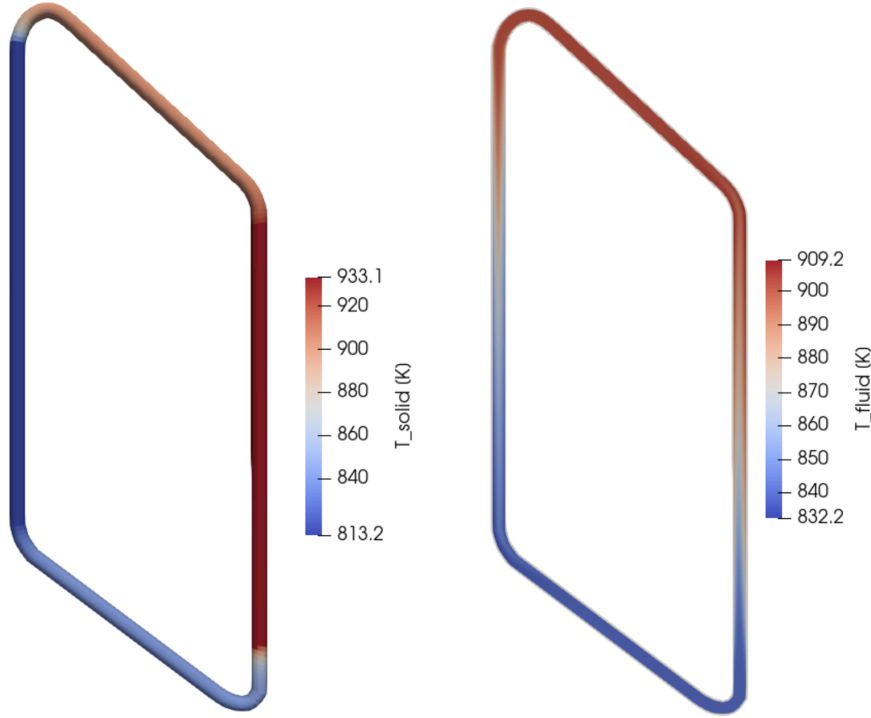


Figure 21. Temperature distribution during steady-state operation of the 3D natural convection loop demonstration case. **Left:** Solid pipe temperature. **Right:** Temperature in the molten salt.

The corrosion product distribution after 100 days of operation is presented in Figures 22, 23, and 24 for chromium, iron, and nickel, respectively. The behavior of these species follows the temperature and flow fields driven by natural convection.

The transport of corrosion products in the straight pipe sections is similar to the previous 2D case. However, in this 3D simulation, some plating of chromium is also observed in the cold leg due to the lower temperature in that region. As the molten salt cools down in the left leg, the reduced solubility of chromium in the cooler fluid leads to a greater tendency for chromium to plate onto the pipe walls.

For chromium, shown in Figure 22, leaching occurs predominantly in the hot right leg, where the elevated temperatures accelerate the corrosion process. As the molten salt circulates through the loop, chromium is carried away from the hot region and gradually deposits in the cooler left leg. The plating of chromium in the cold leg is enhanced by the temperature difference between the hot and cold sections, which drives the transport and deposition of corrosion products.

In the case of iron, depicted in Figure 23, the overall distribution is similar to that of chromium, with iron leaching out in the hot leg and depositing in the cooler leg. However, the extent of iron transport is smaller than chromium due to the lower electrode potential of iron. The transport and deposition patterns observed for iron are similar to those seen in the previous 2D case.

Nickel, shown in Figure 24, exhibits a different behavior compared to chromium and iron. Due to its lower electrode potential, the transport of nickel in the molten salt loop remains much lower. Some nickel leaches into the salt initially, but as the electric potential in the salt increases, most of the nickel plates back onto the pipe walls, particularly in the cooler regions.

In addition to the straight pipe sections, significant corrosion effects are observed at the elbows of the loop. These effects are not isotropic due to the flow dynamics and wall shear forces at the bends. The elbows

experience higher strain rates where the flow velocity is greater. This results in asymmetric corrosion and material degradation, with higher leaching rates in the high-velocity regions. For all corrosion products, this effect is clearly observed in the bottom-right elbow, where leaching occurs on the outer side of the elbow, where higher velocities and shear strain rates are obtained, while deposition is observed on the inner side of the elbow, where the flow is more occluded. A similar effect is observed for the top-left elbow, where the mixing flow field causes asymmetric leaching and deposition profiles.

The non-isotropic nature of corrosion at the elbows is important because these areas are often structural weak points in engineering systems. Understanding and accurately predicting corrosion at the elbows is essential for improving the longevity and reliability of molten salt reactor systems. This work demonstrates the model's capability to predict 3D leaching and deposition profiles in these elbows.

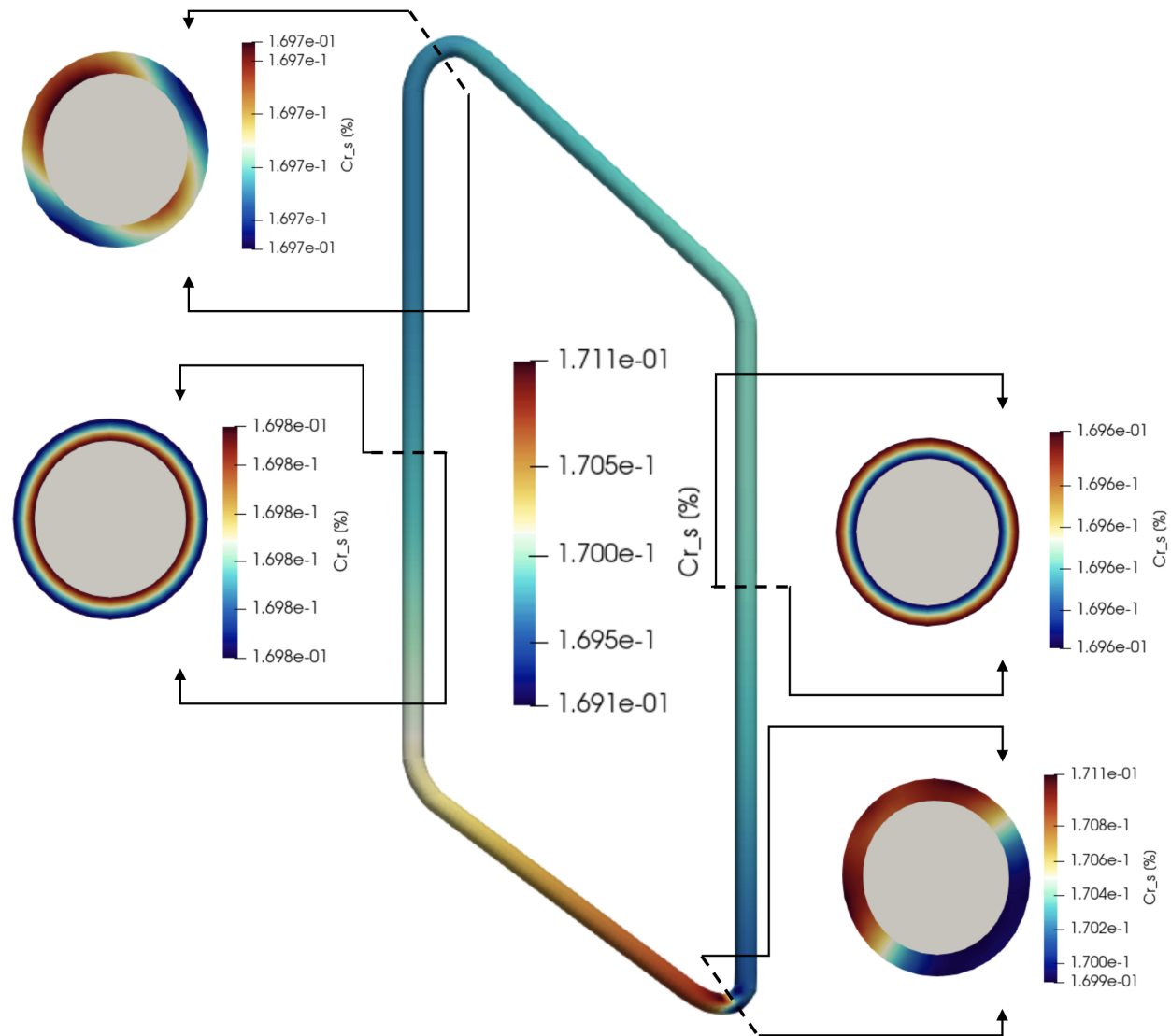


Figure 22. Chromium profile in the molten salt loop pipe for the 3D natural convection loop demonstration case after 100 days of operation.

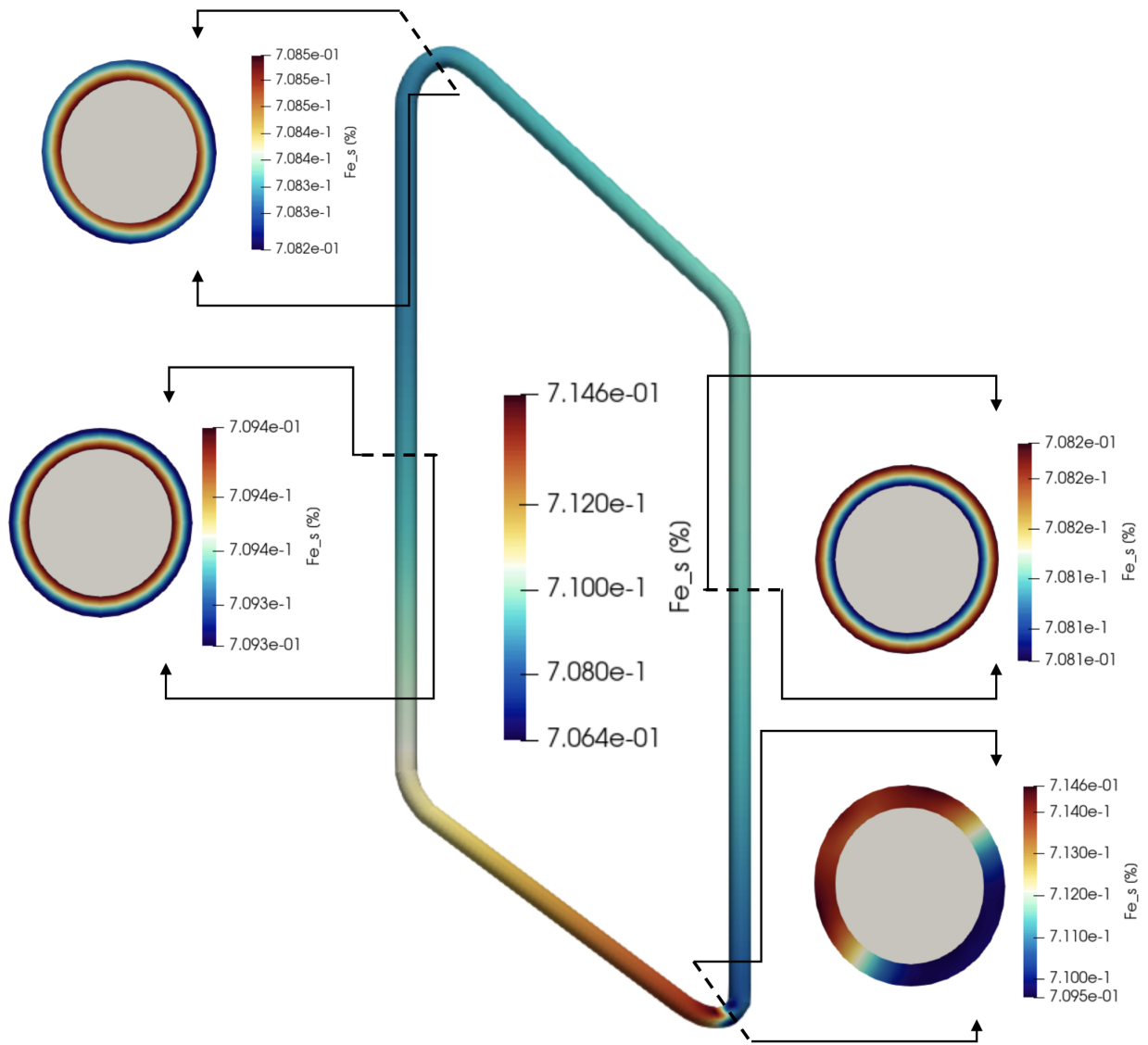


Figure 23. Iron profile in the molten salt loop pipe for the 3D natural convection loop demonstration case after 100 days of operation.

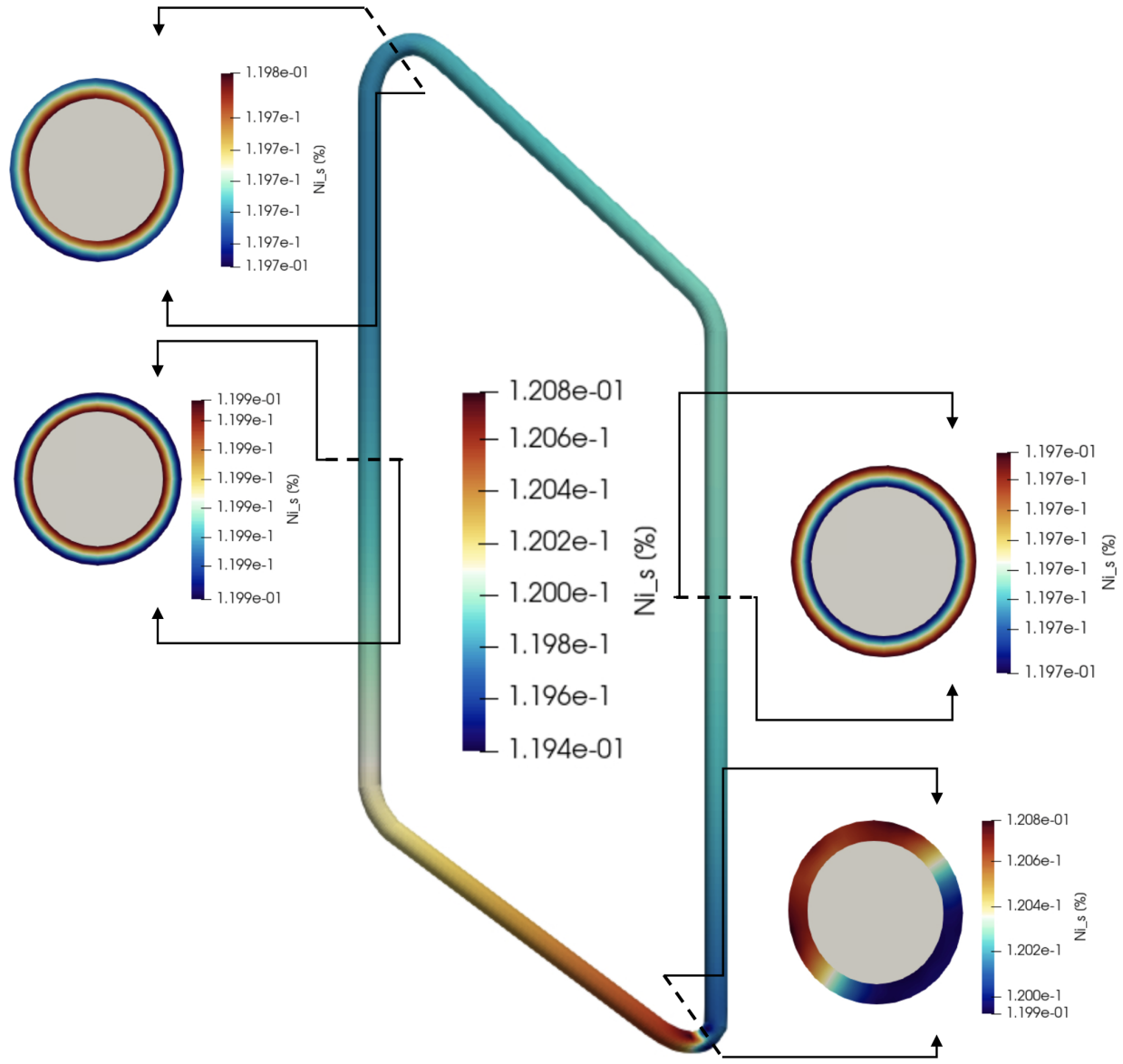


Figure 24. Nickel profile in the molten salt loop pipe for the 3D natural convection loop demonstration case after 100 days of operation.

Figure 25 presents the concentration of chromium, iron, and nickel dissolved in the molten salt after 100 days of operation. The concentrations follow the expected trend, with the concentration of chromium being higher than iron, and the concentration of iron being higher than that of nickel. This is consistent with the expected trends based on the electrode potential of these species. The higher concentrations of chromium and iron in the cold leg are due to the higher density of the cold salt in this region, which causes an accumulation of these species. However, the dissolved concentrations of these species remain approximately constant throughout the loop due to the advective transport. For nickel, the leaching from the hot region compensates for the density effect in the cold leg, resulting in slightly higher concentrations in the hot leg. Nevertheless, the concentration of nickel remains approximately constant throughout the loop, thanks to the advective transport driven by natural convection. In summary, the results indicate that the 3D model can capture the spatial variation of corrosion products throughout the loop.

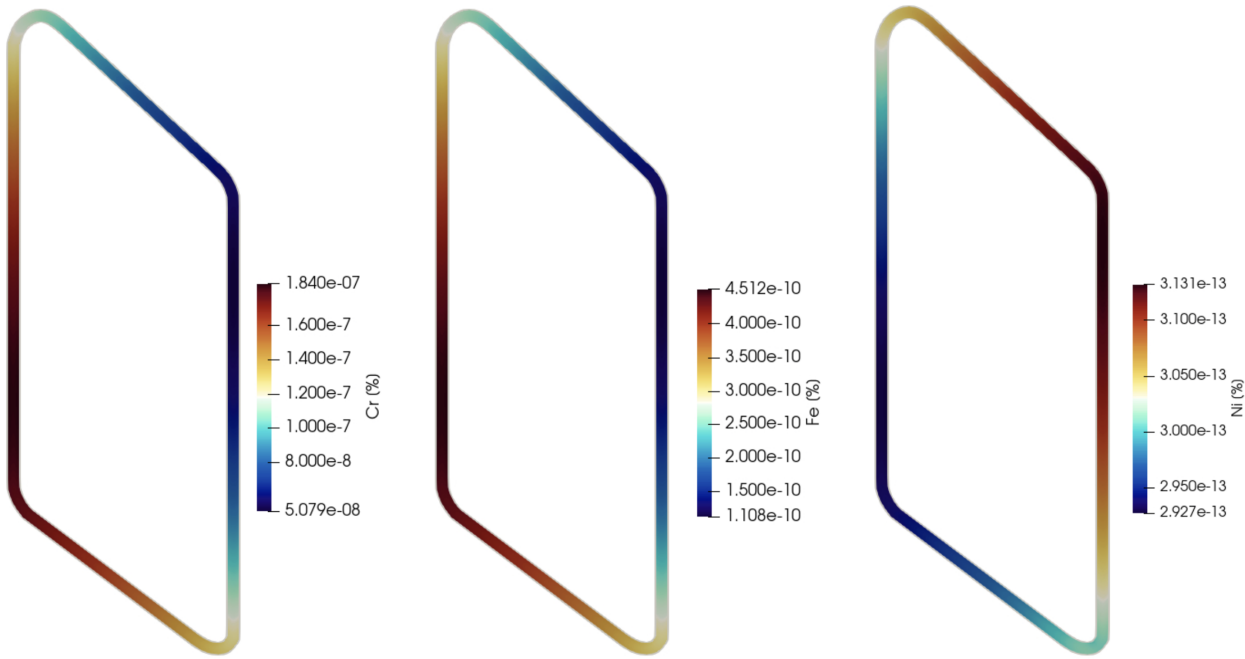


Figure 25. Concentration in the molten salt of corrosion products after 100 days of operation for the 3D natural convection loop demonstration case, including Chromium (left), Iron (center), and Nickel (right).

In conclusion, the 3D molten salt natural convection loop demonstrates the effect of temperature gradients on the circulation of molten salt and the distribution of corrosion products. The transport of corrosion products in the straight sections is similar to the 2D case, but additional chromium plating is observed in the cooler leg. The elbows in the loop exhibit non-isotropic corrosion effects due to complex flow dynamics, highlighting the importance of accounting for these geometrical features when modeling the long-term corrosion performance of molten salt components. The use of a realistic 3D geometry and computational mesh provides a more accurate representation of practical molten salt systems, underlining the significance of including geometrical effects in the assessment of material degradation.

## 7. FULL MSR LOOP DEMONSTRATION CASES

The previous section have presented simulations of coupled corrosion, two-phase flow, and Thermochimica-predicted speciation for simple moten salt loops. However, the situation is more complicated for full MSRs, where these physics are coupled with the depletion of the fuel salt.

This section presents some of the full MSR loop demonstration cases showcasing the integration Thermochimica within the MOOSE framework for multiphysics modeling and simulation the full primary loop MSRs. Utilizing Thermochimica coupled with various NEAMS codes allows for novel MSR physics to be modeled including depletion-driven thermochemistry, corrosion and fuel-salt redox control, and thermochemical speciation of chemical species for off-gas system design and source term characterization. In the following examples, both steady-state and transient analyses of full MSR cores and primary loops will be presented and discussed.

Before showcasing the full loop MSR demonstration cases of coupling Thermochimica within the MOOSE framework, it is essential to discuss the importance of the thermochemical database being used by

Thermochimica for MSR-related modeling and simulation. As previously introduced, the thermochemical database of choice is the Molten Salt Thermal Properties Database-Thermochemical (MSTDB-TC) [33].

The following results use MSTDB-TC V3.1 as the thermochemical database for both fluoride and chloride salt systems. MSTDB-TC V3.1 is the state of the art of self consistent thermochemical data of molten salt systems which incorporates actinides, base salt constituents, fission products, and corrosion products. Both the fluoride and chloride system include the recent addition of iodine which allows for the chemical behavior of this fission product in MSR systems to be determined. This, in addition to other fission products, allows for the multiphysics modeling of chemical speciation of volatile gases by coupling equilibrium thermochemistry via Thermochimica with the two phase flow models described earlier.

## 7.1. Lotus Molten Salt Reactor

The first example is of the Lotus Molten Salt Reactor (L-MSR) which is based on the open-source specifications of the Molten Chloride Reactor Experiment (MCRE) [34]. The generic L-MSR is depicted in Figure 26. The primary components of the MSR loop include a core pool, a pump, and the piping that connects the reactor to the pump. Here the liquid nuclear fuel flows upwards through the reactor cavity and is then pumped back around through the return piping.

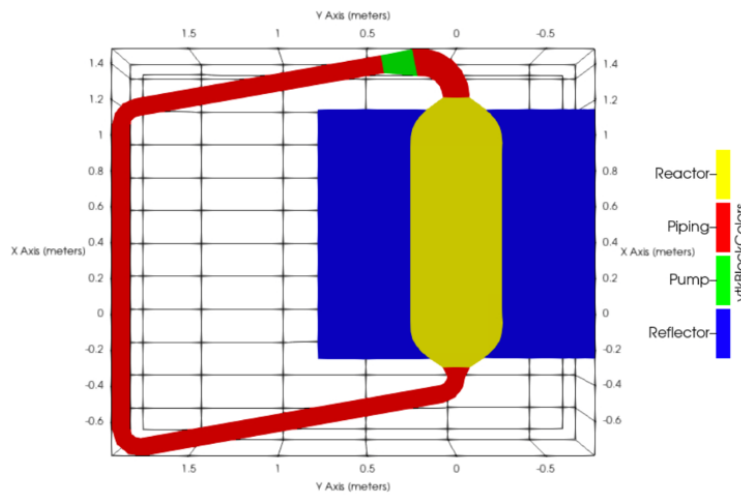


Figure 26. Geometry for the 3D Lotus Molten Salt Reactor

The specific design parameters of the reactor important for thermochemical modeling are summarized in Table 10. The fuel salt composition corresponds to the eutectic point of the  $\text{UCl}_3\text{-NaCl}$  system. The thermophysical properties of the nuclear salt and the reflector are based on best-estimate values from open literature. A mass flow rate of 100 kg/s is assumed for the steady-state operation of the L-MSR. At this mass flow rate, the nominal pressure drop across the reactor loop is approximately 139 kPa.

Table 10. Key modeling parameters of the L-MSR

Parameter	Value
Core Power [kW <sub>th</sub> ]	25
Operation Temperature [K]	900
Mass Flow Rate [kg s <sup>-1</sup> ]	100
Fuel Salt Composition [mol %]	NaCl [33.3%] - UCl <sub>3</sub> [66.6%]
Fuel Salt Density [kg m <sup>-3</sup> ]	$\rho = 4.213 \times 10^3 - 1.0686T$

The temperature and pressure profiles in LMSR are shown in Figure 27 along with the resulting chemical potential of chloride (Cl<sup>-</sup>), the primary anion in the system. Here, the NEAMS codes Griffin and Pronghorn are used to calculate the temperature and pressure profiles due to multiphysics modeling of the reactor neutronics and thermal-hydraulics. Subsequently, Thermochimica takes the temperature and pressure fields along with the changing fuel salt composition due to depletion to determine chemical equilibrium snap-shots of L-MSR at various points during depletion.

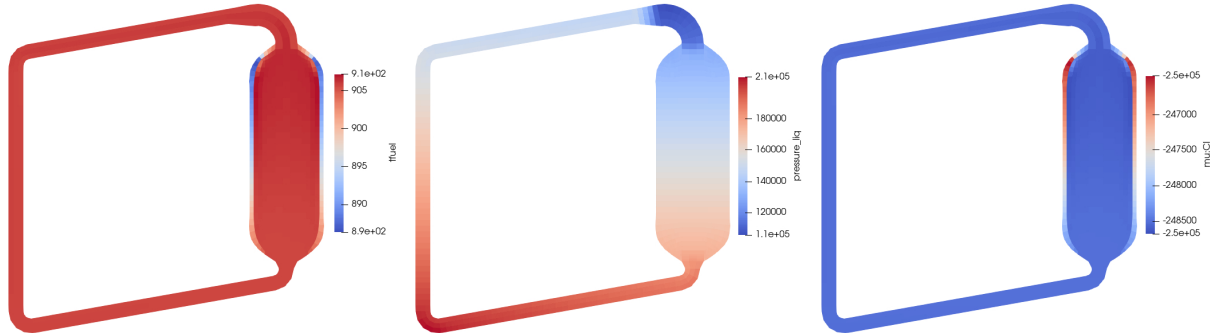


Figure 27. Thermochemically important fields within L-MSR at steady-state operation: (a) temperature [K], (b) pressure [Pa], (c) chemical potential of chloride (Cl<sup>-</sup>) [J mol<sup>-1</sup>].

In addition to calculating the chemical potentials of elements in the molten salt system, Thermochimica also calculates the stable ideal gas phase present in the reactor due to fission product formation of noble gases and the associated minor amounts of chemical species that volatilize into gas phase. The amount of volatilization is dependent on the pressure, temperature, and chemical potential of the primary anion in the fuel salt (i.e., F<sup>-</sup> or Cl<sup>-</sup>). Figure 28 showcases the total ideal gas phase that would be present in L-MSR if there was no off-gas system to extract the primary gas phase. The ideal gas phase predicted by Thermochimica is generated due to noble gases such as xenon which as modeled assumes there is no xenon transport into the structural material or extracted into an off-gas system.

Additionally, Figure 28 illustrates the volatilization of gaseous RbCl and CsI, rubidium, cesium, and iodine being the more volatile of fission products within molten salts. However, given the minor burnup expected and solubility of these species in the chloride salt predicted by the thermochemical database, the volatilization of chemical species is extremely minuscule with concentrations in the parts per trillion within the ideal gas phase. This is an anticipated outcome for normal reactor operation of MSR systems, but should be qualified in that the volatilization of chemical species is heavily dependent on the temperature, pressure, and redox potential (i.e., fluoride or chloride chemical potential) of the fuel salt which can all be drastically changing during severe accident scenarios.

As seen in Figure 28 the volatilization of chemical species into the ideal gas phase occurs in low-pressure,

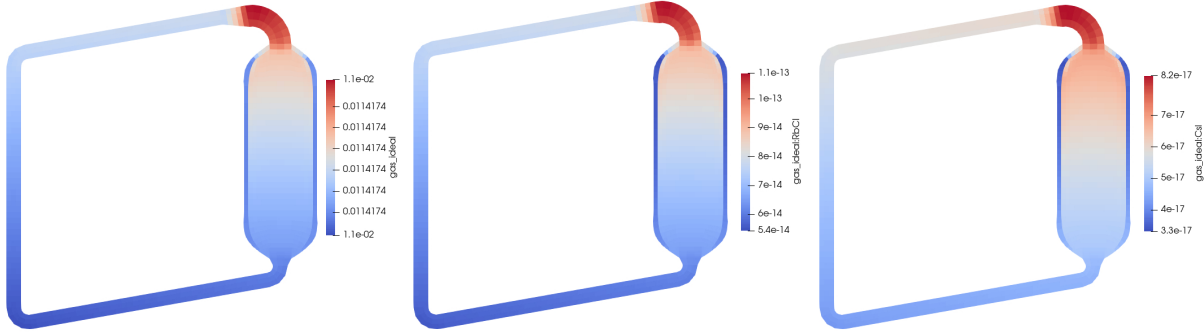


Figure 28. Volatilization of noble gases and chemical species within L-MSR at steady-state operation: (a) ideal gas phase distribution [ $\text{mol m}^{-3}$ ], (b) RbCl gaseous species distribution [ $\text{mol m}^{-3}$ ], (c) CsI gaseous species distribution [ $\text{mol m}^{-3}$ ].

high-temperature regions like the top of the core before the pump making this a suitable place to incorporate an off-gas system.

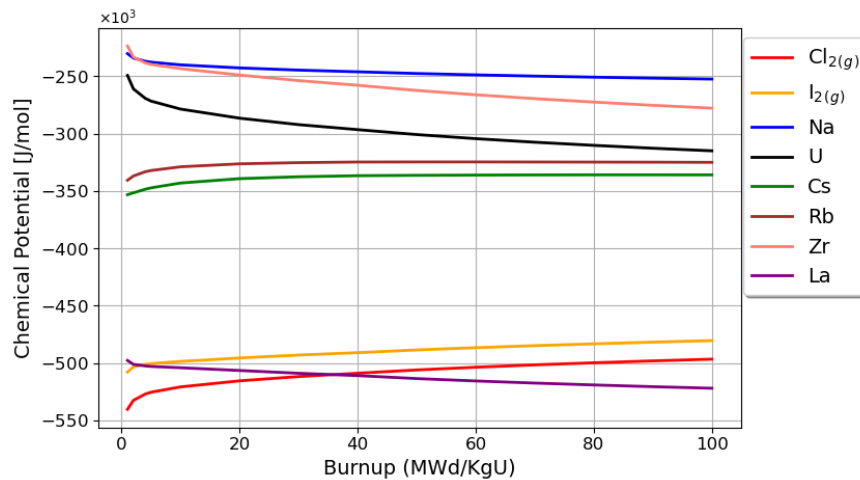


Figure 29. Changing chemical potentials of fuel salt constituents during depletion in L-MSR

Lastly, the effect of depletion-driven chemistry where consumption of uranium fuel due to fission has a measurable impact on the resulting redox potential of the fuel salt which correspondingly affects the volatilization of chemical species and corrosion processes[35]. This effect is illustrated in Figure 29. The chemical potentials of elements in the L-MSR fuel salt throughout burnup are shown here where there is a decrease in the chemical potential of uranium due to fission, and a subsequent increase in the chlorine (i.e.,  $\text{Cl}_2$ ) potential. Additionally, the chemical potential of fission products cesium, rubidium, and iodine increase throughout burnup, whereas rare earth fission products represented by lanthanum decrease throughout reactor despite their increasing concentration. This fact showcases the relative solubility of these elements within the chloride salt, where cesium, rubidium, and iodine volatility slowly increases due to the consumption of uranium and increase of chlorine potential, whereas rare earth metals become increasingly stable within the liquid phase of the chloride salt.

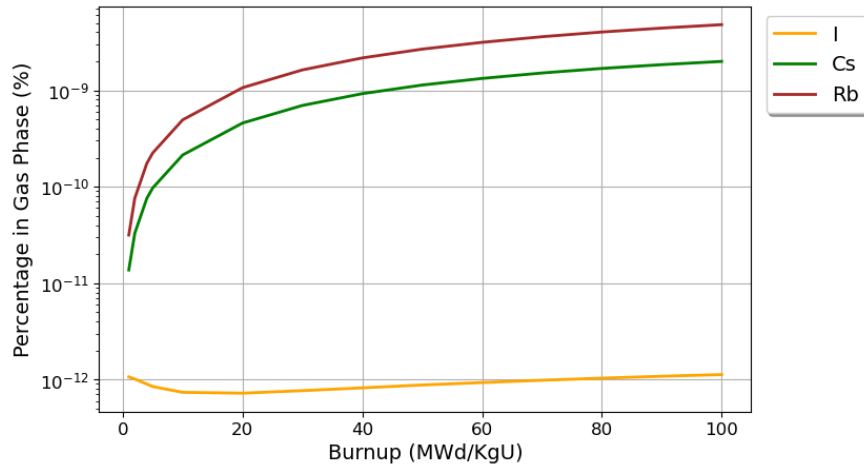


Figure 30. Increasing volatilization of chemical species due to depletion in L-MSR.

This is further illustrated in Figure 30 which shows the increasing percentage of iodine, cesium, and rubidium present in the ideal gas phase created by noble gases in L-MSR. This result sums up all of the gas species of which RbCl and CsI as shown in Figure 28 are two of the biggest contributors. Here the increasing percentage of these species in the ideal gas phase is due to the increasing chemical potential of these elements throughout depletion without active redox control. However, it should be noted that with the given depletion history, iodine, cesium, and rubidium still remain quite stable with concentrations in the gas phase of parts per trillion to parts per billion.

This effect can become increasingly significant for high burnup designs and will require active chemistry control of MSR systems in order to prevent excess volatilization of source term significant radionuclides. The effect of redox potential transients is further examined in the next full loop MSR example.

## 7.2. Molten Salt Reactor Experiment

The Molten Salt Reactor Experiment (MSRE) operated from 1965 to 1969 at Oak Ridge National Laboratory and demonstrated the feasibility of molten salt reactors [36]. To this day it offers the most robust experimental data available for modeling MSR specific multiphysics including fuel salt redox potential measurements, volatilization of chemical species into the off-gas system, and circulating fuel reactivity effects. The MSRE operated with a thermal power output of 10 MW and used a fuel-salt mixture of uranium tetrafluoride ( $\text{UF}_4$ ) along with lithium, beryllium, and zirconium fluorides.

Here a 2D axisymmetric model of the MSRE is presented which captures the primary multiphysics behavior of the system by incorporating neutronics, thermal-hydraulics, and thermochemistry. This model is schematically shown in Figure 31. Here the fuel salt undergoes fission in the graphite moderated core and flows upwards through the riser to where it is pumped out through the rest of the primary loop (i.e., return piping, downcomer, and lower plenum).

A unique feature of the MSRE was its management of gaseous fission products which can be seen in the gas removal label at the top of the MSRE model. Here a flow bypass line was used to extract 5% of the mass flow from the pump outlet to a toroidal gas-liquid spray tower contactor shown in Figure 32. Gaseous fission products such as xenon and krypton were extracted through this spray tower to prevent performance and safety issues.

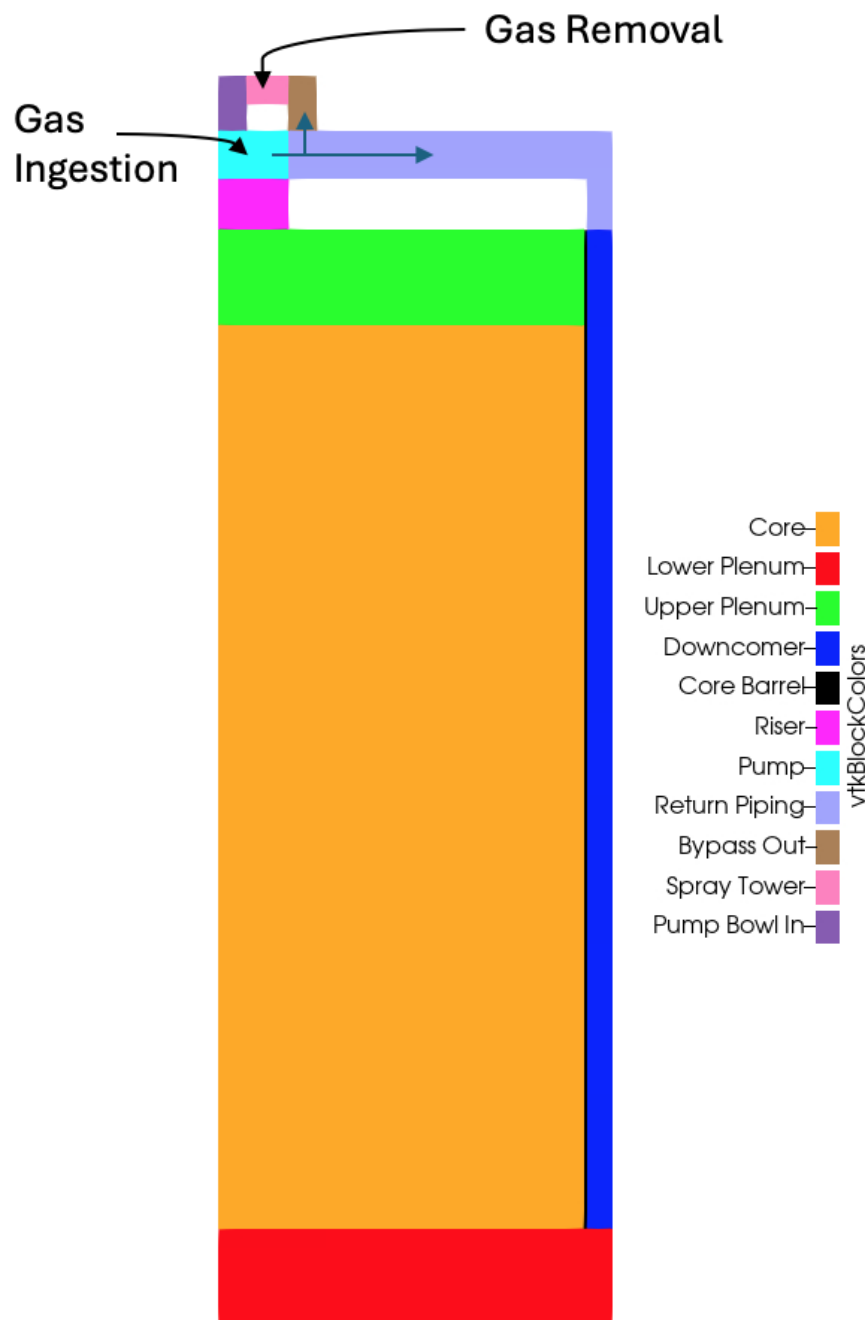


Figure 31. Axisymmetric Griffin-Pronghorn-Thermochimica model developed for MSRE.

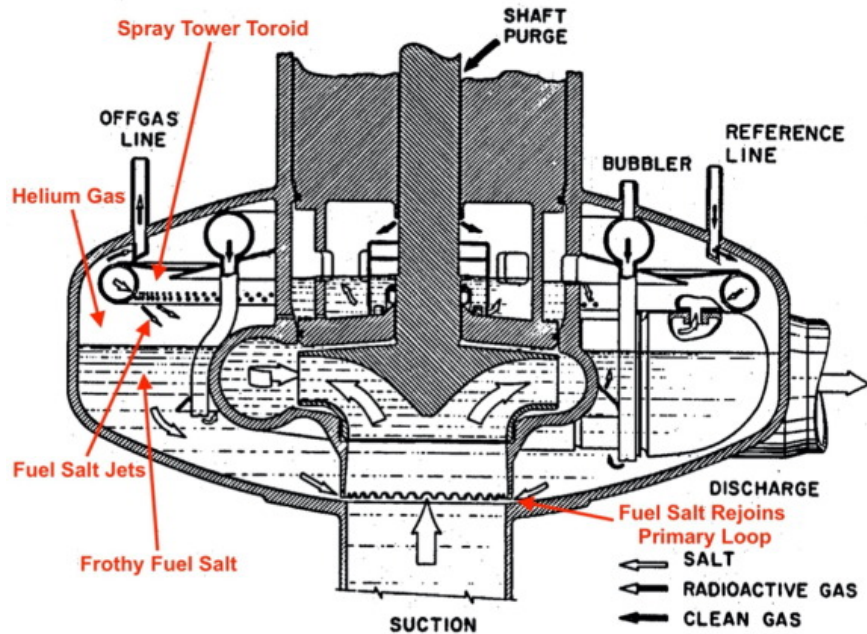


Figure 32. MSRE Pump Bowl Schematic[1].

In the 2D axisymmetric model, gas extraction is simulated by using a volumetric sink term to represent the loss of volatile species via the mass transfer equivalent of the Dittus Boelter correlation[29] as described earlier. This mass transfer coefficient  $K$  and the interfacial area of the gas-liquid contactor are used within the interphase mass transfer equation to determine the effective volumetric sink term for species being extracted in the pump bowl to the off-gas system.

Incidentally, helium gas from the gas-liquid contactor in the pump bowl was periodically, and in some cases consistently, ingested into the primary loop via helium entrainment from the impinging jets as shown in Figure 32 thereby creating a measurable void within the reactor core[1]. This phenomena is modeled in a reduced order fashion by defining a volumetric helium source in the pump which is correspondingly tuned to create the void of 0.5% measured in the MSRE core during the experimental runs which used U-233 fuel.

Utilizing the new modeling capability of species transport between liquid and gas phases within the MOOSE framework allows for the determination of the volatilization of chemically reactive fission products (i.e., non-noble fission products like iodine, rubidium, and cesium). These elements are typically highly soluble in molten salts as shown in the previous section. However, given temperature, pressure, or redox potential transients the volatility of these elements changes accordingly. Using the mass transfer correlation for bubbles with a mobile interface, the effective circulating helium void mass transfer source term for the fractional volatilization of chemical species in the molten salt can be determined. Subsequent noble gases and the fractional chemical species counterparts in the void phase extraction to the off-gas system can be modeled to determine time dependent element and radionuclide inventories within the MSRE.

### MSRE Steady State Operation

The following example showcases the Thermochimica and MOOSE chemical species transport with two-phase flow mixture model for tightly coupled multiphysics analysis of the Molten Salt Reactor Experiment at steady-state operation. Figure 33 showcases the temperature, pressure, and resulting fluoride potential  $F^-$  in the MSRE during steady-state operation. The temperature, pressure, and velocity were calculated using Griffin-Pronghorn multiphysics models of tightly coupled neutronics and thermal-hydraulics. Thermochimica

then calculates the chemical potential of fluoride in the system (i.e., the redox potential of the fuel salt) given the elemental composition of the MSRE fuel salt.

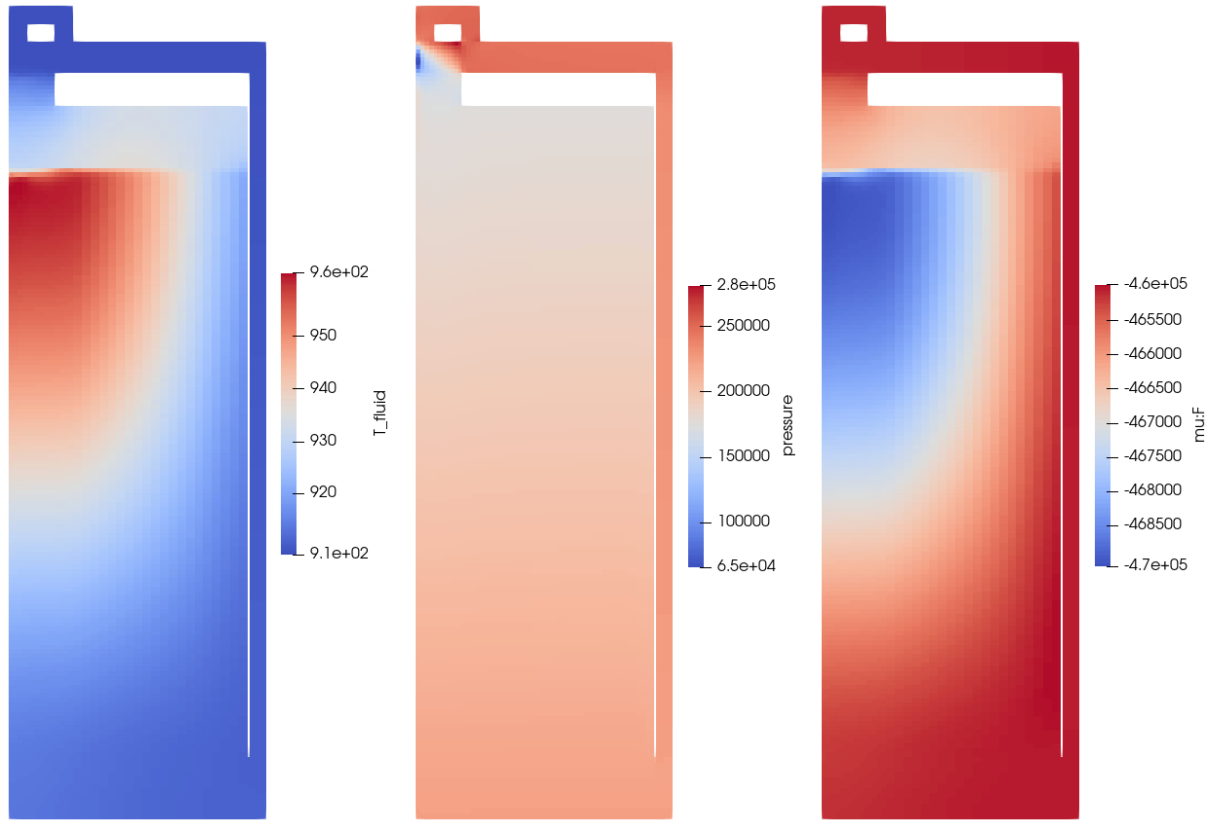


Figure 33. Thermochemically important fields within MSRE at steady-state operation: (a) temperature [K], (b) pressure [Pa], (c) chemical potential of fluoride ( $F^-$ ) [ $J \text{ mol}^{-1}$ ].

Next the circulating helium void is generated with a tuned volumetric source for helium in the pump, and a volumetric extraction rate calculated by the mass transfer Dittus Boelter correlation in the toroidal spay tower gas-liquid contactor as seen in the steady-state ideal gas phase in Figure 34. Additionally, the resulting ideal gas void (made mostly of helium gas) is also shown in Figure 34 along with the effective circulating void mass transfer source term (i.e.  $a_i K_k$ ) for the fractional volatilization of chemical species using the mass transfer coefficient for bubbles with mobile interfaces.

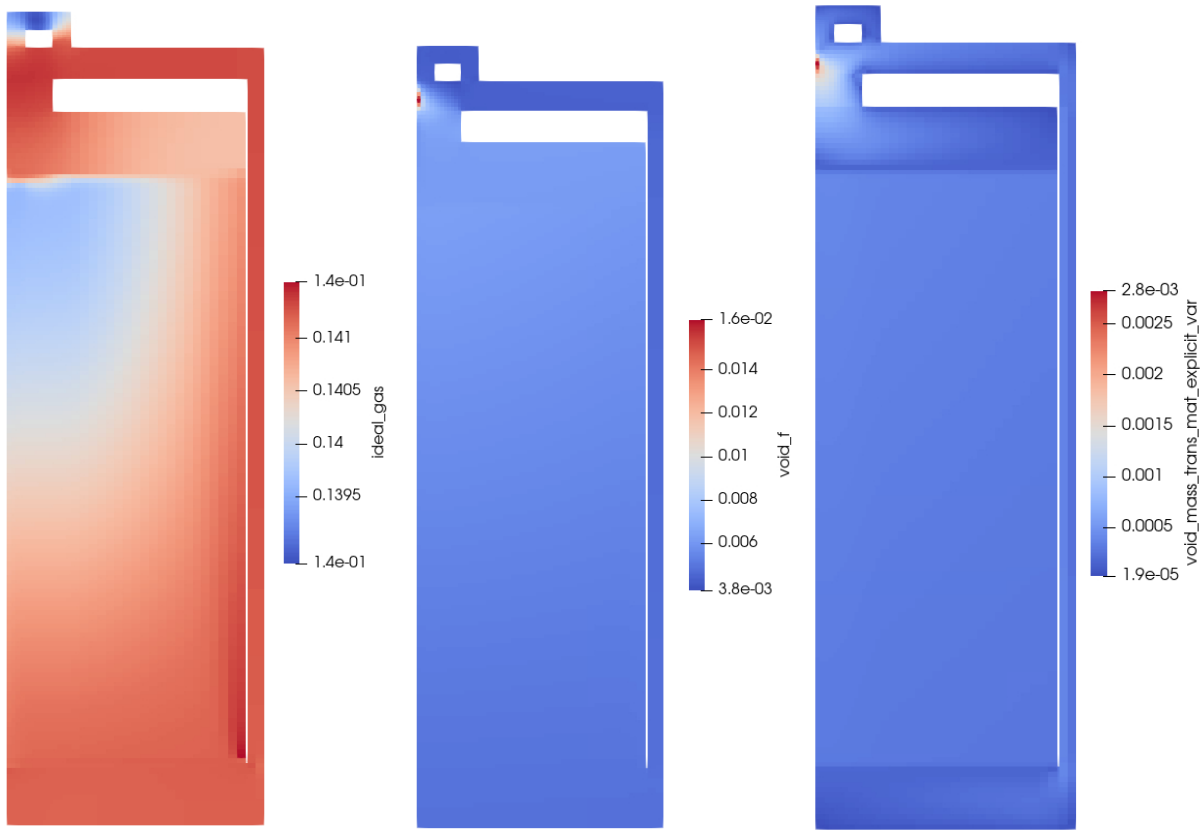


Figure 34. Circulating helium void in MSRE at steady-state operation: (a) ideal gas phase distribution [ $\text{mol m}^{-3}$ ], (b) ideal gas void volume [ $\text{m}^3$ ], (c) effective circulating void mass transfer source term for fractional volatilization of chemical species [ $\text{m}^3$ ].

Using the fission source calculated by Griffin, generic fission product element fields are generated for illustration purposes to showcase the new spatially resolved thermochemistry capabilities of Thermochemica within MOOSE. Figure 35 showcases three element distributions in both the liquid molten-salt phase, and the gaseous ideal-gas phase. The elements are rubidium, iodine, and cesium, and were chosen as a demonstration case since these three elements show some limited fractional volatility as opposed to rare earth fission products which are effectively completely non-volatile in fluoride salts.

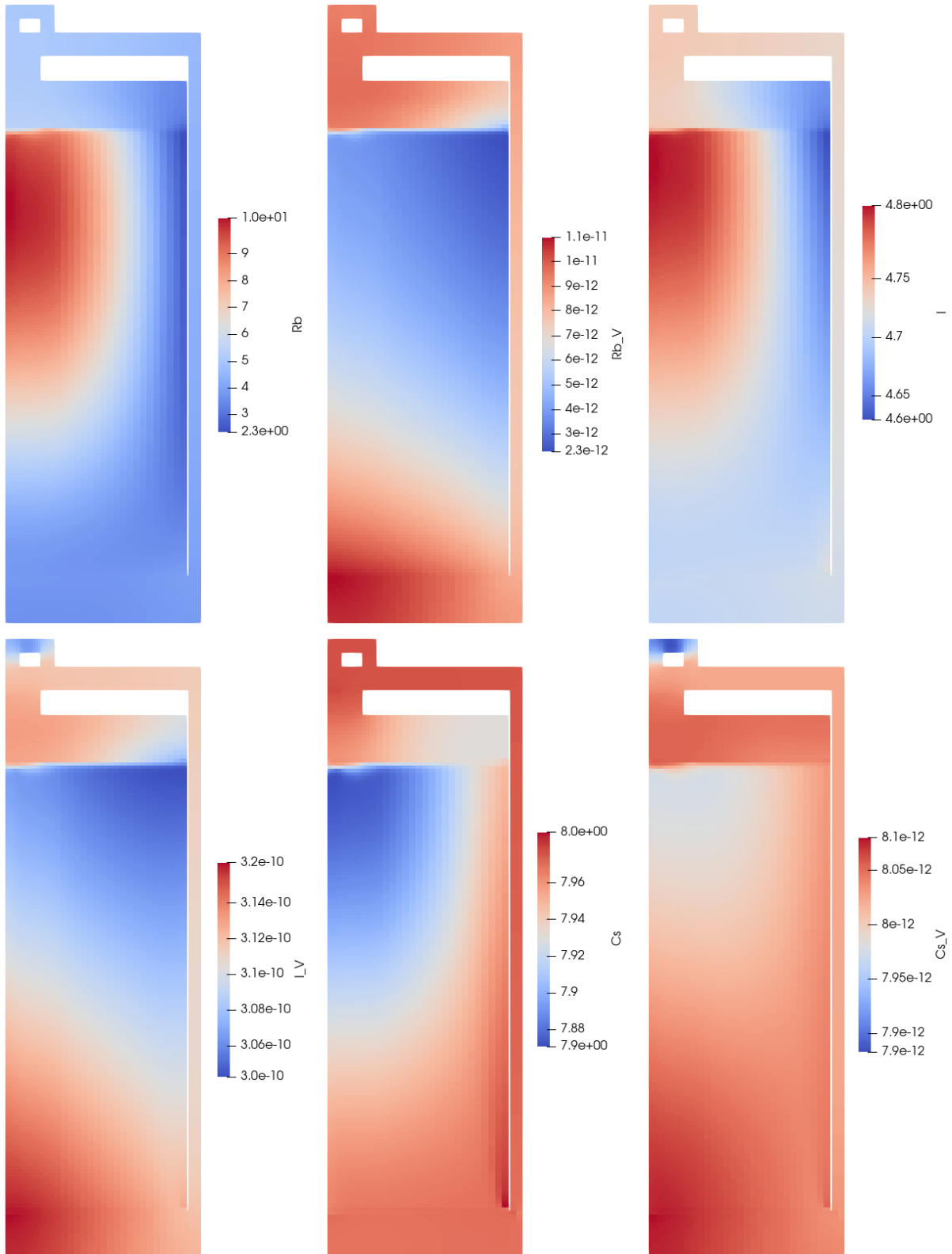


Figure 35. Fission product element fields in MSRE at steady-state operation: (a) concentration of rubidium in the liquid phase [ $\text{mol m}^{-3}$ ], (b) concentration of rubidium in the gaseous phase [ $\text{mol m}^{-3}$ ], (c) concentration of iodine in the liquid phase [ $\text{mol m}^{-3}$ ], (d) concentration of iodine in the gaseous phase [ $\text{mol m}^{-3}$ ], (e) concentration of cesium in the gaseous phase [ $\text{mol m}^{-3}$ ], (f) concentration of cesium in the gaseous phase [ $\text{mol m}^{-3}$ ].

The fission product element distributions were artificially selected to effectively condense all the fission product radionuclides within that element with a single group condensed fission yield and decay constant. Therefore the effect of spatially resolved thermochemistry is overly emphasized for demonstration purposes where rubidium is the most localized element due to its short half-life of 30 seconds, iodine is moderately distributed due to its medium half-life of 30 minutes, and cesium is basically homogenously distributed with its long half-life of 75 days. The corresponding concentration of these elements in the circulating helium void is on the order of parts per trillion at steady-state similar to what was shown in the L-MSR case. This can be attributed in part to the reduced state of the fluoride potential which gives low volatility of chemical species and low corrosion rates.

### MSRE Fluorination Pulse Transient Demonstration

This next demonstration is another generic example to showcase the Thermochimica in MOOSE modeling capabilities for chemical species volatilization and two-phase species transport for thermochemical transients. Here a fluorination pulse transient is modeled where a large amount of fluorine gas (i.e.,  $F_2$ ) is sparged into the MSRE pump for a 1 second period. It should be noted that this is not an expected transient within an MSR primary loop. However this fluorination process was used during the MSRE in another controlled environment outside of the primary loop to swap out the fuel salt from U-235 enriched to U-233 enriched fuel. It is shown here to illustrate the new reacting chemical flow modeling capability available with Thermochimica coupled with the two-phase flow chemical species transport model within MOOSE.

Figure 36 showcases the one second fluorination pulse within the pump in the MSRE. Here the total fluorine gas, total void, and total iodine gas are shown. The fluorine gas pulse is the source of the rapid growth of the void in the low pressure region at the entrance to the pump. The large amount of fluorine in the pump rapidly oxidizes the localized region which is modeled here by only accounting for the volatilization of chemical species as opposed to also incorporating structural corrosion from the wall. Therefore the combination of increasing the fluorine potential and the generation of a large interfacial area of the ideal gas phase bubble swarm due to the large amount of fluorine gas subsequently volatilizes a significant amount of iodine as seen in the bottom snapshots of Figure 36. In this example, the fluorine gas is rapidly absorbed into the fuel salt after the one second fluorination pulse has ended as seen in the 1.50 s snapshot. This corresponds to the decrease in total ideal-gas void in the pump, and subsequent decrease in iodine gas formation also seen in the 1.50 s snapshots.

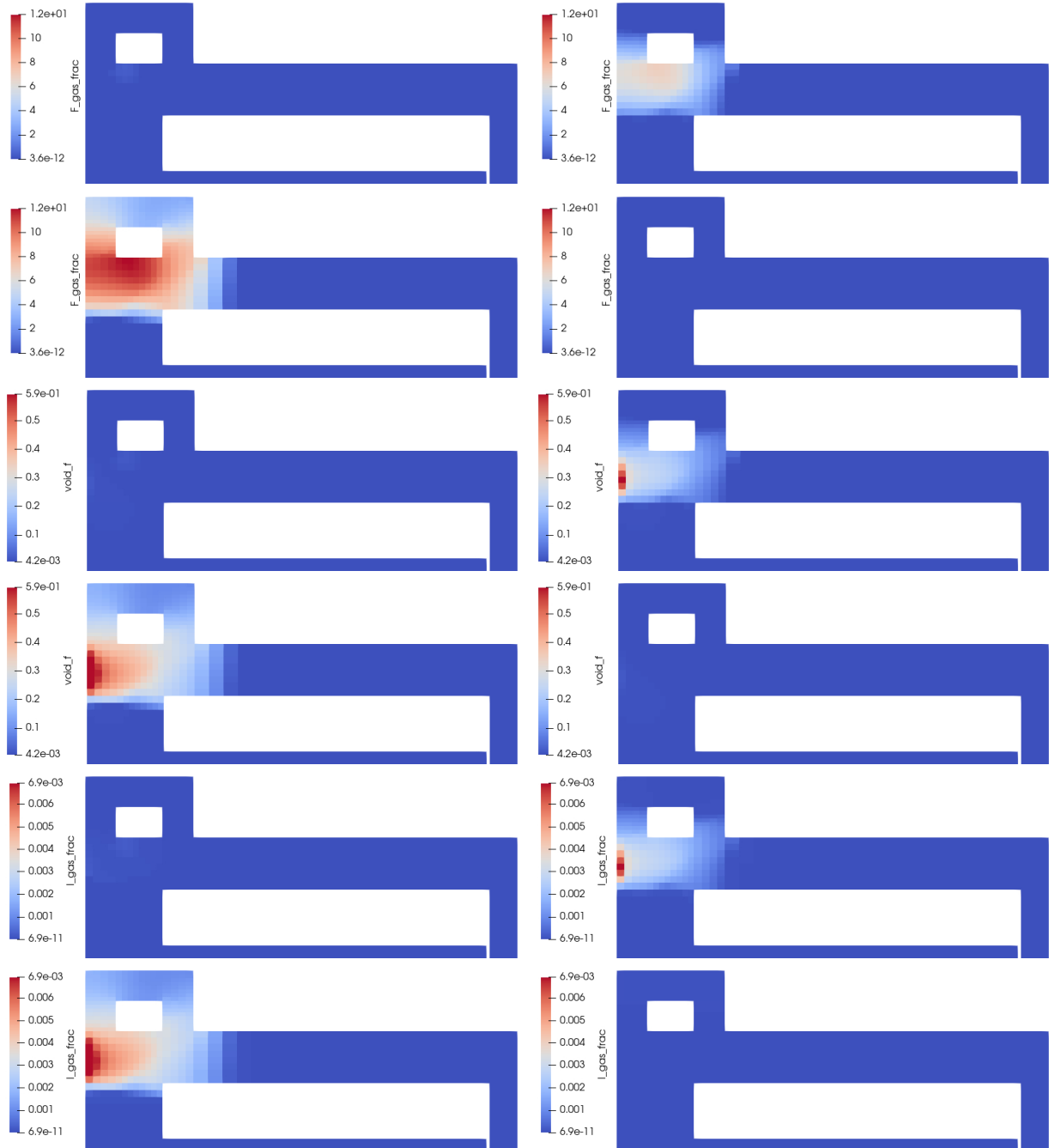


Figure 36. Fluorination pulse transient in MSRE: (a) Total fluorine gas [ $\text{mol m}^{-3}$ ] (from left to right) at 0.75 s, 1.00 s, 1.25 s, and 1.50 s respectively, (b) Total void [ $\text{mol m}^{-3}$ ] (from left to right) at 0.75 s, 1.00 s, 1.25 s, and 1.50 s respectively, (c) Total iodine gas [ $\text{mol m}^{-3}$ ] (from left to right) at 0.75 s, 1.00 s, 1.25 s, and 1.50 s respectively.

The corresponding whole system response of the fluorination pulse traveling through the MSRE is shown in Figure 37. Here the high fluoride potential in the pump due to the fluoroination pulse can be seen to migrate through the piping, downcomer, and upwards into the core oxidizing the entire system.

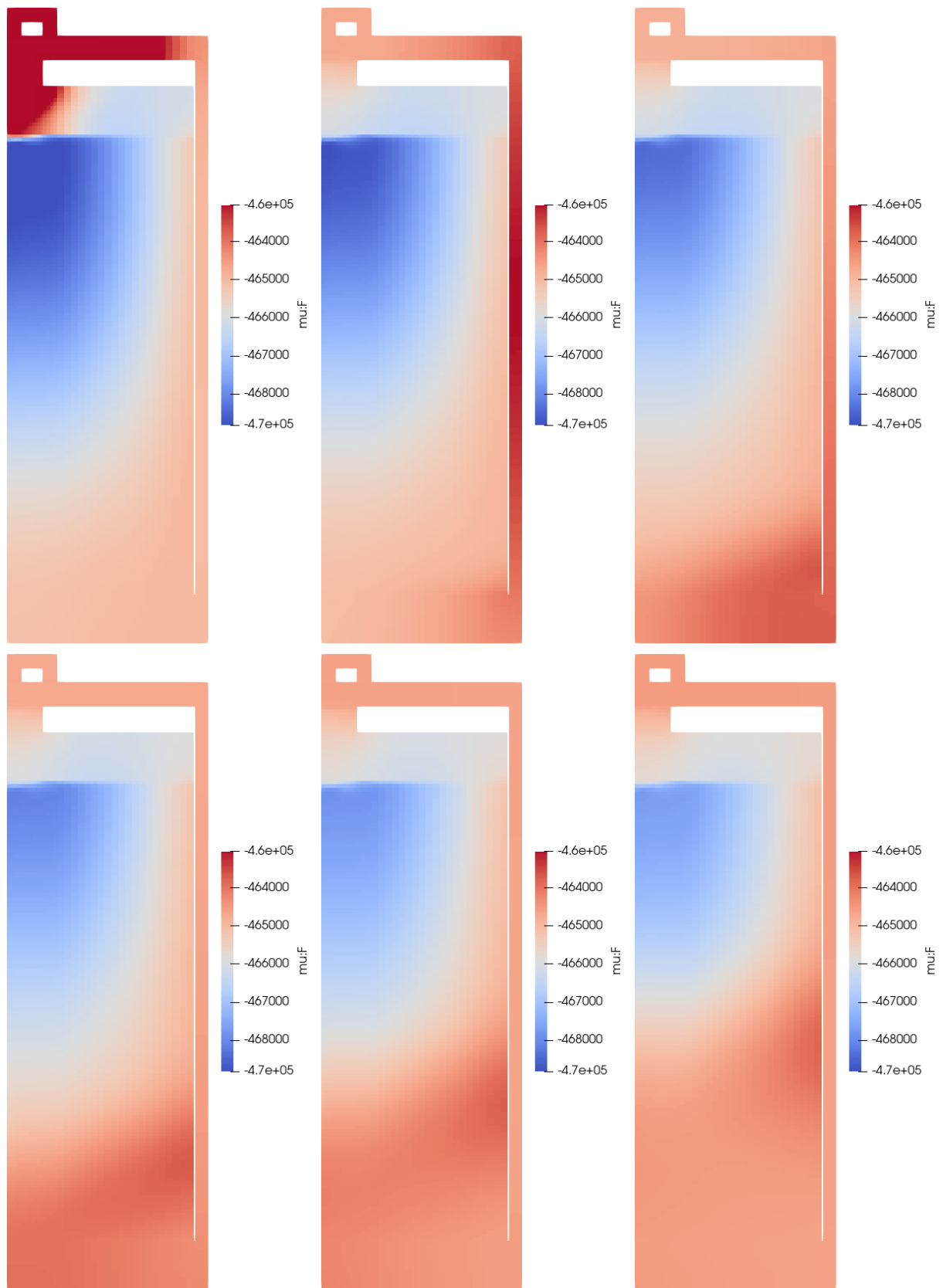


Figure 37. Changing fluoride potential [ $\text{J mol}^{-1}$ ] due to fluorination pulse transient in MSRE (from left to right): (a) at 1.00 s, (b) at 10.00 s, (c) at 20.00 s, (d) at 30.00 s, (e) at 40.00 s, (f) at 50.00 s.

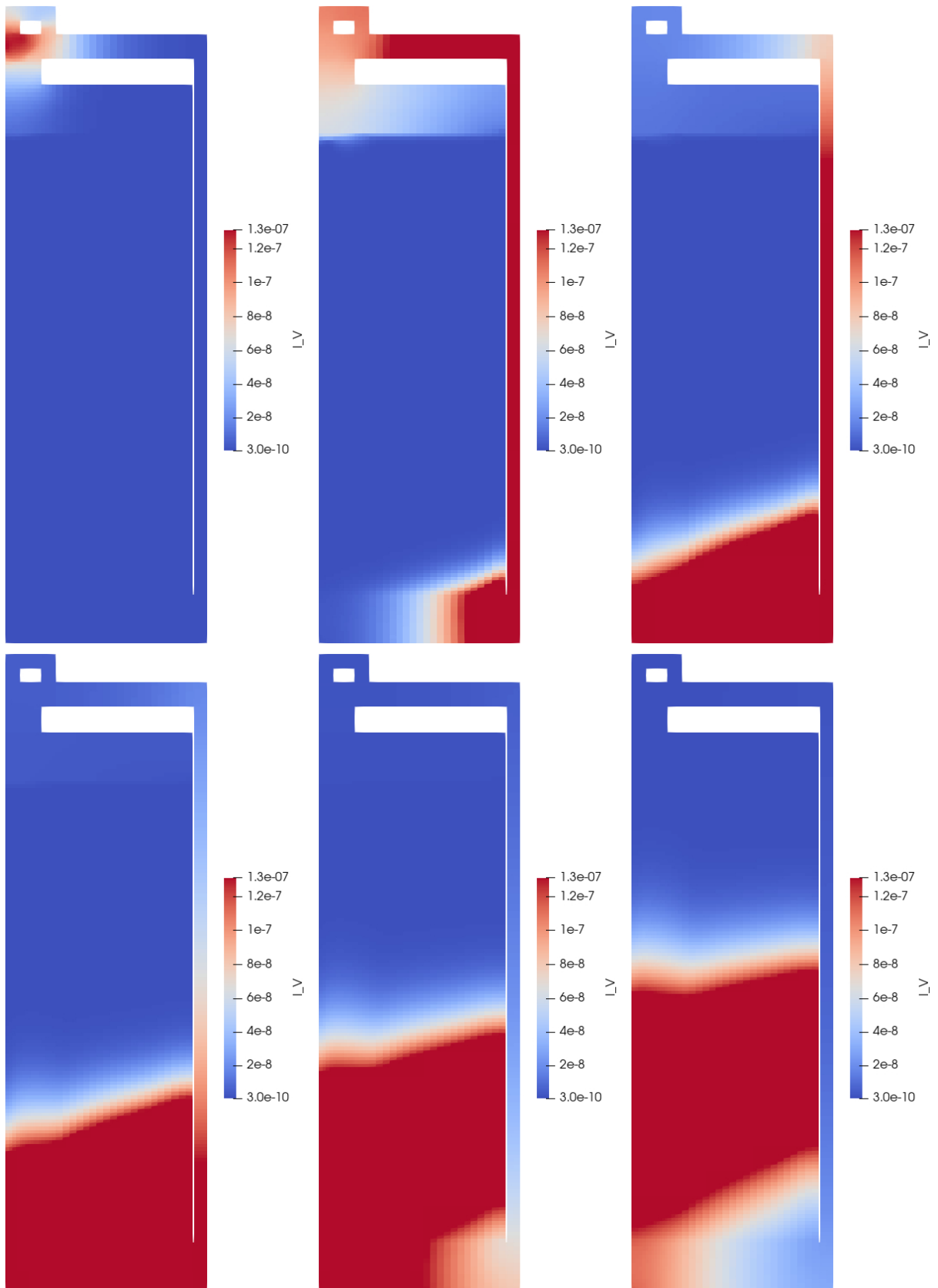


Figure 38. Circulating iodine gas [mol m<sup>-3</sup>] due to fluorination pulse transient in MSRE (from left to right): (a) at 1.00 s, (b) at 10.00 s, (c) at 20.00 s, (d) at 30.00 s, (e) at 40.00 s, (f) at 50.00 s.

Additionally, the iodine gas within the circulating helium void due to the significant volatilization of iodine during the 1 second fluorination pulse can also be seen in Figure 38. The volatilized iodine gas is formed in the pump and is transported throughout the reactor system until it reaches a new equilibrium by being extracted into the off-gas system through the pump bowl or by slowly re-dissolving back into the fluoride salt depending on the new fluoride potential of the system.

## 8. CONCLUSIONS

This work represents a significant advancement in developing a comprehensive multiphysics framework for modeling species tracking, corrosion, and depletion in Molten Salt Reactors (MSRs). The integration of Pronghorn and Thermochemica within the MOOSE framework enables advanced simulations that combine fluid dynamics, thermochemistry, and species transport, offering more accurate predictions of reactor behavior under various operational conditions. Demonstrating this framework in full MSR loop cases, such as the Lotus Molten Salt Reactor (L-MSR) and the Molten Salt Reactor Experiment (MSRE), demonstrates the potential of this model to predict critical phenomena in MSR systems through the coupling of NEAMS codes.

A key outcome of this work is the ability to model dynamic species behavior under both steady-state and transient conditions. The integration of Thermochemica allows for time- and space-resolved calculations of chemical potentials, equilibrium states, and species transport across liquid and gas phases. This capability is needed for simulating thermochemical processes, such as the volatilization of noble gases and fission products, which are required for designing off-gas systems and conducting reactor safety analyses. For instance, in L-MSR, simulations revealed that small quantities of fission products like cesium and iodine, though generally soluble in chloride salts, can volatilize under normal conditions. These findings emphasize the need of understanding how temperature, pressure, and chemical gradients influence fission product behavior, providing insights into mitigating the accumulation of volatile species and reducing the reactor's source term.

Another significant result is the modeling of depletion-driven thermochemistry and its effect on reactor performance and safety. In L-MSR, changes in uranium content due to fission were shown to alter the redox potential of the fuel salt, which, in turn, affected both species equilibrium and corrosion processes. The increased volatilization of iodine, cesium, and rubidium in the gas phase during extended reactor operation show that depletion models are required to be integrated into species tracking frameworks. This allows for accurate predictions of reactor behavior over long operational periods, giving the models the required capabilities for understanding the long-term implications of chemical changes in MSR systems.

In the MSRE case study, the ability to simulate two-phase flow, including the transport of volatile species through gas-liquid interactions, provided demonstrates the ability of the framework to handle species extraction from molten salt. Coupling Pronghorn's two-phase flow models with Thermochemica allowed for accurate predictions of helium void generation and the fractional volatilization of fission products into the off-gas system. These findings are especially relevant for reactors equipped with gas extraction systems, as even under steady-state conditions, trace amounts of volatile species such as iodine and rubidium were transported into the gas phase. The transient analysis of a fluorination pulse in MSRE further demonstrated the framework's capacity to handle rapid changes in chemical potential, providing a demonstration case of how MSRs might respond to chemical perturbations or redox control measures.

The use of the Molten Salt Thermal Properties Database-Thermochemical (MSTDB-TC) as the thermochemical foundation further ensures that predictions of species behavior, including volatilization, solubility, and phase stability, are grounded in accurate data. The MSTDB-TC data allowed for precise modeling of both fluoride and chloride salt systems, enabling reliable assessments of how operational parameters influence species transport and corrosion.

The development of corrosion models within this framework marks a significant step forward in predicting material degradation in MSRs. The coupling of the Poisson-Nernst-Planck (PNP) model with Butler-Volmer kinetics enabled the simulation of electrochemical processes driving corrosion at the fuel-salt and structural material interface. These models captured the influence of electric fields and concentration gradients on species transport, allowing for a mechanistic representation of the leaching and deposition behavior of structural materials, such as chromium, iron, and nickel. The PNP model's ability to predict localized corrosion in high-temperature molten salt environments, such as chromium leaching from hot regions and iron deposition in cooler regions, demonstrated the importance of temperature-driven electrochemical gradients in determining corrosion patterns.

The integration of corrosion models into the broader MOOSE-based framework represents a major advancement in MSR predictive capabilities. By combining thermochemistry, electrochemical kinetics, and species transport, these models provide detailed predictions of corrosion rates and material degradation over time. They offer critical insights into material longevity, redox control requirements, and strategies for mitigating corrosion risks. Future work will involve validating these models against experimental data and incorporating more complex geometries to further refine corrosion assessments.

In summary, this work underscores the importance of integrated thermochemical, fluid dynamic, and species transport modeling for understanding the behavior of MSRs. The ability to accurately predict species concentrations, chemical potentials, and gas-liquid interactions provides reactor designers with powerful tools for optimizing performance and safety. The findings validate the robustness of the Pronghorn-Thermochimica coupling and demonstrate its applicability to a range of MSR designs, from chloride-based systems like L-MSR to historical fluoride-based reactors like MSRE. This framework lays the groundwork for future advancements in MSR modeling, including optimizing off-gas systems, improving material longevity through corrosion predictions, and enhancing safety through accurate species tracking over long reactor lifetimes.

## 9. FUTURE WORK

While this work has demonstrated significant advancements in the multiphysics modeling of Molten Salt Reactors (MSRs), several areas of future research will be required to further enhance the predictive capabilities and operational insights provided by this framework. One important area for future work is the validation of the integrated models against experimental data from both historical and ongoing MSR experiments. While this study has shown promising results using benchmark cases such as the Molten Salt Reactor Experiment (MSRE), further validation with experimental datasets will be necessary to ensure that the coupled Thermochimica-Pronghorn framework accurately captures species transport, thermochemistry, and corrosion in real-world operational scenarios. This validation will also help improve model accuracy, enabling refinements that account for any discrepancies between simulation results and observed reactor behavior.

The incorporation of more detailed and complex geometries is another key direction for future work. Currently, the full MSR loop simulations focus on simplified geometries to streamline computational effort. Expanding the framework to model more detailed reactor components, such as intricate heat exchangers, structural supports, and fuel assemblies, will provide more granular insights into species transport and material degradation patterns within MSR designs. This is particularly important for understanding localized corrosion effects and predicting long-term reactor performance under varying operational conditions. As MSR designs continue to evolve, the ability to simulate these more complex geometries will become crucial for optimizing reactor components and ensuring operational reliability. The increased simulation complexity also necessitates the development of acceleration techniques to speed up the Gibbs energy minimization. Future work will

involve the development and application of caching, surrogate models, and machine learning techniques.

Another area of future work is the continued development of depletion models and their integration with species tracking and corrosion processes. While this work has demonstrated the capability to model depletion-driven thermochemistry, further refinement of depletion models will be needed to handle higher burnup scenarios and to capture the interactions between fuel composition changes, redox potential shifts, and species transport. Future research should focus on coupling depletion models with transient scenarios to assess how fuel depletion influences reactor safety, fission product behavior, and corrosion dynamics over long-term operation. In particular, the interaction between fuel depletion, fission product volatilization, and off-gas system design could be explored in more depth to ensure that MSR systems can manage long-term operational risks effectively.

The integration of two-phase flow modeling for tracking volatile species in both the liquid and gas phases presents another promising area for future development. While the current framework models gas-liquid interactions, further research could focus on refining the accuracy of these models, particularly in relation to bubble dynamics, interfacial mass transfer, and the transport of volatile species under varying pressure and temperature conditions. This would be especially beneficial for evaluating the impact of off-gas systems and for ensuring the effective removal of volatile fission products. Improvements in two-phase flow modeling would also enhance the ability to predict corrosion in regions where gas bubbles form, as well as the transport of species through the reactor's gas phase, which is critical for maintaining reactor safety and operational efficiency.

Future work will also need to focus on improving the robustness of the corrosion models. While the current coupling of the Poisson-Nernst-Planck (PNP) model and Butler-Volmer kinetics allows for mechanistic predictions of corrosion behavior, further development could include more advanced electrochemical models to account for complex redox chemistry and multi-material interfaces. Additionally, the framework would benefit from enhanced modeling of time-dependent corrosion processes, such as material fatigue, cracking, and long-term degradation due to prolonged exposure to molten salts. Validating these corrosion models with experimental corrosion data from high-temperature MSR environments will be a crucial step toward ensuring the accuracy and reliability of these predictions in practical applications.

An important avenue for enhancing corrosion modeling in Molten Salt Reactors involves incorporating phase-field modeling to capture the interactions at the salt-solid interface. Phase-field models are particularly well-suited for simulating microstructural evolution, enabling the detailed representation of localized corrosion processes, such as the nucleation and growth of corrosion pits, material dissolution, and the formation of oxidized layers. By integrating phase-field methods into the existing PNP framework, future work can provide a more mechanistic description of corrosion at the salt-structure interface, accounting for the influence of microstructural heterogeneities, temperature gradients, and chemical potential variations and hence, improve the approximations in the Butler Volmer model. This approach will allow for a deeper and more mechanistic understanding of the spatial and temporal evolution of corrosion, offering insights into material degradation patterns and informing the development of advanced materials and coatings designed to withstand harsh molten salt environments. Phase-field modeling could also be applied to investigate the effect of redox control measures on corrosion progression, making it a key tool for predicting long-term material behavior in MSRs.

## 10. REFERENCES

- [1] J. R. Engel, P. N. Haubenreich, and A. Houtzeel, "Spray, mist, bubbles, and foam in the molten salt reactor experiment," Tech. Rep. ORNL-TM-3027, Oak Ridge National Laboratory, 1 1970.

- [2] W. Grimes, “Molten-salt reactor chemistry,” *Nuclear Applications and Technology*, vol. 8, no. 2, pp. 137–155, 1970.
- [3] K. Sridharan and T. Allen, “Corrosion in molten salts,” in *Molten salts chemistry*, pp. 241–267, Elsevier, 2013.
- [4] G. Zheng and K. Sridharan, “Corrosion of structural alloys in high-temperature molten fluoride salts for applications in molten salt reactors,” *JOM*, vol. 70, pp. 1535–1541, 2018.
- [5] J. W. McMurray, T. M. Besmann, J. Ard, B. Fitzpatrick, M. Piro, J. Jerden, M. Williamson, B. S. Collins, B. R. Betzler, and A. Qualls, “Multi-physics simulations for molten salt reactor evaluation: Chemistry modeling and database development,” tech. rep., Oak Ridge National Lab.(ORNL), Oak Ridge, TN (United States), 2018.
- [6] S. Shahbazi, M. E. Tano, S. Walker, M. R. Tonks, and J. Fang, “Survey of relevant data from the MSRP to guide development of MSR chemistry modeling benchmarks,” tech. rep., Argonne National Laboratory (ANL), Argonne, IL (United States), 2022.
- [7] J. F. Cooper, W. Brummond, J. Celeste, J. Farmer, C. Hoenig, O. H. Krikorian, R. Upadhye, R. L. Gay, A. Stewart, and S. Yosim, “Molten salt processing of mixed wastes with offgas condensation,” tech. rep., Lawrence Livermore National Lab., CA (USA), 1991.
- [8] A. Lindsay, G. Giudicelli, P. German, J. Peterson, Y. Wang, R. Freile, D. Andrs, P. Balestra, M. Tano, R. Hu, *et al.*, “MOOSE Navier–Stokes module,” *SoftwareX*, vol. 23, p. 101503, 2023.
- [9] M. Poschmann, P. Bajpai, B. W. Fitzpatrick, and M. H. Piro, “Recent developments for molten salt systems in Thermochimica,” *Calphad*, vol. 75, p. 102341, 2021.
- [10] J. Robinson and D. Fry, “Experimental neutron flux-to-pressure frequency response for the molten-salt reactor experiment: determination of void fraction in fuel salt,” *Nuclear Science and Engineering*, vol. 42, no. 3, pp. 397–405, 1970.
- [11] W. Liu and H. Xu, “A complete analysis of a classical Poisson–Nernst–Planck model for ionic flow,” *Journal of Differential Equations*, vol. 258, no. 4, pp. 1192–1228, 2015.
- [12] A. Pelton, S. Degterov, G. Eriksson, C. Robelin, and Y. Dessureault, “The Modified Quasichemical Model I – Binary Solutions,” *Metallurgical and Materials Transactions B*, vol. 31B, pp. 651–659, 2000.
- [13] A. Pelton and P. Chartrand, “The Modified Quasichemical Model II – Multicomponent Solutions,” *Metallurgical and Materials Transactions A*, vol. 32A, pp. 1355–1360, 2001.
- [14] P. Chartrand and A. Pelton, “The Modified Quasichemical Model III – Two Sublattices,” *Metallurgical and Materials Transactions A*, vol. 32, pp. 1397–1407, 2001.
- [15] A. Pelton, P. Chartrand, and G. Eriksson, “The Modified Quasichemical Model IV – Two-Sublattice Quadruplet Approximation,” *Metallurgical and Materials Transactions A*, vol. 32, pp. 1409–1416, 2001.
- [16] G. Lambotte and P. Chartrand, “Thermodynamic optimization of the ( $\text{Na}_2\text{O} + \text{SiO}_2 + \text{NaF} + \text{SiF}_4$ ) reciprocal system using the Modified Quasichemical Model in the Quadruplet Approximation,” *Journal of Chemical Thermodynamics*, vol. 43, pp. 1678–1699, 2011.
- [17] M. Hillert, “The Compound Energy Formalism,” *Journal of Alloys and Compounds*, vol. 320, no. 2, pp. 161 – 176, 2001.

- [18] M. H. A. Piro, T. M. Besmann, S. Simunovic, B. J. Lewis, and W. T. Thompson, “Numerical verification of equilibrium thermodynamic computations in nuclear fuel performance codes,” *Journal of Nuclear Materials*, vol. 414, no. 3, pp. 399 – 407, 2011.
- [19] M. Piro and S. Simunovic, “Global optimization algorithms to compute thermodynamic equilibria in large complex systems with performance considerations,” *Computational Materials Science*, vol. 118, pp. 87–96, 2016.
- [20] C. G. Zoski, *Handbook of electrochemistry*. Elsevier, 2006.
- [21] E. J. Dickinson and A. J. Wain, “The Butler–Volmer equation in electrochemical theory: Origins, value, and practical application,” *Journal of Electroanalytical Chemistry*, vol. 872, p. 114145, 2020.
- [22] E. McCafferty, “Validation of corrosion rates measured by the Tafel extrapolation method,” *Corrosion science*, vol. 47, no. 12, pp. 3202–3215, 2005.
- [23] F. Mansfeld, “Tafel slopes and corrosion rates from polarization resistance measurements,” *Corrosion*, vol. 29, no. 10, pp. 397–402, 1973.
- [24] E. Gileadi and E. Kirowa-Eisner, “Some observations concerning the tafel equation and its relevance to charge transfer in corrosion,” *Corrosion science*, vol. 47, no. 12, pp. 3068–3085, 2005.
- [25] A. J. Bard, L. R. Faulkner, and H. S. White, *Electrochemical methods: fundamentals and applications*. John Wiley & Sons, 2022.
- [26] P. J. Roache, “Perspective: A Method for Uniform Reporting of Grid Refinement Studies,” *Journal of Fluids Engineering*, vol. 116, pp. 405–413, 09 1994.
- [27] M. Ishii and T. Hibiki, *Thermo-fluid dynamics of two-phase flow*. Springer Science & Business Media, 2010.
- [28] C. Wu, X. Li, J. Wu, C. Yu, C. Zou, X. Cai, and J. Chen, “Xenon behavior modeling for molten salt reactors by using multiple transport mechanisms,” *Progress in Nuclear Energy*, vol. 168, p. 104987, 2024.
- [29] R. J. Kedl, “Migration of a class of fission products (noble metals) in the molten-salt reactor experiment,” Tech. Rep. ORNL-TM-3884, Oak Ridge National Laboratory, 12 1972.
- [30] F. N. Peebles, “Removal of  $^{135}\text{xe}$  from circulating fuel salt of the msbr by mass transfer to helium bubbles.,” Tech. Rep. ORNL-TM-2245, Oak Ridge National Laboratory, 1 1968.
- [31] M. Pusa and J. Leppänen, “Solving Linear Systems with Sparse Gaussian Elimination in the Chebyshev Rational Approximation Method,” *Nuclear Science and Engineering*, vol. 175, no. 3, pp. 250–258, 2013.
- [32] S. S. Raiman, J. M. Kurley, D. Sulejmanovic, A. Willoughby, S. Nelson, K. Mao, C. M. Parish, M. S. Greenwood, and B. A. Pint, “Corrosion of 316H stainless steel in flowing FLiNaK salt,” *Journal of Nuclear Materials*, vol. 561, p. 153551, 2022.
- [33] J. C. Ard, J. A. Yingling, T. J. Johnson, J. Schorne-Pinto, M. Aziziha, C. M. Dixon, M. S. Christian, J. W. McMurray, and T. M. Besmann, “Development of the Molten Salt Thermal Properties Database – Thermochemical (MSTDB–TC), example applications, and LiCl–RbCl and UF<sub>3</sub>–UF<sub>4</sub> system assessments,” *Journal of Nuclear Materials*, vol. 563, p. 153631, 2022.

- [34] D. Walter, T. Cisneros, K. Wardle, J. Walter, and S. Findlay, “MCRE design description in support of external model development,” tech. rep., TerraPower, (United States), 2023.
- [35] S. A. Walker, M. E. Tano, A. Abou-Jaoude, and O. Calvin, “Depletion-driven thermochemistry of molten salt reactors: review, method, and analysis,” *Frontiers in Nuclear Engineering*, vol. 2, 2023.
- [36] P. N. Haubenreich and J. R. Engel, “Experience with the molten-salt reactor experiment,” *Nuclear Applications and Technology*, vol. 8, no. 2, pp. 118–136, 1970.